Development of software-based methods to evaluate the eye safety of laser based optical systems

Dissertation

der Mathematisch-Naturwissenschaftlichen Fakultät
der Eberhard Karls Universität Tübingen
zur Erlangung des Grades eines
Doktors der Naturwissenschaften
(Dr. rer. nat.)

vorgelegt von
Sebastian Kotzur
aus Ludwigsburg

Tübingen
2024

Gedruckt mit Genehmigung der Mathematisch-Naturwissenschaftlichen Fakultät der Eberhard Karls Universität Tübingen.

Tag der mündlichen Qualifikation:	05.07.2024
Dekan:	Prof. Dr. Thilo Stehle
1. Berichterstatter/-in:	Prof. Dr. Frank Schaeffel
2. Berichterstatter/-in:	Prof. Dr. Siegfried Wahl

‘Finally Prof. Wolbarsht, the chair of the Ocular Bioeffects Subcommittee just sent out a set of limits without giving a rationale and all agreed to the limits.’

Dr. David H. Sliney

‘What is the minimal retina image size? – Implications for setting MPE’s’, ILSC 2005, 43-47. doi:10.2351/1.5056609 (2005)

Contents

1 Zusammenfassung

In dieser Dissertation wurden softwarebasierten Methodiken zur Berechnung der Augensicherheit entwickelt mit dem Fokus auf Laserstrahlung, die auf der Netzhaut des Auges abgebildet wird. Die entwickelten Tools umfassen zum einem die korrekte digitale Implementierung der Lasersicherheitsnorm [IEC, 2014], welche Grenzwerte enthalten, und zum anderen die Entwicklung eines Computermodells zur Simulation thermischer Netzhautschädigungen, welche zur Weiterentwicklung und Validierung der Normen genutzt werden kann. Insgesamt wurden drei Studien durchgeführt. Die erste Studie befasst sich mit der Entwicklung eines Analyseverfahrens für Netzhautbilder, welches eindeutig und hinreichend restriktiv ist und die Anforderungen aus der Lasersicherheitsnorm [IEC, 2014] und der Lampensicherheitsnorm [IEC, 2006] erfüllt. Die Netzhautgrenzwerte repräsentieren photochemische, thermische und thermomechanische Gefährdungen. Mit der Bewertung der Augensicherheit gehen umfangreiche Rechnungen einher, bei denen die Größe der Netzhautbilder durch die Winkelausdehnung der scheinbaren Quelle α beschrieben wird, welcher den Winkel repräsentiert, den das Netzhautbild im Auge aufspannt. Während die Norm hierfür lediglich eine implizite Erklärung vorstellt, wird in dieser Studie ein Verfahren mit einer eindeutigen Definition entwickelt. Es wurde ermittelt, dass die Winkelausdehnung nicht aus Strahlparametern der Laserquelle, sondern durch Analyse der Netzhautbilder abgeleitet wird und zu einem Netzhautbild mehrere Ergebnisse vorliegen können. In der zweiten Studie wurde ein Gaußstrahl mit unterschiedlichen Wellenlängen und Strahltaillen in verschiedenen Abständen vor einem Auge platziert. Unter der Verwendung des Luft äquivalenten Augenmodells, wurden mittels Wellenpropagation die Netzhautbilder für verschiedene Akkommodationszustände berechnet und ausgewertet. Gaußstrahlen stellen häufig einen ersten Ausgangspunkt bei Augensicherheitsrechnungen von Laserstrahlung dar. Es wurde gezeigt, dass die bisher verwendeten analytischen Beschreibungen Beugungseffekte vernachlässigen, welche das Gefährdungspotential erhöhen. Daher wurde eine erweiterte analytische Formel eingeführt und validiert, die diese Effekte berücksichtigt und zu sicheren Ergebnissen führt. In der letzten Studie wurde das Computermodell zur Simulation thermischer Netzhautschädigung entwickelt. Dieses beinhaltet ein Augenmodell zur Berechnung des Netzhautbildes und ein 3D-Modell der Netzhaut zur Bestimmung des Wärmetransportes. Es wurden elliptische Gaußverteilungen, sowie rechteckige und elliptische Top-Hat-Verteilungen für verschiedene Einzelpulsdauern und Profilgrößen untersucht. Für die Normrechnung wird ein Verfahren verwendet, bei dem die gemittelte Profilgröße eingeht. Dieses Vorgehen beruht auf keiner experimentellen Grundlage und daher wurde dieser Datensatz simulativ erzeugt. Für die in dieser Studie untersuchten Profile konnte das Verfahren der Norm validiert werden.

2 Summary

In this thesis software-based methods to evaluate the eye safety were developed with a focus on laser radiation that is imaged on the retina. The developed tools include on one hand the correct digital implementation of the laser safety standard [IEC, 2014] which provide limits and on the other hand the development of a computer model for simulating retinal thermal injuries which can be used for the further development and validation of the standards. In total, three studies were performed. The first study focuses on the development of an analysis method for retinal images that is unambiguous and sufficiently restrictive and fulfills the requirements of the laser safety standard [IEC, 2014] and the lamp safety standard [IEC, 2006]. The retinal limits represent photochemical, thermal, and thermomechanical hazards. The eye safety evaluation involves extensive calculations in which the size of the retinal images is described by the angular subtense of the apparent source α, which represents the angle that the retinal image spans in the eye. While the laser safety standard only provides an implicit explanation for this value, in this study a procedure is developed where this value is unambiguously defined. It was determined that this quantity cannot be derived from beam parameters of the laser source, but by analysing the retinal images and that multiple results for the α-value can be obtained. In the second study, a Gaussian beam for different wavelengths and beam waists is located in front of an eye at different distances. By using the air equivalent eye model and wave optical propagation, retinal images were generated for different accommodation states and evaluated according to the laser safety standard. Gaussian beams often represent a first starting point for eye safety evaluations of laser radiation. It was shown that the analytical descriptions used up to now neglect diffraction effects which increase the hazard potential. For this reason, an extended analytical formula was introduced and validated that takes these effects into account and leads to safe results. In the last study, the computer model for simulating thermal retinal damage was developed. This includes an eye model to calculate the retinal image and a 3D model of the retina to evaluate the heat transport. Elliptical Gaussian distributions, and rectangular and elliptical top-hat distributions were investigated for different single pulse durations and profile widths. For the evaluation according to the standard, a procedure is used in which the averaged profile size is included. This procedure has no experimental basis and therefore this data set was generated simulatively. The calculation procedure was validated for profiles examined in this study.

3 Publications and conference contributions related to this work

3.1 Peer reviewed publications

Jean, M., Schulmeister, K., **Kotzur, S.**, & Frederiksen, A. (2020). Validation of a generalized laser safety analysis method for irregular pulse trains. *Journal of Laser Applications*, 32(3):032027. doi: 10.2351/7.0000017

Lipp, S., **Kotzur, S.**, Elmlinger, P., & Stork, W. (2020). Multiple-pulse damage thresholds of retinal explants in the ns-time regime. *Biomed. Opt. Express*, 11(12):7299-7310. doi: 10.1364/BOE.412012

Kotzur, S., Wahl, S., & Frederiksen, A. (2021). Wave optical simulation of retinal images in laser safety evaluations. J. Biophotonics., 14(2), 14:e202000339. doi:10.1002/jbio.202000339

Kotzur, S., Wahl, S., & Frederiksen, A. (2021). Simulation of laser-induced retinal thermal injuries for non-uniform irradiance profiles and the applicability of the laser safety standard. Opt. Eng., 60(6), 0066115. doi:10.1117/1.OE.60.6.066115

Wichmann, M., Kamil, M., Frederiksen, A., **Kotzur, S.**, & Scherl, M. (2022). Long-Term Investigations of Weather Influence on Direct Time-of-Flight Lidar at 905 nm. *IEEE Sensors Journal*, 22(3):2024-2036. doi: 10.1109/JSEN.2021.3133658

Kotzur, S., Wahl, S., & Frederiksen, A. (2023). Image analysis of retinal images in eye safety evaluations for optical systems. Opt. Eng., 62(1), 016102. doi:10.1117/1.OE.62.1.016102

3.2 Non peer reviewed publications

Kotzur, S., & Frederiksen, A. (2018). Klassifizierung einfach astigmatischer Gaußstrahlen nach IEC 60825-1. *StrahlenschutzPRAXIS*, 3.

Kotzur, S., Wahl, S., & Frederiksen, A. (2020). Klassifizierung nach Lasersicherheitsnorm IEC 60825-1:2014 - Alles klar?. *StrahlenschutzPRAXIS*, 3.

3.3 Peer reviewed Conference contributions

Kotzur, S., Frederiksen, A., & Wahl, S. (2019). Consideration of wave optical phenomena for retinal images in laser safety evaluations. *International Laser Safety Conference*, 2019(1):903. doi: 10.2351/1.5118598

Jean, M., **Kotzur, S.**, Heussner, N., Schulmeister, K., & Frederiksen, A. (2019). Computer modelling to support laser safety analysis of pulse trains with varying peak power and pulse duration. *International Laser Safety Conference*, 2019(1):202. doi: 10.2351/1.5056872

Kotzur, S., Wahl, S., & Frederiksen, A. (2020). Retinal image analysis for eye safety evaluations of products emitting optical radiation. *Proc. SPIE*, Optical Interactions with Tissue and Cells XXXI, 1123808. doi: 10.1117/12.2545673

Kotzur, S., Wahl, S., & Frederiksen, A. (2020). Simulation of laser induced retinal thermal injuries for non-uniform irradiance profiles and their evaluation according to the laser safety standard. *Proc. SPIE*, Tissue Optics and Photonics, 1136314. doi: 10.1117/12.2555492

Kotzur, S., Wahl, S., & Frederiksen, A. (2023). Simulated retinal thermal damage for repetitively pulsed lasers with rectangular shaped irradiance profiles. *International Laser Safety Conference*, 2023(1):101.

3.4 Non Peer reviewed Conference contributions

Halbritter, W., **Kotzur, S.**, Janssen, H., & Frederiksen, A. (2018). The Sun - Basis of our lives but not completely harmless?. *NIR2018: Wellen - Strahlung - Felder*, ISSN 1013-4506, 209-226

Frederiksen, A., Janssen, H., **Kotzur, S.**, & Halbritter, W. (2018). Incoherent optical radiation: Overlapping exposure limits - Why?. *NIR2018: Wellen - Strahlung - Felder*, ISSN 1013-4506, 55-67

4 Statement of own contribution

I declare that this thesis has been composed solely by myself and that it has not been submitted, in whole or in part, in any previous application for a degree. I have not used any sources other than those I have indicated. In the appendix of this thesis, three peer-reviewed papers are included, which were published within the scope of this cumulative dissertation. The contributions of the authors mentioned in these papers are explained in the following subsections.

4.1 Publication 1 - Wave optical simulation of retinal images in laser safety evaluations

Kotzur, S., Wahl, S., & Frederiksen, A. (2021). Wave optical simulation of retinal images in laser safety evaluations. J. Biophotonics., 14(2), 14:e202000339. doi:10.1002/jbio.202000339

Contribution of the first author:

I have developed the initial idea for the study and developed and defined the methodology. I performed the simulation of the study and analyzed the data. I have written the initial version of the manuscript and further improved it based on my ideas and the input from the other authors.

Contribution of the other authors:

The second author of the paper, Prof. Dr. Siegfried Wahl was available for support, gave suggestions and helped to improve the manuscript. The last author, Dr. Annette Frederiksen, supported the study with her experience and expertise and helped to improve the manuscript with her suggestions and advice.

4.2 Publication 2 - Simulation of laser-induced retinal thermal injuries for non-uniform irradiance profiles and the applicability of the laser safety standard

Kotzur, S., Wahl, S., & Frederiksen, A. (2021). Simulation of laser-induced retinal thermal injuries for non-uniform irradiance profiles and the applicability of the laser safety standard. Opt. Eng., 60(6), 0066115. doi:10.1117/1.OE.60.6.066115

Contribution of the first author:

I have developed the initial idea for the study and developed and defined the methodology. I performed the simulation of the study and analyzed the data. I have written the initial version of the manuscript and further improved it based on my ideas and the input from the other authors.

Contribution of the other authors:

The second author of the paper, Prof. Dr. Siegfried Wahl was available for support, gave suggestions and helped to improve the manuscript. The last author, Dr. Annette Frederiksen, supported the study with her experience and expertise and helped to improve the manuscript with her suggestions and advice.

4.3 Publication 3 - Image Analysis of retinal images in eye safety evaluations for optical systems

Kotzur, S., Wahl, S., & Frederiksen, A. (2023). Image analysis of retinal images in eye safety evaluations for optical systems. Opt. Eng., 62(1), 016102.
doi:10.1117/1.OE.62.1.016102

Contribution of the first author:

I have developed the initial idea for the study and developed and defined the methodology. I performed the simulation of the study and analyzed the data. I have written the initial version of the manuscript and further improved it based on my ideas and the input from the other authors.

Contribution of the other authors:

The second author of the paper, Prof. Dr. Siegfried Wahl was available for support, gave suggestions and helped to improve the manuscript. The last author, Dr. Annette Frederiksen, supported the study with her experience and expertise and helped to improve the manuscript with her suggestions and advice.

5 Introduction

5.1 Motivation

The invention of the laser (short for Light Amplification by Stimulated Emission of Radiation) in 1960 [Maiman, 1960] marks an important turning point in the history of technology and innovation. The laser has become an integral part of countless fields, such as industry, manufacturing, medicine, information technology, science and research. Even in the everyday life of each individual, the laser finds its use, such as in laser pointers, optical disc drives or in laser printers. In addition, the laser is also used for entertainment purposes such as in laser shows. A laser beam can be described by an electromagnetic wave with the special characteristics that it is monochromatic, coherent, can have small divergences and can be highly focused resulting in high irradiance levels. Many properties of laser radiation, such as a specific pulse pattern, power, wavelength, phase or polarization, can be precisely adjusted resulting in a range of applications. Research on the laser is still ongoing and further innovations will enable a wider range of applications in the future.

However, with lasers also comes a potential hazard, as the radiation can interact with biological tissue and causes damage. The eye is the most sensitive part of the body in terms of laser damage. For a certain wavelength range, the radiation propagates through the eye and can be highly focused on the retina. Damages to the retina are irreversible and are accompanied by a loss of vision in the damaged regions. The potential hazards of lasers were recognized early on, and so five years after the invention of the laser, there was the first guide in the field of laser safety. [Ministry of Aviation, 1965] As lasers have been further developed, there has also been a lot of research in laser safety, and today the International Commission of Non-Ionizing Radiation Protection (ICNIRP) provides guidelines that include a collection of exposure limits for laser radiation for wavelengths between 180 nm and 1 mm. [ICNIRP, 2013b] The International Electrotechnical Commission (IEC) provides relevant international product safety standards that contain a classification system from laser Class 1 to Class 4. The most important standard for laser products is the IEC 60825-1:2014. [IEC, 2014] However, the application of this standard is not always a trivial matter, because as diverse as laser radiation can interact with the biological tissue, the set of analysis rules in the standard is also correspondingly extensive. To a large extent, the limit values and analysis methods contained in the laser safety standard attempt to resemble the high complexity of biophysics in the field of laser-tissue interaction. For this reason, there is not always a clear answer to various questions. The following quote shows that at some points one is forced to make assumptions with the aim to provide limits that

are sufficiently safe 'Finally Prof. Wolbarsht, the chair of the Ocular Bioeffects Subcommittee just sent out a set of limits without giving a rationale and all agreed to the limits.' [Sliney, 2005] These two aspects, the non-trivial application of the standard and the answering of research relevant questions regarding safe limits, will be addressed in this thesis. The first aspect is a major challenge, since the laser standard only provides an explicit evaluation scheme for simple laser systems such as static, collimated and regular pulsed beams. For more complex systems, e.g. scanning laser systems emitting multiple wavelengths, one must rely on implicit descriptions that have room for interpretation. This problem is aggravated when considering radiation that is imaged on the retina. An unambiguous description to ensure sufficiently restrictive evaluations is strongly needed. Another important point is the eye safety evaluation of Gaussian beams which are often used for simple descriptions of laser systems. Since Gaussian beams can be described analytically, the laser safety standard refers to their specific characteristics that are included in the evaluation. However, this approach has a limited application, since wave optical phenomena lead to behavior that deviates from the analytical descriptions of Gaussian beams and have a significant impact on eye safety calculations. This means that, according to the current state of the standard, there is a potential risk to significantly underestimate the eye hazard. In the second aspect, open questions are addressed, which among others form the basis in the laser standard. Especially for retinal images, which do not show circular symmetry, there is an evaluation scheme in the standard, but no experimental data on which it is based. For this reason, a computer model is further developed in this thesis, with which thermal damages on the retina can be simulated and thus the evaluation scheme can be validated.

The studies in this thesis are motivated with the aim to close current gaps in the laser safety standard using a software-based approach. The methodologies developed here contribute to the further development of standards and guidelines and can support in the development of a laser product, whereby potential hazards to the eye are already identified in early stages of the development process.

5.2 The human eye

The eye is a sensory organ that enables vision and has the main function to image light on the retina. It not only has the ability to focus on objects at different distances from about 10 cm to infinity, but is also able to adapt to different ambient brightnesses and different source intensities. It is estimated that the human eye can see several million colors [Judd et al., 1963] and it is even hinted that it is able to detect a single photon [Tinsley et al., 2016]. The human eye is almost spherical in shape with a diameter of about 24 mm. [Gross et al., 2008b] Figure 1 shows an illustration of the human eye with the essential eye parts.

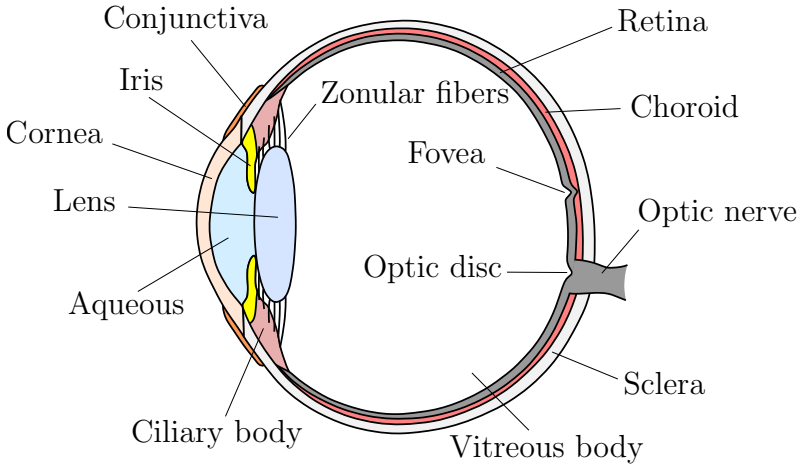

Figure 1: Illustration of a cross section of a human eye. The different parts of the eye are highlighted and labeled.

The main parts of the eye that are responsible for the image formation are the cornea and the lens whereas the cornea makes about two thirds of the total refractive power of the eye. [Gross et al., 2008b] The refractive power of the cornea is about 43 diopters. [Smith and Atchison, 1997] In consequence of the absence of blood vessels, oxygen and nutrients are transported to the cornea via tear fluid and the aqueous humour located in the anterior chamber. [Ng et al., 2012] The cornea is a transparent medium with a refractive index of about 1.376 and is embedded in the sclera. Its diameter is about 12 mm and at the center the thickness is around 0.55 mm. At the edges, the thickness of the cornea slightly increases. The aspherical shape at the edges reduces spherical aberrations in case of large pupil diameters. Between the edge of the cornea and the inside of the eyelid is the conjunctiva. This consists of connective tissue and multilayer epithelium. The conjunctiva enables smooth eye movement with no friction and produces part of the tear fluid, which is distributed by the blinking of the eyelid. [Lang, 2019] The largest part of the outer layer of the eye is the sclera. It has a whitish color and helps to maintain the spherical shape of the eye. It covers the eye at about 80 % and has a water content between 65 % and 75 %. [Dische, 1970] The sclera is connected to the cornea and at the front of the eye it is covered by the conjunctiva. On the opposite side of the eye, the sclera has an exit point for the optic nerve. Six small muscles are attached to the sclera and enable eye movements. [Hahn, 2012] When light enters the eye through the cornea, it passes through the anterior chamber of the eye, which is filled with a fluid called aqueous humour, before it hits the lens. The anterior chamber is the area between the lens and the iris. The aqueous has a refractive index of 1.336 [Kaschke et al., 2014] which is very similar to the refractive index of the cornea. For this reason, the incoming rays are only very weakly refracted at the boundary of both tissues. [Pedrotti et al., 2017] The aqueous is produced in the posterior chamber

which is located between the iris and the ciliary body. The main functions of the aqueous is to bring oxygen and nutrients to the lens and cornea and to dispose waste products. In addition, it helps to maintain the shape of the eye through its internal pressure. [Ng et al., 2012] The amount of light that is entering the eye is regulated by the iris, a pigmented aperture in front of the lens. This aperture is referred to as eye pupil. The iris is composed of 2 layers where the first anterior layer, the stroma, contains blood vessels and nerve tracts. It is connected to a sphincter muscle, which serves to reduce the pupil size. The pupil can be enlarged again by a dilator muscle. The second posterior layer is a pigmented epithelial layer, which is two cells thick and filters stray light. [Kaufman et al., 2003; Oyster, 1999] The amount of pigmentation defines the eye color. The thickness of the iris varies from 370 μm to 640 μm. [François et al., 2007] The dilation and constriction ability of the pupil allows a diameter variation from about two to eight millimetres. [Gross et al., 2008b] At high ambient brightness levels, the pupil contracts, which has the additional benefit of blocking peripheral rays that would cause aberration. At low brightness levels, the diameter increases which improves the signal-to-noise ratio. [Navarro, 2009]

To enable sharp images on the retina, the lens of the eye has the ability to change the focal length by accommodation. Besides the cornea, the lens is the second important optical element for imaging and contributes about one third to the total refraction power of the eye. Light that passing through the aqueous and the pupil is refracted at the eye lens. The lens is connected to the ciliary body by the zonular fibers. Different accommodations can be achieved through the ciliary body. The ciliary body consists of the ciliary muscles, blood vessels and connective tissue and allows to set different accommodation states by changing the shape of the lens. [Lang, 2019] The lens is made up of several layers, which means that the refractive index is not homogeneous. While the refractive index in the center is about 1.41, it is about 1.38 in the outer area. [Pedrotti et al., 2017] Since the lens has neither blood vessels nor nerves, nutrients are provided by the aqueous. Its length is about 10 mm [Bille and Schlegel, 2005] and its thickness increases with age from about 4 mm to more than 4.7 mm. [Adler, 1965] The lens is inserted into an indentation of the vitreous body. The vitreous body, also vitreous humour, is a jelly-like substance that makes up 80 % of the total volume of the eye. It helps to stabilize the eye, and the pressure causes the retina to be pressed against the choroid. [Oyster, 1999] The refractive index of the vitreous is 1.336. [Pedrotti et al., 2017]

The retina is the part of the eye that converts the imaged light into electrochemical energy and sends it further to the brain. The retina is divided into three parts. The first part is the pars iridica retinae, which is located at the back of the iris. Then, there is the pars ciliaris retinae and it is located at the back of the ciliary body. And lastly,

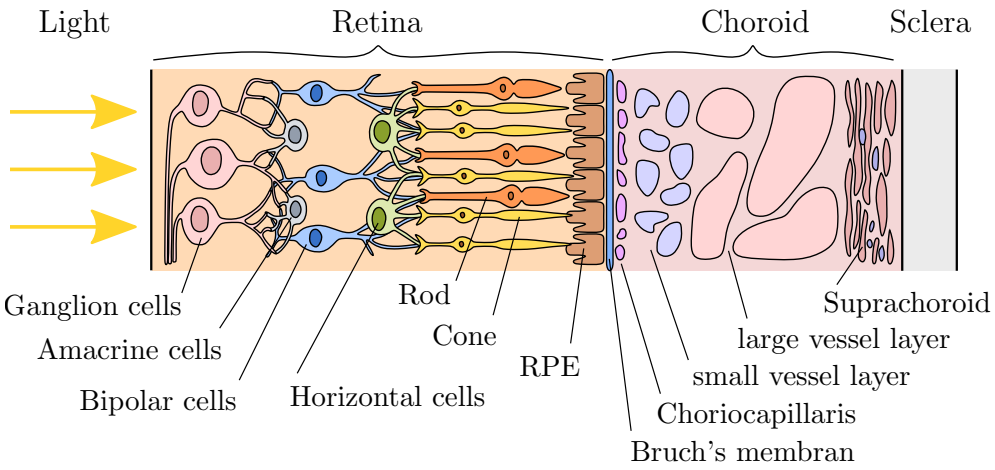

Figure 2: Structure of the retina and choroid. The light comes from the left side. On the right side of this illustration, the sclera is indicated.

there is the pars optica retinae which covers the rest of the interior of the eye. The first two parts consist only of an epithelial layer and are therefore not responsible for vision. The third part of the retina enables vision. It is referred to as sensory retina and is illustrated in Figure 2. The first layer of the sensory retina are the photoreceptors which can be divided into two types, rods and cones. The photoreceptors absorb light signals and transmit the signals to the other neuronal layers. First, the signal is transmitted to the horizontal cells, the bipolar cells and the amacrine cells. Via the ganglion cells, the processed signals are transmitted to the optic nerve which consists of about 1 million nerve fibers. [Kahle et al., 2001] The rods are highly sensitive to light and enable brightness level vision in low light environments (scotopic vision). The cones are used for color vision and function in bright environments due to their low light sensitivity. [Gross et al., 2008b] Both types are built by stacked discs whereas the rods are longer and thinner than the cones. In total, the retina has about 7 million cones and between 75 and 150 million rods. At the location where the optic nerve exits the eye, no photoreceptors are present and no vision is possible. The rods and cones are not evenly distributed. The cones are clustered in an area about 3 mm in size in the center of the retina which is referred to as macula. The fovea is the area of the retina where the sharpest vision is present. It covers a diameter of approximately 200 μm, in which cones are predominantly located. Since the measured light signals are transmitted practically directly to the optic nerve, the neuronal layer here is thinner and the fovea is formed as an indentation in the retina. Outside the macula are predominantly rods and this area is called the paramacula. The photoreceptors are directly located on the retinal pigment epithelium (RPE). Due to a high concentration of melanin, this layer is highly absorptive and therefore appears black. [Schmetterer and Kiel, 2012; Kahle et al., 2001] The RPE has a thickness of approximately 10 μm. [Lüllmann-Rauch et al.,

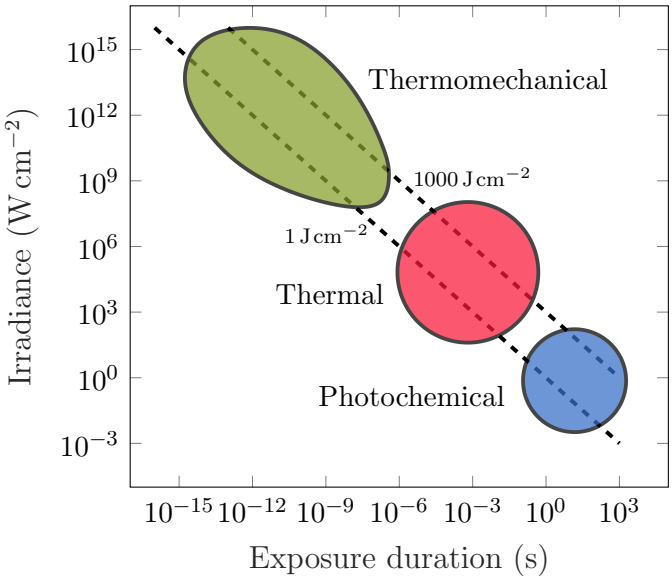

Figure 3: Occurrence of the different types of laser-tissue interaction. The colored areas indicate which type of interaction is likely to occur at the corresponding irradiance levels and exposure duration. Additionally, two diagonal dashed lines with a constant radiant exposure are plotted. Adapted with permission from [Niemz, 2004]

2019] The high absorption of the RPE suppresses scattered light, but also leads to high temperature elevations and therefore to potential retinal injuries in case of high irradiance exposures. [Ham et al., 1970; Beatrice and Steinke, 1972; Lund et al., 2000]

The choroid is located between the retina and the sclera. Figure 2 shows the general structure of the choroid which can be divided into four areas. It supplies oxygen and nutrients to the retina via the lamina vitrea, which is the boundary layer to the RPE. The lamina vitrea, or Bruch's membrane, represents the first tissue layer of the choroid and has a thickness between 2 μm and 4 μm. [Lee et al., 2006] The next area is the choriocapillaris. It is approximately between 10 μm to 30 μm thick and serves to supply nutrients. [Nickla and Wallman, 2009] The third area is the lamina vasculosa, which contains blood vessels and can be divided into Sattler's and Haller layer. Sattler's layer is close to the choriocapillaris and contains medium-sized blood vessels. The Haller layer is next to Sattler's layer and contains large blood vessels. The last layer is the lamina suprachoriodea. This consists of pigmented connective tissue cells and collagen fibers and lies directly on the sclera. [Duane et al., 1996] The permanently present blood flow in the choroid also allows heat transport. Light is strongly absorbed in the RPE layer and the RPE heats up correspondingly. The RPE also transfers some of the heat to the choroid, which is then removed by the blood flow.

5.3 Eye injuries due to optical radiation

Optical radiation refers to radiation in the wavelength range from approximately 180 nm to 1 mm. It can induce eye injuries by different laser-tissue interaction mechanisms. While the wavelength of radiation provides information on which part of the eye is most likely to be damaged, the irradiance as well as the exposure duration determine which type of damage mechanism is most likely to occur. This is shown schematically in Figure 3. A distinction is made between photochemical, thermal, and thermomechanical processes. For low irradiances and long exposure durations, a photochemical injury can occur. However, this damage mechanism can only be present at shorter wavelengths, since a certain photon energy is necessary to generate toxic radicals in the tissue. For example in sunburns, the photochemical process damages DNA, which can lead to skin cancer. The photochemical damage is of cumulative nature, meaning that it is not necessarily a single exposure leading to an injury, but multiple exposures over a long period of time. Often, photochemical damages can occur together with thermal damages. In the case of thermal damage, there are burns of the retina, which can be described as denaturation of proteins. [Birngruber et al., 1985] If temperatures above 100 °C are reached, liquids can evaporate and carbonization can occur. [Henderson and Schulmeister, 2003] In thermomechanical processes, the tissue is heated up that fast that shock waves can develop. These shock waves cause mechanical damage to the surrounding tissue. For exposure durations shorter than a few nanoseconds, the tissue becomes ionized and plasma is formed, which in turn leads to acoustic transients and shock waves. This is referred to as photodisruption.

Depending on the wavelength of the radiation, different parts of the eye can be affected. In the UV range, the cornea and lens will absorb the radiation. In the UV-C range, there is strong absorption in the cornea, causing all radiation to be absorbed in its outermost layer. With very short exposure times in the nanoseconds range and correspondingly high irradiances, photoablation takes place, whereby the irradiated part of the layer can be ablated. For example, if the eye is exposed to UV-C stray light for a long time, photochemical processes take place leading to inflammation of the cornea (photokeratitis) or conjunctiva (photoconjunctivitis). This is a typical consequence that can occur during welding work. Since the cornea renews itself after a few days, the eye can regenerate from this kind of damage. In the case of UV-B radiation, the radiation can propagate deeper into the eye and the lens can also be affected, which can lead to cataract. Since the eye cannot regenerate from this damage, surgery is often performed to replace the crystalline lens by an artificial lens. In the case of UV-A radiation, the absorption at the cornea is lower and most of the radiation is absorbed by the lens. Since the wavelength is longer in this region, damage to the lens is more

probably caused by a thermal process. If IR radiation is present, then the damage is described by thermal processes or, for short exposure times, by thermomechanical processes (ablation of tissue). While IR-A radiation is still partially imaged on the retina, IR-B and IR-C radiation can cause damages to the cornea. For longer exposure durations to IR-A and IR-B radiation, the lens is increasingly affected, which can result in a cataract.

Damages to the anterior parts of the eye are either reversible or treatable, damages to the retina, however, are irreversible. Radiation with wavelengths between 400 nm and 1400 nm reach the retina and depending on irradiance and exposure time, one of the damage mechanisms shown in Figure 3 may occur. Although it is not visible, near-infrared radiation can propagate through the ocular media with little attenuation and reach the retina. Photochemical damages occurs predominantly in the blue wavelength range up to approximately 550 nm for long exposure times [Henderson and Schulmeister, 2003] and the produced radicals may lead to retinopathy [Wu et al., 2006; Hunter et al., 2012; Ivanov et al., 2018]. For exposure durations between a few microseconds to seconds, thermal damage occurs with a denaturation process of proteins in the tissue. Since the sensory part of the retina is largely transparent, most of the radiation is absorbed in the RPE layer, which is where the damage occurs. If a cell in the RPE layer is damaged, this will lead to the degeneration of the overlaying photoreceptors of the sensory part of the retina. At even shorter exposure durations, the tissue is rapidly heated in a very short time, resulting in thermomechanical damage. Here, the fluid around the melanin particles in the RPE layer can evaporate, forming cavitation bubbles. If a shock wave spreads, this can damage the tissue and blood vessels (haemorrhage).

5.4 Laser safety of products emitting optical radiation

In this section, the focus is on the eye safety of optical products that operate lasers. For this purpose, the first guidelines for safe use were published very early, 5 years after the invention of the laser. [Ministry of Aviation, 1965] Nowadays, the International Commission of Non-Ionizing Radiation Protection (ICNIRP) provides guidelines for laser radiation. [ICNIRP, 2013b] These guidelines contain a collection of exposure limits derived on the basis of damage measurements. This is discussed in the first subsection. The second subsection addresses the laser safety standard IEC 60825-1:2014 [IEC, 2014], which refers to the exposure limits from the ICNIRP guidelines and introduces a laser classification system that enables to evaluate the potential associated risks of a laser product.

5.4.1 Definition of exposure limits

In order to determine whether a laser system can pose a potential hazard, certain conditions must be considered. For this reason, the ICNIRP guidelines contain exposure limits (ELs), also referred to as maximum permissible exposures (MPEs), which specify a radiation level below which no injury is expected to occur. These ELs are derived from damage experiments, most of which have been performed on animals such as rabbits [Cain and Welch, 1974], rats [Noell et al., 1966b], non-human primates [Marshall et al., 1975; Stuck, 1984], or enucleated porcine eyes [Schuele et al., 2005]. In such experiments, there is no clear limit between the amount of irradiation that is safe and that which causes injuries. Because of biological variability, there may be a broader range where damage may occur. Other factors that affect the width of the transition zone are experimental variables and the minimum visible lesion. For this reason, the probit curve, introduced by Finney [Finney, 1971], is used for the analysis of the experimental measurements. From this analysis, the ED_{50} value is obtained, which gives the amount of radiation for which there is a 50 % probability that damage will occur. [Sliney et al., 2002] This value is then referred to as the damage threshold. ELs are derived from these determined values using a reduction factor (RF) with no unit. This factor is often in the range of 10, but depends on the wavelength of the radiation, the exposure time, and the mechanism of damage. Generally, larger RFs are present when uncertainties are larger or when a small amount of measurement data is available. For example, when considering photochemical damage, the RFs applied here are high compared to the thermal damage range. In a study by Lund examining photochemical damage at a wavelength of 441 nm, an RF of 23 was determined [Lund et al., 2006]. For thermal damage to retinas, minimal RFs are obtained at a wavelength of 530 nm and for single pulses. [Jean et al., 2017, 2019] Since in such experiments the conditions are clearly defined and the probit analysis shows low uncertainties, RFs with the value 2 are considered as sufficiently safe. [ICNIRP, 2013b]

5.4.2 Laser safety standard

The laser safety standard IEC 60825-1:2014 [IEC, 2014] is an international standard that enables a manufacturer to classify laser product. The laser safety standard adapts the exposure limits from the ICNIRP guidelines [ICNIRP, 2013b] and provides the accessible emission limits (AELs) from them. The classification system consists of four main classes, numbered from one to four. There are various criteria for classifying a product into a particular class. These are the exposure duration, where a distinction is made between long-term exposure and short-term exposure, or the viewing condition, whether the naked eye is exposed to radiation or whether optical viewing instruments

Table 1: Overview of laser classes in the laser safety standard [IEC, 2014]. The measurement condition 3 resembles a naked eye and condition 1 the presence of optical viewing instruments. A short-term exposure refers to a duration of 0.25 s. A long-term exposure is 100 s for wavelengths above 400 nm and 30000 s otherwise. The table shows the potential danger of a laser class for different exposure conditions. The table is modified from [Henderson and Schulmeister, 2003].

Laser Class	Long-term exposure		Short-term exposure		Diffuse reflections/ Skin exposure
	Cond. 3	Cond. 1	Cond. 3	Cond. 1	
1	safe	safe	safe	safe	safe
1M	safe	hazardous	safe	hazardous	safe
2	hazardous	hazardous	safe	safe	safe
2M	hazardous	hazardous	safe	hazardous	safe
3R	hazardous	hazardous	low risk	low risk	safe
3B	hazardous	hazardous	hazardous	hazardous	low risk
4	hazardous	hazardous	hazardous	hazardous	hazardous

(such as telescopes, magnifiers or binoculars) are used. Furthermore, potential skin damage or hazards posed by scattered radiation are considered. An overview of all classes from the laser safety standard is shown in Table 1. The laser Class 1C has not been mentioned, since this is intended for an application on the skin where specific standards must be applied to the product. In principle, with a higher class comes a higher risk potential. The term of an eye safe system is used when a laser product meets the requirements of laser Class 1 according to the laser safety standard (see section 3.37 in [IEC, 2014]). For the classes listed in Table 1, the letter M represents a potential hazard for the use of magnifying optical viewing instruments. Laser systems of Class 2 do not represent a risk for short-term exposure. This class can only be present for visible laser radiation, because under exposure an aversion reaction is possible. There are two subclasses for laser Class 3. In laser Class 3R, there is a low risk in the case of a short-term direct look into the laser beam. The letter R stands for reduced or relaxed requirement. Class 3B describes laser products for which even a short-term exposure poses a risk to the eye. Diffuse reflections and irradiation of the skin present a low risk. The letter B has a historical origin from earlier versions of the laser safety standard. The highest laser class is Class 4 and represents the highest risk potential. Here, both diffuse reflections and exposure of the skin are dangerous. Such lasers often also pose an additional fire hazard. In order to assign a laser product to a class, the accessible emission (AE) is measured. This is a measured amount of radiation under defined conditions, such as the measuring distance to the product or the size of the measuring aperture. If the AE is smaller than the AEL, which is to be assigned to a certain laser class, then the requirements of the corresponding laser class are fulfilled.

6 Objectives and expected outcome of doctoral research

The goal of this thesis is to develop software-based solutions that can support eye safety calculations as well as that can be used for research purposes. Laser radiation in the visible and near infrared wavelength range is particularly complex in eye safety calculations, as this radiation is imaged on the retina of the eye. The focus of the thesis is on this subject area. Two main aspects will be addressed, namely the implementation of the evaluation schemes from the laser safety standard IEC 60825-1:2014 [IEC, 2014] and the validation of the standard by damage simulations in the thermal damage region. Several challenges are faced when an optical system is evaluated with regard to the eye safety by using simulations. These concern the choice of the propagation method and the associated generation of retinal images, as well as the correct implementation of the analysis procedure of the retinal images according to the laser safety standard. The first study of this thesis relates to the topic of retinal image analysis. By means of this analysis, it is possible to perform eye safety calculations for radiation imaged on the retina. This analysis method is developed in a general way that it can be applied both to coherent radiation according to the laser safety standard [IEC, 2014] and to incoherent radiation according to the lamp safety standard [IEC, 2006]. An incorrect implementation could lead to an underestimation of the hazard potential. The aim of this study is to introduce an unambiguous evaluation method that leads to a restrictive result. In the second study, the propagation method is investigated. A Gaussian beam, the simplest form of a laser source is placed in front of an eye in this study. By using an air-equivalent eye model, retinal images are calculated using wave optics. The retinal images are evaluated according to the method determined from the first study. Here, the question is investigated what influence wave optical effects can have in eye safety evaluations and where simplifications with analytical descriptions can be made. In the last part of this thesis, a computer model is further developed to simulate thermal injuries to the retina caused by laser radiation. The computer model allows the investigation of single or multiple pulsed laser beams with different beam profiles. The thresholds simulated with this computer model will be compared with the results of the laser safety evaluations. The reason for this investigation is that beam profiles deviating from circular symmetry have to be evaluated in a certain way according to the standard, although there is no experimental threshold data available. The aim of the investigation is to extend the threshold data by simulation and to use this data to validate the evaluation scheme from the standard.

7 Results and Discussion

The investigations and results made within the scope of this thesis were published in three publications, which can be viewed in the appendix. In the first study, the requirements for an eye safety calculation according to the laser safety standard [IEC, 2014] are listed in detail and are digitally implemented. The focus here is specifically on radiation that is imaged on the retina. The newly developed image analysis method allows an eye safety evaluation which is applied to retinal images. The image analysis is developed in such a general way that it also meets the requirements for incoherent radiation according to the lamp safety standard [IEC, 2006]. The detailed study can be viewed in the appendix A3. The second study deals with the consideration of Gaussian beams in terms of eye safety. On the basis of the air equivalent eye model, wave propagation is used to simulate the retinal images for different input parameters of the Gaussian beam. The obtained retinal images are then evaluated using the image analysis. An analytical formula is derived and validated, which allows an eye safety evaluation without the need of simulating retinal images and analysing them. The corresponding results can be seen in detail in the paper from appendix A1. In the last study, a computer model is further developed with which thermal retinal damage can be simulated. By comparing the simulated thresholds to the calculated limits, the evaluation procedure according to the laser standard and thus the image analysis procedure is validated. The entire study is presented in the paper in appendix A2.

The first study deals with the correct digital implementation of the laser safety standard and the development of a general evaluation scheme. As it can be seen in Fig. 4, the wavelength of the radiation is decisive for which part of the eye can potentially be damaged. In an experiment performed by Boettner and Wolter [Boettner and Wolter, 1962; Boettner, 1967], the spectral transmittance of different parts of the eye was measured. In their studies, eyes from several subjects of different ages were enucleated. The results are shown on the left side of the Figure 4. The transmittance is plotted for wavelengths from 250 nm to 2500 nm. Based on these measured data, the corresponding penetration depths of the wavelength regions into the eye parts are indicated on the right side of Figure 4. It can be seen that not only visible light is imaged on the retina, but additionally IR-A radiation. For this wavelength range, the anterior optical media, i.e. the cornea, the aqueous, the lens, and the vitreous, are largely transparent. Only for wavelengths above about 1150 nm the transmittance of the anterior media is low and a reduced amount of radiation energy reaches the retina. Radiation that is imaged on the retina poses an especially high hazard potential, since the focus ability of the eye allows the radiation to be imaged on a small area. Here,

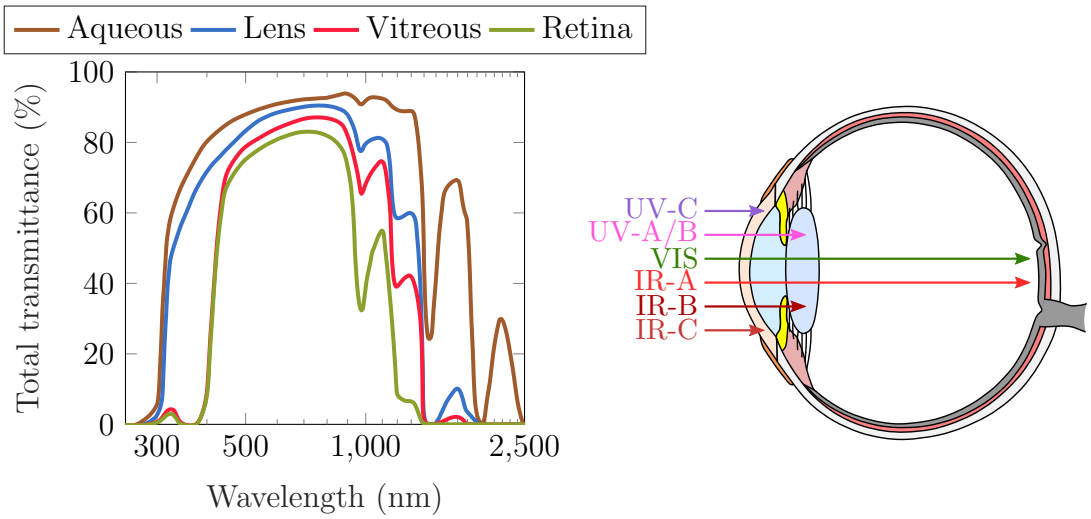

Figure 4: Depiction of the spectral transmittance characteristic of the human eye. Left: Total transmittance measured at the anterior surface of the corresponding eye part (Adapted with permission from [Boettner and Wolter, 1962; Boettner, 1967]). Right: Sketch of the penetration depth of the different regions of optical radiation into the eye.

the irradiance can increase by a factor of up to 10^5. [Niemz, 2004] Because of this focus ability, the thresholds for retinal damages can be much lower than for damages to the other parts of the eye. For UV-C radiation as well as for IR-C radiation, most of the radiation is absorbed at the cornea. In the UV-B range, the radiation can propagate deeper and reaches the lens. Any damage here can affect both the cornea and the lens. For even longer wavelengths in the UV-A range, the transmittance of the cornea is higher, which is why most of the radiation is absorbed by the lens. Wavelengths in the IR-B range are absorbed in both the cornea and the lens. The laser safety standard provides a set of accessible emission limits (AELs) which are dependent on the wavelength of the radiation to cover all possible eye injuries. In the following, the focus is on radiation that is imaged on the retina which refers to wavelengths between 400 nm and 1400 nm. In case of a retinal image which spans over an area larger than about 25 μm, it is called an extended source and allows an increased AEL. To perform corresponding eye safety evaluations, the retinal image has to be analysed. For this purpose, it is necessary to introduce an eye model which is used to create these images from arbitrary laser sources. Such an eye model is shown in Fig. 5. To fulfill the requirements from the laser safety standard, the air equivalent eye model shows a 7 mm diameter aperture stop, an ideal lens and a plane detector representing the retina. The plane detector has the distance d_2=17 mm to the ideal lens. The focal length f is variable between 17 mm and 14.53 mm realizing accommodation distances between 10 cm and infinity. An essential part of the eye safety evaluation is to measure

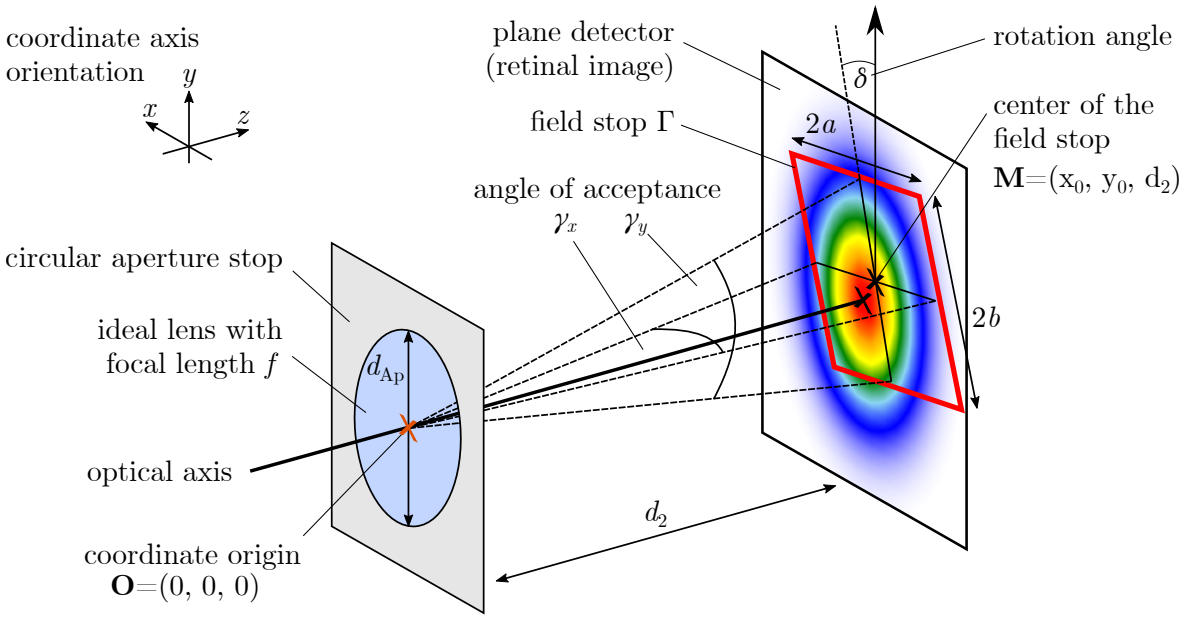

Figure 5: Illustration of the air equivalent eye model. The model consists of a circular aperture stop, an ideal lens and a plane detector. Furthermore, the field stop Γ is shown which is used for measuring the accessible emission. The field stop spans the two angles γ_x and γ_y which is referred to as angle of acceptance.

the accessible emission (AE). This is done by placing a field stop Γ into the retinal image and determining the radiant energy contained therein. The field stop has several degrees of freedom. It can be placed at any location (x_0,y_0) on the retina and can be rotated by an angle δ. Though Fig. 5 only shows a rectangular shaped field stop, it can also be elliptical. The two half widths of Γ, a and b, are also varying parameters with the restriction that the angle of acceptance γ_x and γ_y have to be within $\alpha_{\min}$ and $\alpha_{\max(t)}$. These limitations are defined in the laser safety standard and the maximum limitation is dependent on the emission duration t. As mentioned earlier, the AEL can be increased for larger retinal images. This increase is defined by the angular subtense of the apparent source α which represents the image size and is between the minimum and maximum limitation. However, there is no explicit definition available and using common beam diameter definitions, e.g. the FWHM or the d_{63}-diameter, can lead to an underestimation of the hazard potential. For this reason, a general evaluation scheme to obtain this parameter is developed. In principle, this is achieved by varying all possible configurations of the field stop for either a rectangular or an elliptical shape. For a specific configuration, the AE is determined and the averaged value of γ_x and γ_y, namely γ, goes into the evaluation of the AEL. The angles γ_x and γ_y are clearly

defined by

$$\gamma_x(x_0, y_0, a, b, \delta) = \arccos\left(\frac{x_0^2 + y_0^2 - a^2 + d_2^2}{\sqrt{{d_2}^2 + (x_0 + a\,\cos\delta)^2 + (y_0 - a\,\sin\delta)^2}} \right. \\ \left. \times \frac{1}{\sqrt{{d_2}^2 + (x_0 - a\,\cos\delta)^2 + (y_0 + a\,\sin\delta)^2}} \right), \tag{1}$$

$$\gamma_y(x_0, y_0, a, b, \delta) = \arccos\left(\frac{x_0^2 + y_0^2 - b^2 + d_2^2}{\sqrt{{d_2}^2 + (y_0 + b\,\cos\delta)^2 + (x_0 + b\,\sin\delta)^2}} \right. \\ \left. \times \frac{1}{\sqrt{{d_2}^2 + (y_0 - b\,\cos\delta)^2 + (x_0 - b\,\sin\delta)^2}} \right). \tag{2}$$

On this basis, the image analysis to obtain α is defined by

$$\left\{ \Gamma(x_0, y_0, a, b, \delta) \middle| \max \frac{\mathrm{AE}\,(\Gamma)}{\mathrm{AEL}\,(\gamma)} \right\} \Bigg|_{\gamma=\alpha\ (\gamma_x=\alpha_x, \gamma_y=\alpha_y)} . \tag{3}$$

The angular subtense α is derived from the configuration that gives the highest value and therefore the most restrictive result. This procedure can also be applied to the eye safety evaluation of incoherent sources as it also fulfills the requirements of the lamp safety standard. [IEC, 2006]

In case of coherent radiation where the laser safety standard applies, the AEL shows up to three different dependencies on the angle of acceptance. These dependencies can be expressed by the piecewise defined function κ^{C}

$$\kappa^{\mathrm{C}}\,(\gamma) = \begin{cases} \gamma, & \text{if } t \leq T_2\,(\gamma) \\ \gamma\, 10^{-\frac{\gamma}{394\,\mathrm{mrad}}}, & \text{if } t > T_2\,(\gamma) \\ \gamma\, 10^{-\frac{7\gamma}{394\,\mathrm{mrad}}}, & \text{if } t > T_2\,(7\gamma) \ \text{ and (M)} \end{cases} . \tag{4}$$

The time T_2 is a parameter from the laser safety standard and represents an emission duration for which eye movements lead to a blurred retinal image. This is the reason that the AEL remains constant for emission duration larger than T_2. The designation (M) refers to the magnifying condition where viewing aids like a telescope or binoculars are used. This condition leads to an increase in the size of the retinal image by a factor of 7.

To investigate the effect of these three dependencies on the determination of the angular subtense, a radial symmetric Gaussian distribution is examined as a retinal image. The width of the distribution was varied and with the image analysis the value

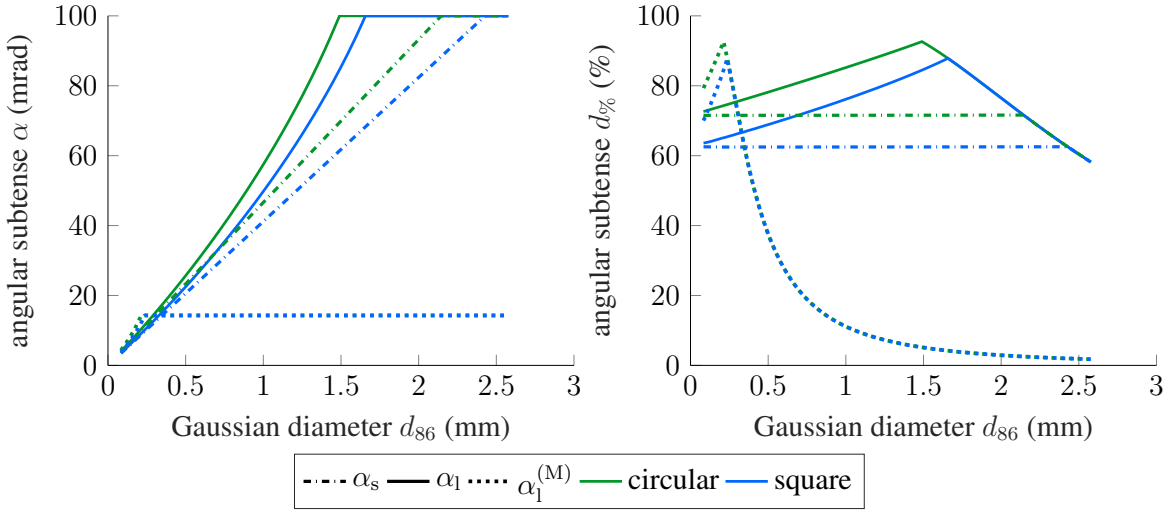

Figure 6: Results of the image analysis for a Gaussian distribution with a varying width d_{86}. The short-time, long-time and long-time-magnifying α values are evaluated for a circular and a square field stop. On the left side, the angular subtense is plotted and on the right side this value is recalculated to a $d_{\%}$-diameter for the corresponding distribution.

of α was determined. The obtained values are denoted as short-time (α_s), long-time (α_l) and long-time-magnifying ($\alpha_l^{(M)}$) representing the different cases for AEL from equation (4) from top to bottom. The results are shown in Fig. 6 where a maximum limitation of 100 mrad is assumed. The kinks in the plot come from the maximum limitation of the angular subtense. In case of the long-time-magnifying result, the kink appears for smaller distribution widths than for the other two α values. Generally, the angular subtense is the highest for the long-time-magnifying method and the lowest for the short-time method. Another important result is that the α does not follow a specific beam diameter definition which can clearly be deduced from the right plot of Fig. 6. The only exception is for $\alpha_s < \alpha_{max}$ where the corresponding $d_{\%}$-diameter stays approximately constant for a varying distribution width. For a square shaped field stop, the angular subtense can be given by the $d_{62.5}$-diameter and for a circular shaped field stop, it can be given by the $d_{71.5}$-diameter. Furthermore, when comparing both possible field stop shapes, the use of a square field stop yields smaller angular subtenses and more restrictive results than a circular field stop. As this evaluation is performed on a radial symmetric retinal image, it is not necessary to vary the rotation angle δ of the field stop.

To point out the importance of the rotation, a further retinal image is investigated. Since it does not matter whether the field stop or the image itself is rotated, the procedure in which the retinal image is rotated was chosen. The investigated retinal image shows an elliptical Gaussian irradiance distribution with the $1/e$-widths of 25 μm

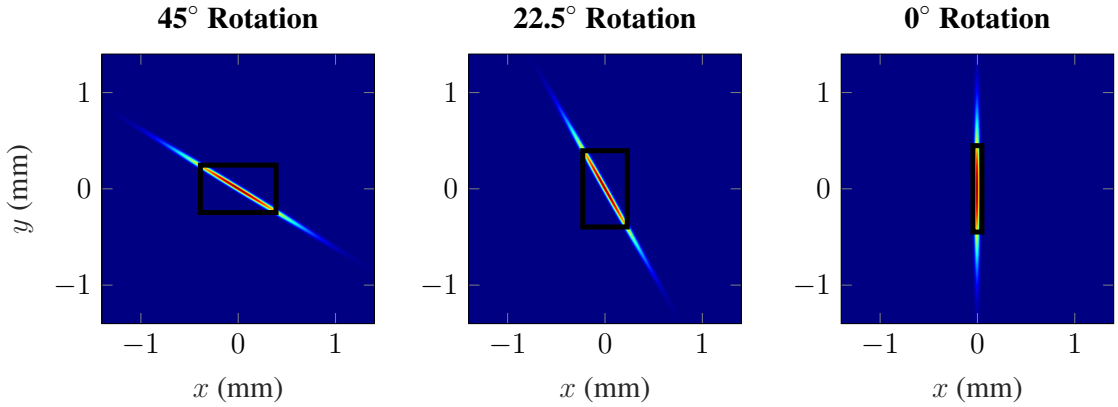

Figure 7: Image analysis of a retinal image with an elliptical Gaussian irradiance distribution. The image is rotated by 45° (left), 22.5° (center) and 0° (right). The obtained α values are shown by the black rectangles and are listed in Table 2.

Table 2: Determined α values of the three differently rotated images in Fig. 7.

Angular subtense \ Rotation angle	45°	22.5°	0°
α_x (mrad)	45.73	26.91	5.44
α_y (mrad)	28.97	46.61	52.78
α (mrad)	37.35	36.76	29.11

and 700 μm along both orthogonal directions. The image analysis is performed with rectangular shaped field stops and the long-time method with a maximum limitation of 100 mrad. The rotation angles are set to 45°, 22.5° and 0° and the results can be seen in Fig. 7 and Table 2. As one would intuitively expect, the smallest and most restrictive result is obtained for the case where the field stop is aligned along the elliptical Gaussian irradiance distribution. The results from Fig. 7 decrease from left to right. Comparing the results between 45° and 0°, there is a deviation of about 28.3 % for the angular subtense. If a complete eye safety evaluation is performed where a static retinal image is assumed for long times, then a 22.3 % higher laser power would be obtained for the image rotated by 45° and therefore the hazard potential would be greatly underestimated. In general, rotation is necessary to find the most restrictive case. If the retinal image has at least one axis of symmetry, then a rotation from 0° to 45° needs to be performed. For any retinal image, due to the symmetry of the field stops, the rotation angle has to be varied from 0° to 90°.

Another improvement that comes with the image analysis presented here is the treatment of multiple wavelengths. According to the laser safety standard, there is only an implicit specification here as well. If a laser system has multiple sources of different wavelengths in the visible and near-infrared region, the retinal image must be

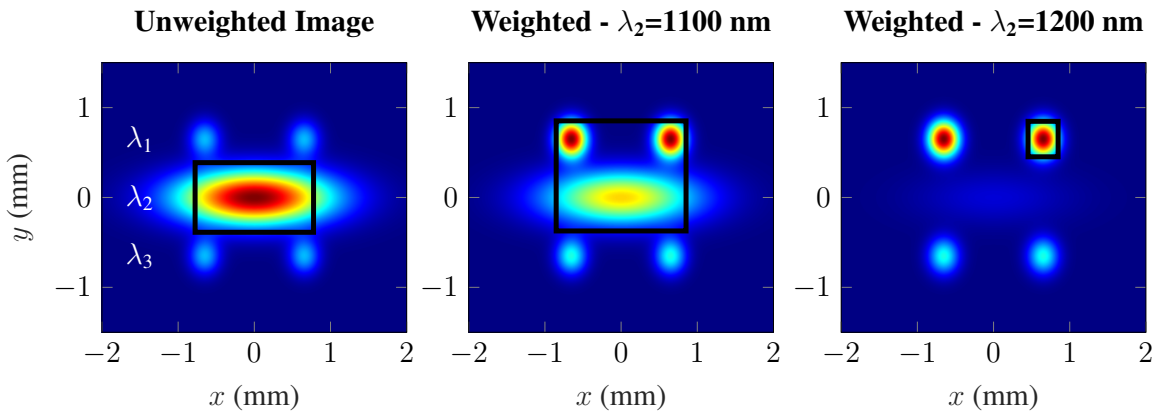

Figure 8: Left: Unweighted retinal image consisting of three different wavelengths λ_1=400 nm, λ_2 and λ_3=900 nm. Center: Weighted retinal image for λ_2=1100 nm. Right: Weighted retinal image for λ_2=1200 nm. The black rectangles show the angular subtense α for each image.

given in terms of a spectral irradiance distribution.

To apply the image analysis on these systems, a weighted retinal image is necessary. The weighting is done by integrating the spectral irradiance multiplied by the reciprocals of the correction factors C_4 and C_7. These correction factors are defined in the laser safety standard and in an extended form they are given by

$$C_4(\lambda) = \begin{cases} 1, & \text{if } \lambda \in [400\,\text{nm}, 700\,\text{nm}) \\ 10^{\frac{0.002}{\text{nm}}(\lambda - 700\,\text{nm})}, & \text{if } \lambda \in [700\,\text{nm}, 1050\,\text{nm}) \\ 5, & \text{if } \lambda \in [1050\,\text{nm}, 1400\,\text{nm}) \end{cases}, \tag{5}$$

$$C_7(\lambda) = \begin{cases} 1, & \text{if } \lambda \in [400\,\text{nm}, 1150\,\text{nm}) \\ 10^{\frac{0.018}{\text{nm}}(\lambda - 1150\,\text{nm})}, & \text{if } \lambda \in [1150\,\text{nm}, 1200\,\text{nm}) \\ 8 + 10^{\frac{0.04}{\text{nm}}(\lambda - 1250\,\text{nm})}, & \text{if } \lambda \in [1150\,\text{nm}, 1400\,\text{nm}) \end{cases}. \tag{6}$$

In the following, the retinal image shown in Fig. 8 is analysed. The image is constructed so that the top two spots have the wavelength λ_1=400 nm, the middle spot has the wavelength λ_2 and the bottom two spots have the wavelength λ_3=900 nm. Fig. 8 also shows the weighted retinal images for two different values of λ_2. Applying the image analysis using the short-time method and a rectangular field stop with a maximum limitation of 100 mrad leads to the results listed in Table 3. It can clearly be seen that due to the weighting of the image, the maximum irradiance level shifts to the upper two spots. The reason for that is that the correction factor C_7 increases for higher wavelengths and thus reducing the weighted irradiance. In case of λ_2=1100 nm the weighting leads to comparable irradiances to the upper two spots and the α results

Table 3: Results for the angular subtenses of the retinal images shown in Fig. 8.

Result \ Retinal Image	Unweighted	Weighted λ_2=1100 nm	Weighted λ_2=1200 nm
x_0 (μm)	0	0	650
y_0 (μm)	0	240	650
α_x (mrad)	91.41	100	23.23
α_y (mrad)	45.58	72.03	23.23
α (mrad)	68.49	86.01	23.23

enclose the spots for λ_1 and λ_2. For λ_2=1200 nm only the upper two spots are decisive for the α determination. If a detailed eye safety evaluation is made based on the results for the unweighted retinal image, then a radiation power with a factor of 10 higher than allowed would be obtained. This shows the importance of a correct weighting in eye safety evaluations of laser systems having multiple wavelengths.

In summary, in this study a general evaluation procedure was developed that can be used for eye safety evaluations of radiation in the visible and near-infrared wavelength region. With this procedure, an explicit definition of the angular subtense of the apparent source is introduced for the first time. According to the standards, there is a free choice regarding the shape of the field stop which is used for the evaluation. It was found that the use of a rectangular shape leads to more restrictive results than for an elliptical shape. Another important finding is that the angular subtense of the apparent subtense is not a characteristic value of a laser source, but must be derived from the retinal image and can have several values. In total, three different methods were found to determine α, which are referred to as short-time, long-time and long-time-magnifying method. In addition to the AELs that depend on the angular subtense, there are also the so-called photochemical limits. For these limits a slightly different image analysis has to be used which can be derived from the developed algorithm in equation (3). As the photochemical limits provide a fixed angle of acceptance γ, there is no need to vary the widths of the field stop in the algorithm. Therefore, the image analysis covers all kind of retinal limits from the laser safety standard and even the lamp safety standard. Regarding the lamp safety standard, the provided procedure also improves the definition for the angular subtense and provides the most restrictive results.

The results obtained in this study provide a fundamental basis for eye safety evaluations. The investigations done here can be repeated in a future study on a larger set of different retinal images. This would allow a stronger statement about the characteristics of the image analysis. This concerns statements like that the use of a rectangular field stop is more restrictive than an elliptical one or that the long-time method always leads to more restrictive results than the short-time method. Another point that can be

discussed in more detail is the required computational power. In the procedure presented here, a variation of many parameters is foreseen, which can be time-consuming from a computational point of view. Since a complete eye safety evaluation of a laser product does not include the consideration of a single retinal image, but a multitude, as different accommodation states and distances to the laser source have to be taken into account, this problem is aggravated. For this reason, algorithms that can optimize different calculation steps or that point to the most restrictive results are needed.

The second study focuses on the wave optical properties of laser radiation and its influence on eye safety evaluations. Physically, the light that can be perceived with human vision can be described by an electromagnetic wave in a specific wavelength range. An electromagnetic wave is a transverse wave in which the direction of propagation, the the electric field vector and the magnetic field vector are perpendicular to each other. Electromagnetic waves satisfy the wave equation

$$\Delta\vec{E} - \epsilon\epsilon_0\mu_0\frac{\partial^2\vec{E}}{\partial t^2} = 0 \tag{7}$$

which arises from Maxwell's equations assuming non-conducting materials. [Zinth and Zinth, 2013] Here $\vec{E}$ is the electric field vector, ϵ_0 is the vacuum permittivity, ϵ is the relative permittivity, μ_0 is the vacuum magnetic permeability, and t is the time. A laser beam is also an electromagnetic wave and is described in its simplest form by a Gaussian beam. Gaussian beams are solutions of the Helmholtz equation, which is a time-independent form of the wave equation. To the concept of Gaussian beams belongs a set of solution sets, which are called Gaussian modes. In this study, a Gaussian beam is considered in the most fundamental mode, the TEM_{00} mode, which is given by the irradiance distribution

$$I(r,z) = \frac{2}{\pi w(z)^2}\exp\left(-2\frac{r^2}{w(z)^2}\right), \tag{8}$$

where the z-axis is the optical axis and r the radial distance to it. The parameter $w(z)$ refers to the $1/e^2$-width of the distribution and follows

$$w(z) = w_0\sqrt{1+\left(\frac{z-z_0}{z_\mathrm{R}}\right)^2} \tag{9}$$

with the beam waist w_0 and the Rayleigh length z_R

$$z_\mathrm{R} = \frac{\pi}{\lambda}w_0^2. \tag{10}$$

The Gaussian beam is therefore completely characterized by setting a wavelength λ and a beam waist w_0. The width $w(z)$ in equation (9) represents the wave optical propagation of the Gaussian beam in the free space in terms of the Fresnel-Kirchhoff diffraction equation [Zinth and Zinth, 2013]. A propagating Gaussian beam shows a broadening of the distribution and a divergence angle can be calculated according to

$$\theta = \frac{2\lambda}{\pi w_0}. \tag{11}$$

As the retinal images are needed for the eye safety evaluation, the propagation through the air equivalent eye model from Fig. 5 has to be considered. This is done by a computer simulation where the diffraction equation is solved. The essential propagation steps are at first a translation with distance d_1 which is the distance between the beam waist and the eye model. Afterwards the truncation at the circular aperture with radius r_A is calculated. Then the refraction at the ideal lens with the focal length f is taken into account and at last a translation with the distance d_2=17 mm to the retina is performed. The simulated retinal images are analysed with the image analysis from equation (3) where the angular subtense of the apparent source is obtained. In addition, Gaussian beams have a special feature in the fields of eye safety. These beam profiles are the only exception with an explicit definition for the angular subtense α. Here, according to the laser safety standard, the d_{63}-diameter of the distribution can be used for the determination of α. This approach is commonly used where an analytical formula for the distribution width on the retina is applied. This formula is given by

$$w_r = w_0 \sqrt{\left(1 - \frac{d_2}{f}\right)^2 + \left(\frac{1}{z_\mathrm{R}}\right)^2 \left(d_1 + d_2\left(1 - \frac{d_1}{f}\right)\right)^2}. \tag{12}$$

Since the truncation effect of the circular aperture lead to a limited application, an extended analytical formula is presented in this study. Here, the calculation of α is done by the piecewise function

$$\alpha = \begin{cases} 2\arctan\frac{w_r}{\sqrt{2}d_2} & \frac{w_0}{\sqrt{2}}\sqrt{1+\frac{d_1^2}{z_\mathrm{R}^2}} < r_\mathrm{A} \\ 2\arctan\frac{w_r^t}{d_2} & \frac{w_0}{\sqrt{2}}\sqrt{1+\frac{d_1^2}{z_\mathrm{R}^2}} \geq r_\mathrm{A} \end{cases}. \tag{13}$$

The width w_r^t represents a truncated Gaussian distribution and is defined by

$$w_r^t = r_\mathrm{A} \sqrt{\frac{\left(1 - \frac{d_2}{f}\right)^2 + \left(\frac{1}{z_\mathrm{R}}\right)^2 \left(d_1 + d_2\left(1 - \frac{d_1}{f}\right)\right)^2}{1 + \left(\frac{1}{z_\mathrm{R}}\right)^2 d_1^2}}. \tag{14}$$

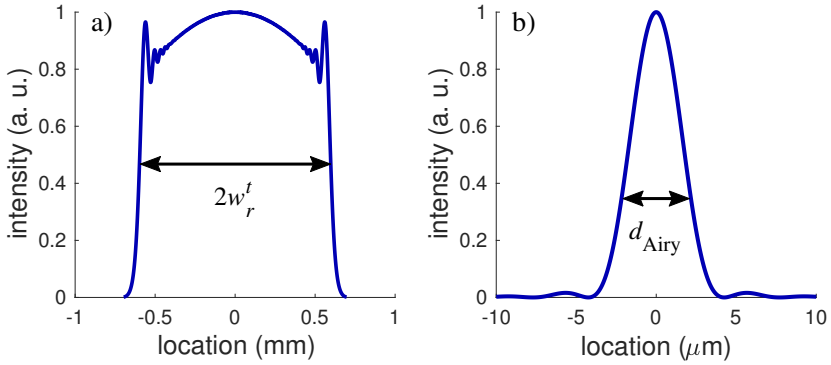

Figure 9: Simulation of retinal images for a Gaussian beam with $w_0 = 10\,\mathrm{mm}$ and for a wavelength of $\lambda = 1400\,\mathrm{nm}$ where in plot a) the eye accommodates to a distance of 10 cm and in plot b) the eye accommodates to infinity.

In the following, the applicability of this newly introduced formula is investigated by an comparison with the results obtained by the computer simulation.

In a first investigation, the effect of the circular aperture on the simulated retinal images is considered. For this purpose, a Gaussian beam with a waist of w_0=10 mm is considered which has a larger size than the circular aperture diameter. The retinal images can be seen for two different accommodation states in Fig. 9. As the Gaussian beam has a radially symmetric irradiance distribution, the plotted retinal images depict one slice within the retinal area. Due to the truncation of the Gaussian beam, the outer parts of the distribution are cut off in the left plot of Fig. 9. The resulting width can be described very well with the parameter w_r^t from equation (14). In this example, this diameter is about 1.2 mm. In case of the right plot of Fig. 9, the so-called 'Airy disc' appears. Here, the accommodation to infinity projects the far field diffraction pattern of the circular aperture into the focal plane. The size of the distribution can be estimated with

$$d_{\mathrm{Airy}} \approx 1.22 \frac{\lambda}{2r_{\mathrm{A}}} d_2 \approx 4.1\,\mu\mathrm{m}. \tag{15}$$

The laser safety standard also includes this effect of a minimal retinal image size. For this reason, there is the minimum limitation α_{min}=1.5 mrad which corresponds to an absolute size of about 25 μm. This is larger than the diameter of the Airy disc, but this value refers to an approximate size of how it is actually imaged in the human eye, where for example scattering effects prevent a perfect minimum spot size.

The study is divided into two sections. At first, collimated Gaussian beams are considered and afterwards divergent Gaussian beams are analysed. The wavelength region that is imaged on the retina goes from 400 nm to 1400 nm and the whole study was performed for the smallest and largest wavelength. As the results is the same for both wavelengths, only the analysis for the wavelength 400 nm is shown. For a collimated beam, the beam divergence angle is small enough so that the influence

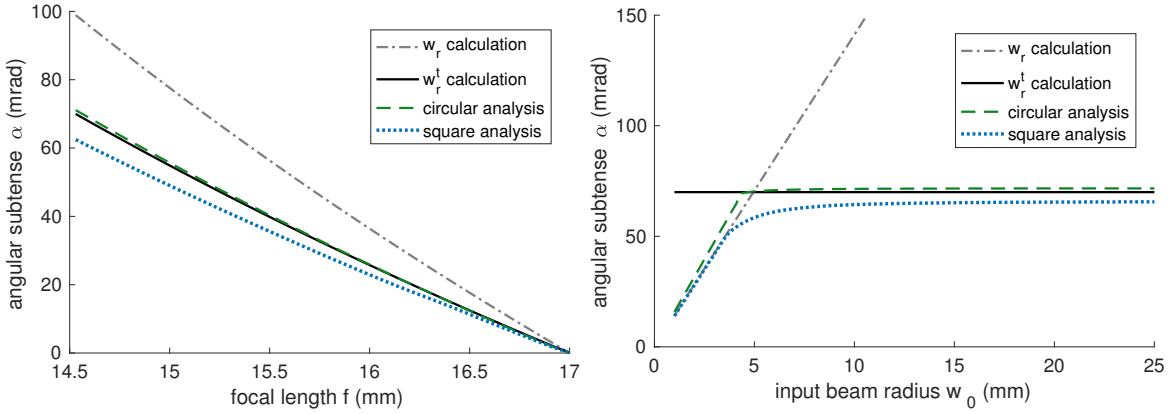

Figure 10: Determination of the angular subtense α for a collimated Gaussian beam with the wavelength 400 nm. Left: The beam waist is set to 7 mm and the focal length f of the eye model is varied. Right: The focal length is set to 14.53 mm and the beam waist is varied.

of the distance d_1 between the beam waist and the eye model is negligible and is therefore set to 0 mm. A Gaussian beam was considered to be collimated in case of a divergence angle smaller than 0.5 mrad. The results for the angular subtense for a varying focal length of the eye model and a varying beam waist w_0 are plotted in Fig. 10. For the analytical evaluation, both cases of equation (13) are shown regardless of the corresponding conditions. In addition, two image analyses were performed where a square and a circular shape of the field stop was used. In the left plot of Fig. 10, it can clearly be seen, that the α determination using w_r from equation (12) yields too large values underestimating the potential hazard. The calculation according to w_r^t from equation (14) lies within the results determined with the image analysis. In the right plot of Fig. 10 where the beam waist is varied, it shows that for certain regions either w_r or w_r^t is an appropriate choice for α. The image analysis shows a kink at about 4 mm. This means that for smaller beam waists, the Gaussian beam is not big enough so that a significant truncation at the circular aperture appears affecting the image. The conditions in the piecewise function from equation (13) represents the intersection point between w_r and w_r^t. This means that for small beam waists w_r applies and for larger beam waists w_r^t applies. This combined curve lies within the image analysis result. Another interesting finding is that there is a maximum retinal image size. For an increasing beam waist, the image analysis shows a saturation in the right plot of Fig. 10 at about 72 mrad. As a higher focal length leads to smaller retinal images, a collimated Gaussian beam can therefore not produce spot sizes larger than 1.2 mm.

In the second half of this study, divergent Gaussian beams are considered with divergence angles higher than 0.5 mrad. The results are shown in Fig. 11. In the left plot, the Gaussian beam has a divergence angle of 51 mrad and is positioned far away enough from the eye model so that truncation occurs. Therefore, the α determination

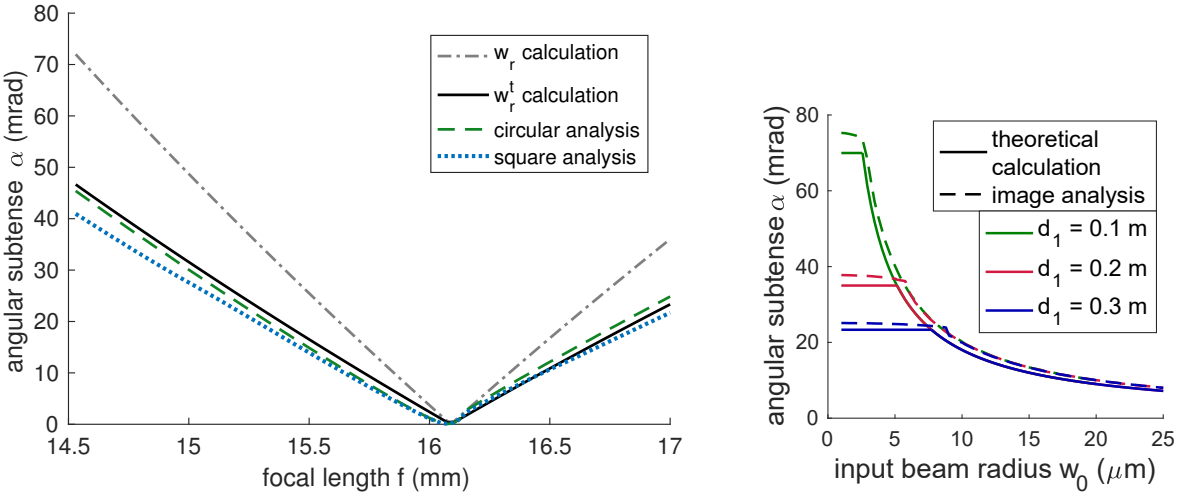

Figure 11: Evaluation of the angular subtense α for divergent Gaussian beams with a wavelength of 400 nm. Left: Varying the focal length of the eye model with a beam waist of 5 μm and a distance of d_1=0.3 m. Right: Varying the beam waist for a fixed focal length at 17 mm where only the piecewise function in equation (13) and the image analysis using a circular field stop are shown. Here, the distance d_1 was set to 0.1 m, 0.2 m and 0.3 m.

using the w_r calculation from equation (12) is leading to incorrectly high results. The evaluation using the w_r^t equation shows smaller α values and shows sufficiently restrictive results when compared to the image analysis. The angular subtense α reaches the minimum limitation of 1.5 mrad for a focal length at about 16.1 mm. This focal length refers to an accommodation distance of 0.3 m where the beam waist is located. The right plot of Fig. 11 shows the image analysis results using a circular field stop and the results obtained by the piecewise function from equation (13) for different divergent beam configurations. Due to a variation of the beam waist, a kink appears in the plot which represents a change in the retinal image behavior due to truncations. The truncation appears in this case for smaller beam waists as a smaller beam waist leads to higher divergence angles and therefore higher beam diameters at the circular aperture stop. The results by the newly developed analytical formula yields restrictive and correct results.

In summary, the study was performed on all possible configurations of a circular symmetric Gaussian whereby the most important results were shown. Based on the results made, it can be clearly said that the new formula introduced here produces restrictive results and is validated by a comparison with the computer simulations. Furthermore, it addresses the current gap in the state of the art, where the hazard potential can be severely underestimated. A further interesting result can be seen in the image analysis when comparing both possible field shapes. The use of a square field shape leads to smaller angular subtenses than a circular field stop and is therefore more

restrictive. A further interesting question in this area arises when elliptical or simple astigmatic Gaussian beams are investigated with regard to the eye safety. Since these beam profiles have two different beam waists, the question arises whether the formula presented here can be applied separately to both axes and whether the comparison with the image analysis also validates it. Such a study is more extensive, since these systems show additional degrees of freedom. Furthermore, in this study ideal Gaussian beam with a perfect coherence where investigated. In reality, laser beams can deviate from this, which is described by means of the M^2 factor. Here, a value of one represents an ideal Gaussian beam and a larger value leads to a different relationship between the beam waist and the beam divergence and to a partial coherence. Such beam profiles can be described by the Gaussian Schell-model [Sudol and Friberg, 1984]. In a further study where this model is used, the influence of partial coherence can be investigated. This leads to a weakening of the truncation effect, which can increase the retinal image size leading to higher α values. Here, the analytical calculation formula must take this effect into account and has to be adjusted. This formula can then be validated by further computer simulations.

In the last study of this thesis, a three-dimensional computer model was developed to simulate retinal thermal injuries. The peculiarity in the study is that irradiance profiles which are not radially symmetric are considered. According to the laser safety standard, an averaged size of the retinal image goes into the eye safety evaluation. However, currently there is no experimental data on which this procedure is based on. For this reason, the data set is extended simulatively with the computer model and thus the evaluation procedure of the standard is validated.

The computer model to simulate retinal thermal injuries can be divided into three steps which is sketched in Fig. 12. At first, an eye model is used to calculate the retinal image from a laser source. Here, the LeGrand eye model [LeGrand and ElHage, 1980] is applied where also the transmittance characteristics from Fig. 4 are included. To take intraocular scattering into account, the following effective transmittance is used which depends on the total transmittance τ_{Total}, the retinal image size r_{Spot} and the wavelength λ of the radiation

$$\tau_{\mathrm{eff}}\left(\lambda, r_{\mathrm{Spot}}\right) = \tau_{\mathrm{Total}}\left(\lambda\right)\left(1 - \frac{1}{2}\exp\left(-\frac{\lambda}{883\,\mathrm{nm}}\right)\exp\left(-\frac{2r_{\mathrm{Spot}}}{600\,\mu\mathrm{m}}\right)\right). \tag{16}$$

The expression in the bracket is multiplied by the total transmittance and represents the effect of intraocular scattering. Depending on the wavelength of the radiation and the retinal spot size, the scattering can reduce the transmittance up to about 30 %. Furthermore, the eye model is based on paraxial approximations and includes chro-

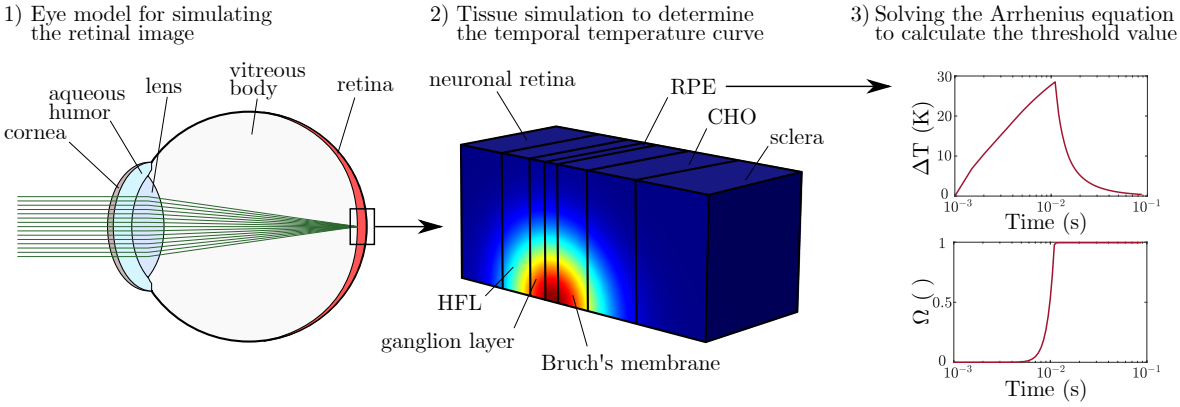

Figure 12: Evaluation steps to simulate retinal thermal injuries of laser radiation in the visible and near-infrared region. In the first step, the retinal image is evaluated by using an eye model. In the second step, the retinal tissue is simulated by finite elements and the heat source is derived from the retinal image. In the third step, the simulated temperature of the RPE layer is inserted into the Arrhenius equation to obtain the threshold value.

Table 4: Thermal characteristics of the simulated retina for evaluating the heat transfer.

thermal characteristic	value
conductivity k	$0.6305\,\frac{\mathrm{W}}{\mathrm{m\,K}}$
specific heat C	$4178\,\frac{\mathrm{J}}{\mathrm{kg\,K}}$
density ρ	$992\,\frac{\mathrm{kg}}{\mathrm{m}^3}$
initial temperature T_0	$310.5\,\mathrm{K}$

matic aberration which has the most dominant influence on the spot size. Aberrations of higher modes like spherical aberrations or astigmatism are not considered since their effects on the retinal spot are limited and are implicitly covered by intraocular scattering [Jean and Schulmeister, 2014a]. In the next step, the retinal tissue is realized in a three-dimensional model using finite-elements. The simulated layer are the neuronal retina, Henle's fiber layer (HFL), ganglion layer, Bruch's membrane, RPE, choroid (CHO) and the sclera as illustrated in Fig. 12. Each layer is constructed by multiple tetrahedons where for each element the heat transfer equation in biological tissue is solved

$$\rho C \frac{\partial T}{\partial t} = k\Delta T + q\left(t, \vec{r}\right) + q_b\left(T\right). \tag{17}$$

The tissue is characterized by the thermal properties from Table 4. The term $q_b\left(T\right)$ represents the heat dissipation due to the blood flow in the choroid layer. The heat source is given by the term $q\left(t, \vec{r}\right)$ and defines the amount of energy of the retinal image that is responsible for heating up the retinal layer. In general, for each wavelength there are different penetration depths and thus the heat source has a strong dependence on it. However, the most amount of radiation energy is absorbed by the RPE [Ham et al.,

1970; Beatrice and Steinke, 1972; Lund et al., 2000] and the retinal thermal injuries appears in this layer. Therefore, the simulated temperature rise within the RPE layer is of further interest. To simulate the injury, the Arrhenius equation is used

$$\Omega\left(t\right) = A \int_0^t \exp\left(-\frac{E}{RT(t')}\right) \mathrm{d}t'. \tag{18}$$

The parameter A is a frequency factor and set to $1.05 \times 10^{95}\,\mathrm{s}^{-1}$ and E is the inactivation energy and equal to $5.99 \times 10^5\,\mathrm{J/mol}$. This equation describes the denaturation of proteins and the temporal temperature curve $T(t)$ has to be inserted. The process of a denaturation is defined for Ω equals one. A retinal thermal injury is defined for a circular area with a diameter of $20\,\mu\mathrm{m}$ within the RPE for which all contained points fulfill the condition $\Omega \leq 1$. The computer model described here was further developed based on the Seibersdorf Laboratories Model, which is validated against approximately 250 ED_{50} values of non-human primates [Jean and Schulmeister, 2017, 2014b]. The model is only valid for emission durations at $100\,\mu\mathrm{s}$ and higher. Another limitation of the computer model is that the retinal images are considered to be stationary and eye movements are not taken into account. In reality, eye movements cannot be prevented which lead to the retinal image being blurred, thus reducing the hazard potential. As a result, the model provides restrictive results, which is seen as advantageous in the development of the laser safety standard. The safety standard still includes the effect of eye movements. Here, the emission limits are set to a constant value after a certain exposure time. When using the computer model, no times longer than this upper time limit from the standard are considered, which means that eye movements do not have to be simulated.

In this study, the computer model is applied on three different irradiance profiles, namely an elliptical Gaussian, an elliptical top-hat and a rectangular top-hat distribution. In addition to the simulation of thresholds (THRs), an eye safety evaluation is performed where the maximum allowed energy (MAE) is calculated. The ratio between those to values is referred to as reduction factor (RF). As the MAE should be below the THR, the RF has to be larger than one. A MAE value that leads to RFs of about two or higher is considered as sufficiently safe for the thermal damage regime [ICNIRP, 2013b]. The analysed irradiance profiles are assumed to have a wavlength of 530 nm. The human eye shows here the highest sensitivity and the RFs show the lowest values in this region. Furthermore, with the computer model a single pulse is simulated where the emission duration is varied from $100\,\mu\mathrm{s}$ to 50 s. The size of the irradiance distribution on the retina is given by the widths d_x and d_y. The width d_x is set to a value of $83.4\,\mu\mathrm{m}$ and the width d_y is varied from $83.4\,\mu\mathrm{m}$ to $2502\,\mu\mathrm{m}$. A complete overview of the simulation parameters can be seen in Fig. 13. In total around 130 parameter

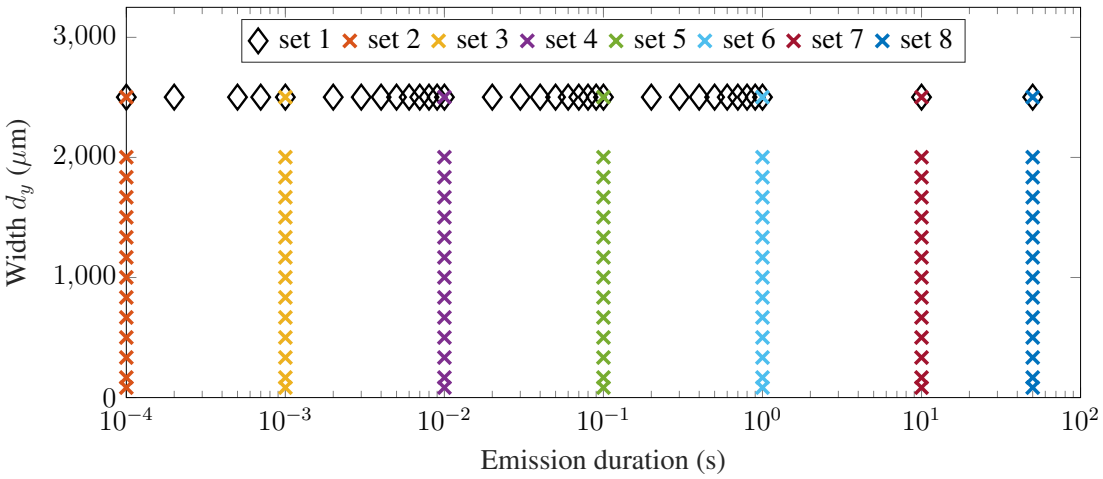

Figure 13: Overview of the parameter sets in this study. In set 1 the emission duration is varied and in the sets from 2 to 8 the width d_y is varied.

variations were investigated where for each variation the computer model was applied to. The heat transfer equation (17) is solved for each of the variation with the finite-element method and in Fig. 14 an exemplary result where the isothermal curves are plotted can be seen. The isothermal curves clearly resemble the corresponding irradiance profiles. Both top-hat distributions show a plateau where the temperature is the same within the irradiated region. In case of the elliptical Gaussian, it is different. Due to a decrease in the irradiance level, the temperature increase is lower at the outer parts of the distribution. Furthermore, there is a better cooling from the surrounding tissue leading to a lower maximum temperature in the center. For this reason, a higher peak irradiance is needed to induce an injury in comparison to the both top-hat profiles. Where in this exemplary case an irradiance of about $6.8\,\mathrm{Wmm^{-2}}$ is needed to induce an injury, the peak irradiance for the Gaussian distribution needs to be $7.1\,\mathrm{Wmm^{-2}}$. This can also be seen in Fig. 15 where the THRs expressed by the irradiance are plotted for a varying emission duration and a varying width d_y. In these plots there is almost no difference between both top-hat results as the temperature rise is similar for both cases. The irradiance levels are higher for the Gaussian distribution in all cases. In order to get a better understanding of the irradiance levels on the retina, two examples are given. In the first example, a green laser pointer with a power of 1 mW and a beam diameter of 1 mm is considered. This is a collimated laser beam where the total radiation power propagates into the eye. It produces a minimal spot on the retina and the irradiance is then approximately $1.3\,\mathrm{mWmm^{-2}}$. In a second example, sun gazing is considered. Under realistic conditions, the pupil is contracted, resulting in a decreased radiant power entering the eye. For the standardized ASTM G173 sun spectrum, the irradiance at the pupil is at about $1000\,\mathrm{Wm^{-2}}$ and the retinal image is a circular spot with a diameter of about 9 mrad or 150 μm in absolute size. [Halbritter et al., 2018]

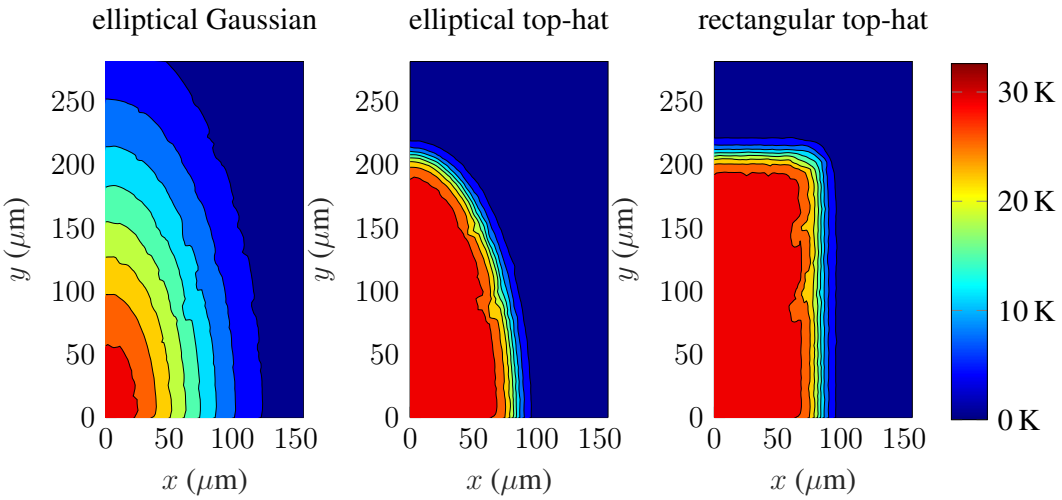

Figure 14: Plot of the isothermal curves in the RPE layer for the three different irradiance profiles. The pulse duration is 1 ms and the widths are $d_x = 166.8\,\mu$m and $d_y = 417\,\mu$m. The isothermal curves show the temperature rise at the end of the pulse and due to symmetry, only the first quadrant is shown.

For pupil diameters between 3 mm and 7 mm, this results in a retinal irradiance of between $0.4\,\mathrm{Wmm}^{-2}$ and $2.2\,\mathrm{Wmm}^{-2}$. In the left plot of Fig. 15, the irradiance decreases for a longer single pulse duration. This means, that for a denaturation that processes over a longer time, a lower irradiance is needed. As a result, the reached maximum temperature also decreases for longer single pulse emission durations. The right plot of Fig. 15 shows a variation of the width d_y where the width d_x is fixed. A higher d_y therefore results in a more elongated profile shape. At a width of about $500\,\mu$m, the THR converges. This can be explained by a heat plateau that is formed in the center region of the retina. Here, the irradiance profile is too large to allow a significant cooling from the surrounding tissue. For a smaller d_y width, there appears a higher deviation between the THR results of both top-hat profiles. This can also be explained by a different thermal behavior where the profile is small enough so that the different cooling behavior affects the determination of the THR. As the elliptical top-hat irradiates a smaller area than the rectangular top-hat, the cooling is better in the center and a higher irradiance is needed to induce an injury.

For all parameter sets, the THR values are simulated and eye safety evaluations are performed using the image analysis from equation (3). For the image analysis, rectangular as well as elliptical field stops were used and both results were used to calculate the RFs. All RFs for the three irradiance profiles and for all parameter sets are plotted in a histogram in Fig. 16. The corresponding statistical data can be seen in Table 5. A total of around 250 RF are obtained for each profile. Generally, the RFs appear to be lower for the Gaussian profile compared to both top-hats. Here, the mean

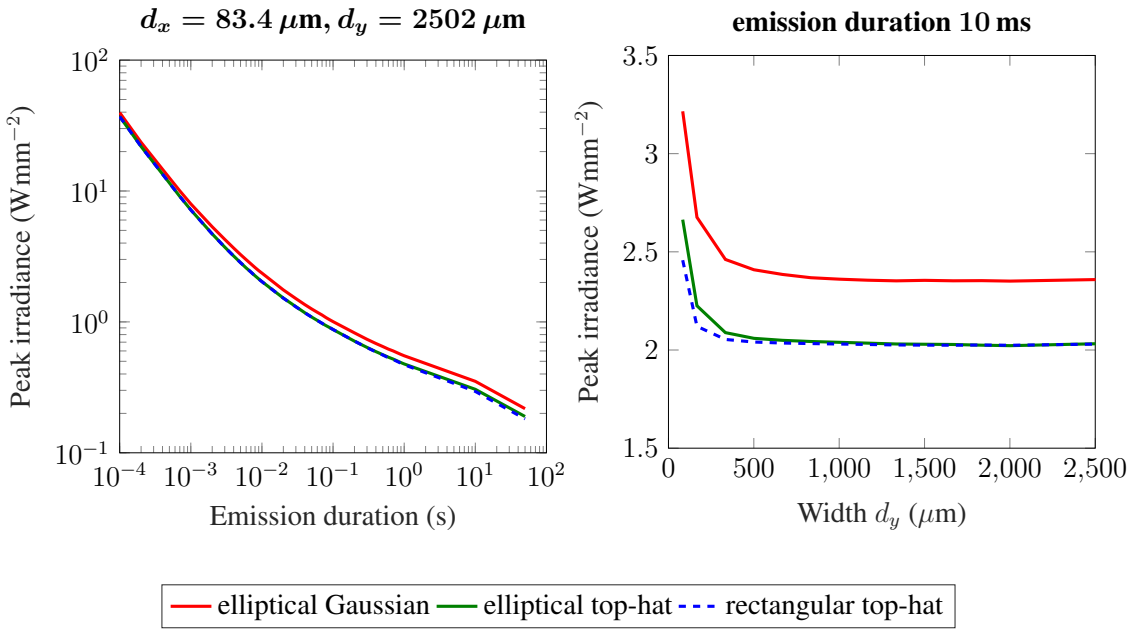

Figure 15: Simulated THRs given in terms of the peak irradiance for the three different irradiance profiles. Left: Results for parameter set 1 from Fig 13. Right: Results for parameter set 4 from Fig 13.

RF is at 3.05 and for the elliptical top-hat it is at 3.48 and for the rectangular top-hat at 3.62. The overall minimum RF is found for the Gaussian profile with a value of 1.52. This minimum and also the minimum values for the top-hat profiles are reached for parameter set 4 where the single pulse duration is 10 ms and the width d_y is equal to d_x with a value of 83.4 μm. In addition, these minimum were obtained using an elliptical shaped field stop. The largest RF appears for the rectangular top-hat with a value of 11.08. This value is present for parameter set 2 where the emission duration is 100μs and d_y=d_x using a rectangular field stop. A more detailed analysis between both field stop shape methods shows, that the use of a rectangular field stop is more restrictive than an elliptical shape leading to higher RF values. The results for the MAE for both field stop shapes show an average deviation of 15.8 %. The minimum RF appears when the width d_y equals d_x and a higher d_y value therefore leads to an increase in the RF. However, it cannot be stated for all cases that a more elongated profile leads to a higher RF. This is shown in Fig. 17. It can be seen, that the RF increases for the single pulse durations 100 μs, 1 ms, 10 ms and 100 ms meaning that a more elongated profile results in a more conservative eye safety evaluation. For the longer single pulse durations, the RF decreases and thus the eye safety evaluation is getting less conservative. However, in these cases the RF is always above two and therefore the evaluation procedure can be considered as sufficiently safe. The results for the elliptical top-hat are not plotted here as the obtained results are similar to the rectangular top-hat.

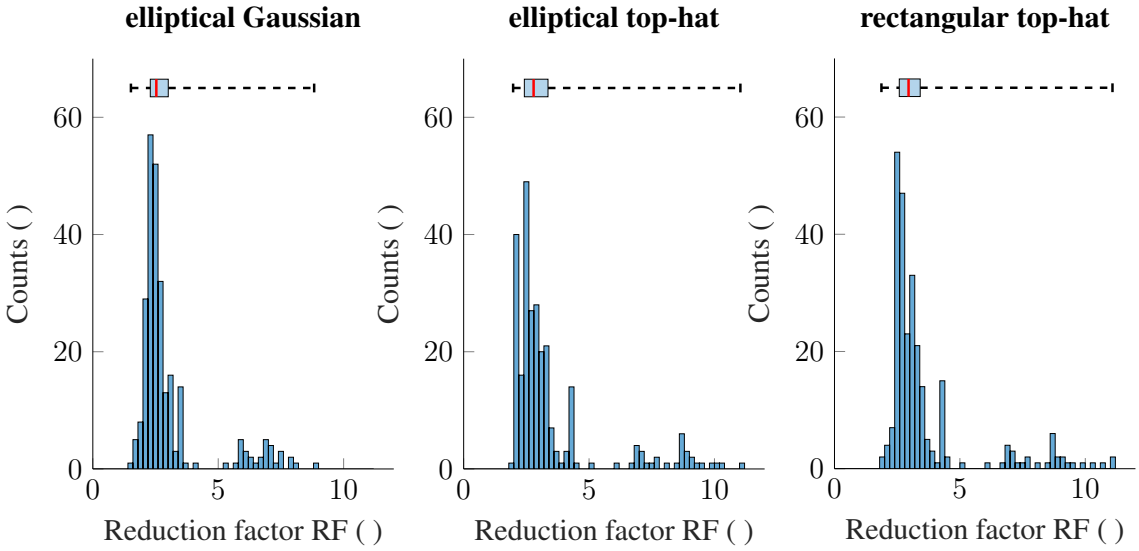

Figure 16: The calculated RFs for the three profiles are plotted as histogram containing all parameter variations from Fig. 13. The box plots above show the minimum and maximum values (dashed line), the first and third quartile (edges of blue rectangle) and the median (red line). The statistics are listed in more detail in Table 5.

In summary, an extensive study was performed in which thermal injuries were simulated for three different irradiance profiles on the retina. Here, the single pulse duration as well as the width of the distribution along one axis were varied. The laser safety standard defines a specific evaluation procedure for profiles that deviate from radial symmetry. By comparison with the simulated values, the question can be answered whether this procedure is valid. First, the calculation of the THR shows that for a Gaussian distribution there are on average about 13.9 % higher threshold values than for the two top-hat distributions. This can be explained by a difference in the thermal behavior, where the Gaussian distribution shows a stronger cooling in the center. Eye safety evaluations were performed with the image analysis using both rectangular and elliptical field stops. It can be seen that using a rectangular field stop is on average about 15.8 % more restrictive than using an elliptical one. Last, the RFs were calculated and the lowest values were found for the Gaussian distribution. The minimum value of 1.52 was present for a radially symmetric distribution with an emission duration of 100 μs. Here, the RF increases for a more elongated profile, meaning that the procedure presented in the standard leads to a more restrictive evaluation. Overall, the procedure from the laser safety standard can be considered as validated for the investigated irradiance profiles.

In future studies, a larger set of different profiles can be investigated with respect to the applicability of the evaluation procedure. The three profiles studied here show

Table 5: Statistical data for the RFs from Fig. 13.

Statistics \ Irradiance Profile	ell. Gaussian	ell. top-hat	rect. top-hat
1st quartile	2.29	2.42	2.58
median	2.53	2.79	2.95
3rd quartile	3.01	3.36	3.42
minimum	1.52	1.97	1.87
maximum	8.83	11.03	11.08
mean	3.05	3.48	3.62
standard deviation	1.46	1.93	1.91

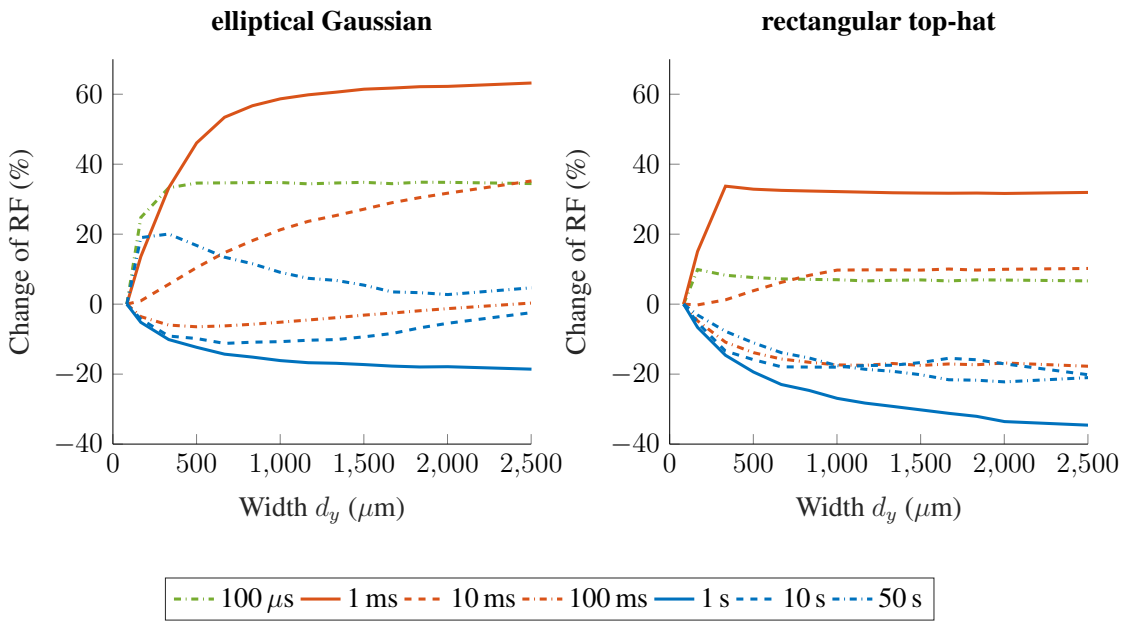

Figure 17: Change of the RF for a varying d_y width from parameter set 2 to 8, see Fig. 13. The eye safety evaluation is performed using a rectangular field stop. Left: Elliptical Gaussian profile. Right: Rectangular top-hat profile.

a single maximum irradiance. It would also be of interest to have profiles that show multiple local maxima, resulting in a more complex temperature behavior. Another important issue concerns the topic of pulsed profiles. According to the laser safety standard, a certain evaluation procedure must also be applied in case of a pulsed retinal image. This procedure is also complex and in the case of non-radially symmetric distributions, there are further open questions which can be dealt with thermal simulations. First, simple pulse patterns, e.g. regular pulses at different pulse repetition frequencies, could be considered and afterwards more complex and irregular pulse pattern can be investigated. Furthermore, the topic of dynamic retinal images, as it is for example the case with scanning lidar systems, still has many open questions, where the computer model presented here can also be used to answer them.

8 References

Adler, F. H. (1965). Physiology of the eye. *Academic Medicine*, 40(7).

ANSI (2014). Z136.1-2014: American National Standard for the Safe Use of Lasers, American National Standards Institute.

Artal, P., Santamaría, J., and Bescós, J. (1988). Retrieval of wave aberration of human eyes from actual point-spread-function data. *J. Opt. Soc. Am. A*, 5(8):1201–1206.

Atchison, D. A. and Smith, G. (2000). *Optics of the Human Eye*. Butterworth-Heinemann.

Beatrice, E. S. and Steinke, C. A. (1972). Q-switched ruby retinal damage in rhesus monkey. In *Report No. R-2051*. Frankford Arsenal, Joint AMRDC-AMC Laser Safety Team, Philadelphia, PA.

Berman, E. R., Schwell, H., and Feeney, L. (1974). The Retinal Pigment Epithelium : Chemical Composition and Structure. *Investigative Ophthalmology & Visual Science*, 13(9):675–687.

Beuth, T., Thiel, D., and Erfurth, M. G. (2018). The hazard of accommodation and scanning lidars. In *Optical Systems Design*.

Bille, J. and Schlegel, W. (2005). *Medizinische Physik 3: Medizinische Laserphysik*. Medizinische Physik. Springer Berlin Heidelberg.

Birngruber, R. (1980). Thermal modeling in biological tissues. In Hillenkamp, F., Pratesi, R., and Sacchi, C. A., editors, *Lasers in Biology and Medicine*, pages 77–97. Springer US, Boston, MA.

Birngruber, R., Drechsel, E., Hillenkamp, F., and Gabel, V.-P. (1979). Minimal spot size on the retina formed by the optical system of the eye. *International Ophthalmology*, 1(3):175–178.

Birngruber, R., Hillenkamp, F., and Gabel, V.-P. (1978). Experimentelle und theoretische Untersuchungen zur thermischen Schädigung des Augenhintergrundes durch Laserstrahlung. *GSF-Bericht, Gesellschaft für Strahlen- und Umweltforschung mbH*.

Birngruber, R., Hillenkamp, F., and Gabel, V.-P. (1985). Theoretical investigations of laser thermal retinal injury. *Health Physics*, 48(6):781–796.

Bodem, F. and Reidenbach, H.-D. (1976). Transformation of Gaussian beams by spherical and cylindrical lenses: the scalar diffraction approach. *Optical and Quantum Electronics*, 8(3):207–211.

Boettner, E. A. (1967). Spectral transmission of the eye.

Boettner, E. A. and Wolter, J. R. (1962). Transmission of the Ocular Media. *Investigative Ophthalmology & Visual Science*, 1(6):776–783.

Brinkmann, R., Hüttmann, G., Rögener, J., Roider, J., Birngruber, R., and Lin, C. P. (2000). Origin of retinal pigment epithelium cell damage by pulsed laser irradiance in the nanosecond to microsecond time regimen. *Lasers in Surgery and Medicine*, 27(5):451 – 464.

Cain, C. P., Noojin, G. D., Hammer, D. X., Thomas, R. J., and Rockwell, B. A. (1997). Artificial eye for in vitro experiments of laser light interaction with aqueous media. *Journal of Biomedical Optics*, 2(1):88–94.

Cain, C. P. and Welch, A. J. (1974). Measured and predicted laser-induced temperature rises in the rabbit fundus. *Invest Ophthalmol*, 13(1):60–70.

Campbell, C. (1987). Fresnel diffraction of Gaussian laser beams by circular apertures. *Optical Engineering*, 26(3):270 – 275.

Campbell, F. W. and Gubisch, R. W. (1966). Optical Quality of the Human Eye. *The Journal of Physiology*, 186(3):558–578.

Delori, F. C., Goger, D. G., and Dorey, C. K. (2001). Age-Related Accumulation and Spatial Distribution of Lipofuscin in RPE of Normal Subjects. *Investigative Ophthalmology & Visual Science*, 42(8):1855–1866.

Delori, F. C. and Pflibsen, K. P. (1989). Spectral reflectance of the human ocular fundus. *Applied Optics*, 28(6):1061–1077.

Dische, Z. (1970). Biochemistry of connective tissue of the vertebrate eye. volume 5 of *International Review of Connective Tissue Research*, pages 209–279. Elsevier.

Duane, T., Tasman, W., and Jaeger, E. (1996). *Duane's clinical ophthalmology. 4.* Duane's Clinical Ophthalmology. Lippincott-Raven.

Fersch, T., Weigel, R., and Koelpin, A. (2017). Challenges in miniaturized automotive long-range lidar system design. In *Commercial + Scientific Sensing and Imaging*.

Finney, D. J. (1971). Probit analysis, 3rd ed. *Journal of Pharmaceutical Sciences*, 60(9):1432–1432.

François, G., Gautron, P., Breton, G., and Bouatouch, K. (2007). Anatomically accurate modeling and rendering of the human eye. In *ACM SIGGRAPH 2007 Sketches*, SIGGRAPH '07, page 59–es, New York, NY, USA. Association for Computing Machinery.

Frederiksen, A., Fiess, R., Stork, W., Bogatscher, S., and Heussner, N. (2012). Eye safety for scanning laser projection systems. *Biomedizinische Technik. Biomedical engineering*, 57:175–84.

Freund, D., McMcally, R., Farrell, R., and Sliney, D. (1996). The theoretical comparison of retinal temperature changes resulting from exposure to rectangular and Gaussian beams. *Lasers in the Life Sciences*, 7(2):71–89.

Freund, D. and Sliney, D. (1999). Dependence of retinal model temperature calculations on beam shape and absorption coefficients. *Lasers in the Life Sciences*, 8(4):229–247.

Galbiati, E. (2001). Evaluation of the apparent source in laser safety. *Journal of Laser Applications*, 13:141–149.

Geeraets, W. J. and Berry, E. R. (1968). Ocular spectral characteristics as related to hazards from lasers and other light sources. *American Journal of Ophthalmology*, 66(1):15–20.

Gerstman, B. S., Thompson, C. R., Jacques, S. L., and Rogers, M. E. (1996). Laser induced bubble formation in the retina. *Lasers in Surgery and Medicine: The Official Journal of the American Society for Laser Medicine and Surgery*, 18(1):10–21.

Goodman, J. (2005). *Introduction to Fourier Optics*. McGraw-Hill physical and quantum electronics series. W. H. Freeman.

Gross, H., Blechinger, F., and Achtner, B. (2008a). *Handbook of Optical Systems, Survey of Optical Instruments*. Handbook of Optical Systems. Wiley.

Gross, H., Blechinger, F., and Achtner, B. (2008b). *Human Eye*, chapter 36, pages 1–87. John Wiley & Sons, Ltd.

Gubisch, R. W. (1967). Optical quality of the human eye. *J. Opt. Soc. Am*, 57:407.

Hadler, J. and Dowell, M. (2013). Accurate, inexpensive testing of laser pointer power for safe operation. *Measurement Science and Technology*, 24(4):045202.

Hahn, G.-A. (2012). *Kurzlehrbuch Augenheilkunde*. Thieme.

Halbritter, W., Kotzur, S., Janssen, H., and Frederiksen, A. (2018). *The Sun - Basis of our lives but not completely harmless?* NIR 218, Fachverband für Strahlenschutz e.V.

Ham, W T, J., Ruffolo, J J, J., Mueller, H. A., Clarke, A. M., and Moon, M. E. (1978). Histologic analysis of photochemical lesions produced in rhesus retina by short-wavelength light. *Investigative Ophthalmology & Visual Science*, 17(10):1029–1035.

Ham, William T., J., Geeraets, W. J., Mueller, H. A., Williams, R. C., Clarke, A. M., and Cleary, S. F. (1970). Retinal Burn Thresholds for the Helium-Neon Laser in the Rhesus Monkey. *Archives of Ophthalmology*, 84(6):797–809.

Henderson, R. and Schulmeister, K. (2003). *Laser Safety*. CRC Press.

Heussner, N., Bogatscher, S., and Stork, W. (2014). Optimizing flying-spot display designs based on the upcoming edition of the laser safety standard. *Journal of the Society for Information Display*, 22(1):9–17.

Hunter, J. J., Morgan, J. I., Merigan, W. H., Sliney, D. H., Sparrow, J. R., and Williams, D. R. (2012). The susceptibility of the retina to photochemical damage from visible light. *Progress in Retinal and Eye Research*, 31(1):28 – 42.

ICNIRP (1999). ICNIRP statement on laser pointers. *Health Physics*, 77(2):218–220, International Commission on Non–Ionizing Radiation Protection.

ICNIRP (2013a). ICNIRP guidelines on limits of exposure to incoherent visible and infrared radiation. *Health Physics*, 105(1):74–96, International Commission on Non–Ionizing Radiation Protection.

ICNIRP (2013b). ICNIRP guidelines on limits of exposure to laser radiation of wavelengths between 180 nm and 1,000 μm. *Health Physics*, 105(3):271–295, International Commission on Non–Ionizing Radiation Protection.

IEC (2006). IEC62471: Photobiological safety of lamps and lamp systems, International Electrotechnical Commission.

IEC (2011). IEC/TR 60825-13 Ed. 2.0: Safety of laser products - Part 13: Measurements for classification of laser products, International Electrotechnical Commission.

IEC (2014). IEC 60825-1 Ed. 3.0: Safety of laser products - Part 1: Equipment classification and requirements, International Electrotechnical Commission.

IEC (2017). IEC 60825-1:2014/ISH1:2017: Safety of laser products - Part 1: Equipment classification and requirements - Interpretation Sheet 1, international electrotechnical commission.

ISO (2005). ISO 11146-1:2005: Lasers and laser-related equipment - Test methods for laser beam widths, divergence angles and beam propagation ratios, International Organization for Standardization.

Ivanov, I. V., Mappes, T., Schaupp, P., Lappe, C., and Wahl, S. (2018). Ultraviolet radiation oxidative stress affects eye health. *Journal of Biophotonics*, 11(7):e201700377.

Jacques, S. L. (2006). Ratio of entropy to enthalpy in thermal transitions in biological tissues. *Journal of Biomedical Optics*, 11(4):1 – 7.

Jäger, C. and Sternecker, M. (2016). Eye safety of IREDs used in lamp applications. (1):1–11.

Jean, M., Kotzur, S., Heussner, N., Schulmeister, K., and Frederiksen, A. (2019). Computer modelling to support laser safety analysis of pulse trains with varying peak power and pulse duration. *International Laser Safety Conference*, 2019(1):202.

Jean, M. and Schulmeister, K. (2014a). Modeling of laser-induced thermal damage to the retina and the cornea. In Ng, E., Acharya, U., Suri, J., and Campilho, A., editors, *Image Analysis and Modeling in Ophthalmology*, chapter 15, pages 265 – 292. CRC Press.

Jean, M. and Schulmeister, K. (2014b). *Modeling of laser-induced thermal damage to the retina and the cornea*, chapter 15, pages 265 – 292. CRC Press.

Jean, M. and Schulmeister, K. (2017). Validation of a computer model to predict laser induced retinal injury thresholds. *Journal of Laser Applications*, 29(3):032004.

Jean, M., Schulmeister, K., Heussner, N., and Frederiksen, A. (2017). Computer modelling to support laser safety analysis of irregular pulse trains. *International Laser Safety Conference*, 2017(1):166–172.

Jean, M., Schulmeister, K., Kotzur, S., and Frederiksen, A. (2020). Validation of a generalized laser safety analysis method for irregular pulse trains. *Journal of Laser Applications*, 32(3):032027.

Judd, D. B., Wyszecki, G., and Wintringham, W. T. (1963). Color in business, science, and industry. *Physics Today*, 16(12):74–75.

Kahle, W., Leonhardt, H., and Platzer, W. (2001). *Taschenatlas Anatomie in 3 Bänden*. Thieme.

Kaschke, M., Donnerhacke, K.-H., and Rill, M. S. (2014). *Optics of the Human Eye*, chapter 2, pages 15–48. John Wiley & Sons, Ltd.

Kaufman, P., Alm, A., and Adler, F. (2003). *Adler's Physiology of the Eye: Clinical Application*. Mosby.

Kelly, M. W. (1997). *Intracellular cavitation as a mechanism of short-pulse laser injury to the retinal pigment epithelium*. PhD thesis, Tufts University.

Kotzur, S. and Frederiksen, A. (2018). Klassifizierung einfach astigmatischer Gaußstrahlen nach IEC 60825-1. *StrahlenschutzPRAXIS*, 3.

Kotzur, S., Frederiksen, A., and Wahl, S. (2019). Consideration of wave optical phenomena for retinal images in laser safety evaluations. *International Laser Safety Conference*, 2019(1):903.

Kotzur, S., Wahl, S., and Frederiksen, A. (2020a). Klassifizierung nach Lasersicherheitsnorm IEC 60825-1:2014 - Alles klar? *StrahlenschutzPRAXIS*, 3.

Kotzur, S., Wahl, S., and Frederiksen, A. (2020b). Retinal image analysis for eye safety evaluations of products emitting optical radiation. In *Optical Interactions with Tissue and Cells XXXI*, volume 11238, pages 16 – 29. International Society for Optics and Photonics, SPIE.

Kotzur, S., Wahl, S., and Frederiksen, A. (2020c). Simulation of laser induced retinal thermal injuries for non-uniform irradiance profiles and their evaluation according to the laser safety standard. In *Tissue Optics and Photonics*, volume 11363, pages 117 – 128. International Society for Optics and Photonics, SPIE.

Kotzur, S., Wahl, S., and Frederiksen, A. (2021a). Simulation of laser-induced retinal thermal injuries for non-uniform irradiance profiles and the applicability of the laser safety standard. *Optical Engineering*, 60(6):1 – 21.

Kotzur, S., Wahl, S., and Frederiksen, A. (2021b). Wave optical simulation of retinal images in laser safety evaluations. *Journal of Biophotonics*, 14(2):e202000339. e202000339 jbio.202000339.R1.

Kuttner, P. (1986). Image Quality Of Optical Systems For Truncated Gaussian Laser Beams. *Optical Engineering*, 25(1):180.

LAMBDA Research Corporation, USA-01460 Massachusetts. Trace Pro.

Lang, G. (2019). *Augenheilkunde*. Thieme.

Lee, C. J., Vroom, J. A., Fishman, H. A., and Bent, S. F. (2006). Determination of human lens capsule permeability and its feasibility as a replacement for bruch's membrane. *Biomaterials*, 27(8):1670–1678.

LeGrand, Y. and ElHage, S. G. (1980). *Physiological Optics*. Springer, Berlin, Heidelberg.

Lepock, J. (2003). Cellular effects of hyperthermia: Relevance to the minimum dose for thermal damage. *International Journal of Hyperthermia*, 19(3):252–266.

LightTrans International UG, D-07745 Jena, Germany. VirtualLab Fusion: Optical Design Software from LightTrans.

Lüllmann-Rauch, R., Asan, E., and KG, G. T. V. (2019). *Taschenlehrbuch Histologie*. Georg Thieme Verlag.

Lund, B. J., Lund, D. J., and Edsall, P. R. (2008). Laser-induced retinal damage threshold measurements with wavefront correction. *Journal of Biomedical Optics*, 13(6):064011.

Lund, D., Stuck, B., and Edsall, P. (2006). Retinal injury thresholds for blue wavelength lasers. *Health Physics*, 90(5):477–84.

Lund, D. J., Edsall, P. R., and Stuck, B. E. (2000). Spectral dependence of retinal thermal injury. In *Laser-Induced Damage in Optical Materials: 1999*, volume 3902, pages 22 – 34. International Society for Optics and Photonics, SPIE.

Lund, D. J., Edsall, P. R., and Stuck, B. E. (2001). Ocular hazards of Q-switched blue wavelength lasers. In *Laser and Noncoherent Light Ocular Effects: Epidemiology, Prevention, and Treatment*, volume 4246, pages 44 – 53. International Society for Optics and Photonics, SPIE.

Lund, D. J., Edsall, P. R., Stuck, B. E., and Schulmeister, K. (2007). Variation of laser-induced retinal injury thresholds with retinal irradiated area: 0.1-s duration, 514-nm exposures. *Journal of Biomedical Optics*, 12(2):024023.

Löfgren, S., Thaung, J., and Lopes, C. (2013). *Laser pointers and eye injuries. An analysis of reported cases.* SSM rapport. Strålsäkerhetsmyndigheten.

Maiman, T. (1960). Stimulated optical radiation in ruby. *Nature*, 187(4736):493–494.

Marshall, J., Hamilton, A. M., and Bird, A. C. (1975). Histopathology of ruby and argon laser lesions in monkey and human retina. A comparative study. *British Journal of Ophthalmology*, 59(11):610–630.

Medeiros, J. A., Borwein, B., and McGowan, J. W. (1979). Application of optical transform techniques to laser irradiation of retina. *Investigative Ophthalmology & Visual Science*, 18(6):602–613.

Ministry of Aviation (1965). *Laser Safety Code of Practice*. London.

Navarro, R. (2009). The optical design of the human eye: a critical review. *Journal of Optometry*, 2(1):3–18.

Neumann, J. and Brinkmann, R. (2005). Boiling nucleation on melanosomes and microbeads transiently heated by nanosecond and microsecond laser pulses. *Journal of Biomedical Optics*, 10(2):024001.

Ng, E., Tan, J., Acharya, U., and Suri, J. (2012). *Human Eye Imaging and Modeling*. CRC Press.

Nickla, D. L. and Wallman, J. (2009). The multifunctional choroid. *Prog Retin Eye Res*, 29(2):144–168.

Niemz, M. (2004). *Laser-Tissue Interactions: Fundamentals and Applications*. Biological and Medical Physics Series. Springer Berlin Heidelberg.

Noell, W. K., Walker, V., Kang, B. S., and Berman, S. (1966a). Retinal damage by light in rats. *Investigative ophthalmology*, 5(5):450–473.

Noell, W. K., Walker, V. S., Kang, B. S., and Berman, S. (1966b). Retinal damage by light in rats. *Investigative Ophthalmology & Visual Science*, 5(5):450–473.

Ooi, E.-H. and Ng, E. Y.-K. (2008). Simulation of aqueous humor hydrodynamics in human eye heat transfer. *Comput. Biol. Med.*, 38(2):252–262.

Oyster, C. W. (1999). The human eye: structure and function. *Nature medicine*, 5 11:1229.

Pedrotti, F., Pedrotti, L., and Pedrotti, L. (2017). *Introduction to Optics*. Cambridge University Press.

Pfefer, T. J., Choi, B., Vargas, G., McNally, K. M., and Welch, A. J. (1999). Pulsed Laser-Induced Thermal Damage in Whole Blood . *Journal of Biomechanical Engineering*, 122(2):196–202.

Piñero, D. P., Ortiz, D., and Alio, J. L. (2010). Ocular scattering. *Optometry and Vision Science : Official Publication of the American Academy of Optometry*, 87(9):E682—96.

Robertson, D. M., McLaren, J. W., Salomão, D. R., and Link, T. P. (2005). Retinopathy from a green laser pointer: a clinicopathologic study. *Archives of Ophthalmology*, 123(5):629–33.

Saleh, B. E. A. and Teich, M. C. (2007). *Fundamentals of photonics*. Wiley, 2nd edition.

Schmetterer, L. and Kiel, J. (2012). *Ocular Blood Flow*. Springer Berlin Heidelberg.

Schuele, G., Rumohr, M., Huettmann, G., and Brinkmann, R. (2005). RPE Damage Thresholds and Mechanisms for Laser Exposure in the Microsecond-to-Millisecond Time Regimen. *Investigative Ophthalmology & Visual Science*, 46(2):714–719.

Schulmeister, K. (2005). The 'Apparent Source' - A Multiple Misnomer. *International Laser Safety Conference*, (1):91–98.

Schulmeister, K. (2013). The radiance of the sun, a 1 mW laser pointer and a phosphor emitter. *International Laser Safety Conference*, 2013(1):371–378.

Schulmeister, K. (2015). Classification of extended source products according to IEC 60825-1. *International Laser Safety Conference*, 2015(1):271–280.

Schulmeister, K. (2019). Notes on the determination of the angular subtense of the apparent source in laser safety. *International Laser Safety Conference*, 2019:284–293.

Schulmeister, K., Gilber, R., Edthofer, F., Seiser, B., and Vees, G. (2006). Comparison of different beam diameter definitions to characterize thermal damage of the eye. In *Laser Beam Control and Applications*, volume 6101, pages 297 – 309. SPIE.

Schulmeister, K., Husinsky, J., Seiser, B., Edthofer, F., Fekete, B., Farmer, L., and Lund, D. (2008). Ex vivo and computer model study on retinal thermal laser-induced damage in the visible wavelength range. *Journal of Biomedical Optics*, 13(5):054038.

Schulmeister, K. and Jean, M. (2017). Inferring injury thresholds for the human retina from medical treatment protocols. *International Laser Safety Conference*, 2017(1):125–131.

Schulmeister, K., Stuck, B., Lund, D., and Sliney, D. (2011). Review of thresholds and recommendations for revised exposure limits for laser and optical radiation for thermally induced retinal injury. *Health Physics*, 100(2):210–20.

Sliney, D. H. (2005). What is the minimal retina image size? - Implications for setting MPE's. *International Laser Safety Conference*, 2005(1):43–47.

Sliney, D. H., Mellerio, J., Gabel, V.-P., and Schulmeister, K. (2002). What is the meaning of threshold in laser injury experiments? Implications for human exposure limits. *Health Physics*, 82(3):335–347.

Sliney, D. H. and Wolbarsht, M. L. (1980). *Safety with Lasers and Other Optical Sources: A Comprehensive Handbook*. Plenum Press.

Smith, G. and Atchison, D. A. (1997). *The Eye and Visual Optical Instruments*. Cambridge University Press.

Strzelecki, W., James, R. H., and Ilev, I. K. (2017). Quantitative Evaluation of a Time-Dependent Eye Hazard Posed by Laser Pointers. *Health Phys*, 113(5):375–381.

Stuck, B. (1984). Ocular susceptibility to laser radiation: human vs Rhesus monkey. volume 1, pages 67–83. Letterman Army Institute of Research.

Subczynski, W., Wisniewska, A., and Widomska, J. (2010). Location of macular xanthophylls in the most vulnerable regions of photoreceptor outer-segment membranes. *Archives of Biochemistry and Biophysics*, 504(1):61–6.

Sudol, R. J. and Friberg, A. T. (1984). Gaussian schell-model beams. In Mandel, L. and Wolf, E., editors, *Coherence and Quantum Optics V*, pages 423–430, Boston, MA. Springer US.

Takata, A. (1977). *Laser-induced Thermal Damage of Skin*. USAF School of Aerospace Medicine, Aerospace Medical Division.

Takata, A., Goldfinch, L., Hinds, J., Kuan, L., and Thomopoulis, N. (1974). *Thermal Model of Laser-Induced Eye Damage*. Engineering Mechanics Division, IIT Research Institute.

Tinsley, J. N., Molodtsov, M. I., Prevedel, R., Wartmann, D., Espigulé-Pons, J., Lauwers, M., and Vaziri, A. (2016). Direct detection of a single photon by humans. *Nature Communications*, 7(1):12172.

Vassiliadis, A. (1971). Ocular damage from laser radiation. In Wolbarsht, M. L., editor, *Laser Applications in Medicine and Biology: Volume 1*, pages 125–162. Springer US, Boston, MA.

Vincelette, R., Thomas, R., Rockwell, B., Clark III, C., and Welch, A. (2009). First-order model of thermal lensing in a virtual eye. *Journal of the Optical Society of America. A, Optics, image science, and vision*, 26:548–58.

Vincelette, R., Thomas, R., Rockwell, B., and Welch, A. (2007). Thermal lensing in the ocular media. *Progress in Biomedical Optics and Imaging - Proceedings of SPIE*, 6435:7.

Vincelette, R. L., Welch, A. J., Thomas, R. J., Rockwell, B. A., and Lund, D. J. (2008). Thermal lensing in ocular media exposed to continuous-wave near-infrared radiation: the 1150–1350-nm region. *Journal of Biomedical Optics*, 13(5):1 – 10.

Vogel, A., Dlugos, C., Nuffer, R., and Birngruber, R. (1991). Optical properties of human sclera, and their consequences for transscleral laser applications. *Lasers in Surgery and Medicine*, 11(4):331–40.

Welch, A. J. and Polhamus, G. D. (1984). Measurement and prediction of thermal injury in the retina of the rhesus monkey. *IEEE Transactions on Biomedical Engineering*, 31(10):633–644.

Wu, J., Seregard, S., and Algvere, P. (2006). Photochemical damage of the retina. *Survey of ophthalmology*, 51:461–81.

Zemax, LLC, Kirkland, USA-98033 Washington. Zemax Optic Studio.

Zinth, W. and Zinth, U. (2013). *Optik: Lichtstrahlen - Wellen - Photonen*. De Gruyter.

Zuclich, J., Lund, D., Edsall, P., Hollins, R., Smith, P., Stuck, B., and Mclin, L. (1999). Experimental study of the variation of laser-induced retinal damage threshold with retinal image size. *Nonlinear Optics*, 21(1):19–28.

Zuclich, J. A., Edsall, P. E., Lund, D. J., Stuck, B. E., Till, S., Hollins, R. C., Kennedy, P. K., and McLin, L. N. (2008). New data on the variation of laser induced retinal-damage threshold with retinal image size. *Journal of Laser Applications*, 20(2):83–88.

Zuclich, J. A., Edsall, P. R., Lund, D. J., Stuck, B. E., Hollins, R. C., Till, S., Smith, P. A., Mclin, L. N., and Kennedy, P. K. (2000). Variation of laser induced retinal-damage threshold with retinal image size. *Journal of Laser Applications*, 12(2):74–80.

9 Acknowledgements

This thesis was done at the Robert Bosch GmbH in cooperation with the ZEISS Vision Science Lab of the Eberhard Karls University of Tübingen. First of all, I would like to thank my advisors Prof. Dr. Siegfried Wahl and Prof. Dr. Frank Schaeffel for their constant support, advice and feedbacks during my time of research and writing this thesis. I would like to thank you very much for the opportunity to do my PhD together with the Zeiss Vision Science Lab.

My special thanks go to my advisor on the part of Robert Bosch GmbH, Dr. Annette Frederiksen, who gave me guidance during my thesis with her expert advice, suggestions and always had time for discussions.

Finally, I would like to express my gratitude to my family who has continuously supported me.

Appendix A: Accepted publications

A1 Wave optical simulation of retinal images in laser safety evaluations

Kotzur, S., Wahl, S., & Frederiksen, A. (2021). Wave optical simulation of retinal images in laser safety evaluations. J. Biophotonics., 14(2), 14:e202000339.
doi:10.1002/jbio.202000339

A1.1 Abstract

Lasers with wavelengths in the visible and near infrared region, pose a potential hazard to vision as the radiation can be focused on the retina. The laser safety standard IEC 60825-1:2014 provides limits and evaluation methods to perform a classification for such systems. An important parameter is the retinal spot size which is described by the angular subtense of the apparent source. In laser safety evaluations, the radiation is often described as a Gaussian beam and the image on the retina is calculated using the wave optical propagation through a thin lens. For coherent radiation, this method can be insufficient as the diffraction effects of the pupil aperture influence the retinal image. In this publication, we analyse these effects and propose a general analytical calculation method for the angular subtense. The proposed formula is validated for collimated and divergent Gaussian beams.

A1.2 Introduction

Laser systems emitting radiation above the accessible emission limits of the laser safety standards [IEC, 2014; ANSI, 2014] or the exposure limits of the ICNIRP guidelines for laser radiation [ICNIRP, 2013b] represent a potential hazard for the human eye and skin.

For laser radiation in the visible and near-infrared wavelength region, defined from 400 nm to 1400 nm according to the laser safety standards, the radiation is imaged on the retina, the most sensitive part of the eye. The eye safety evaluation is based on the retinal image where the angular subtense of the apparent source is determined [Kotzur et al., 2020b]. Thus, a laser classification on a theoretical basis depends on three main issues, the eye model, propagation method and analysis method. An eye model is necessary to simulate the retinal image that is produced by the laser system as the

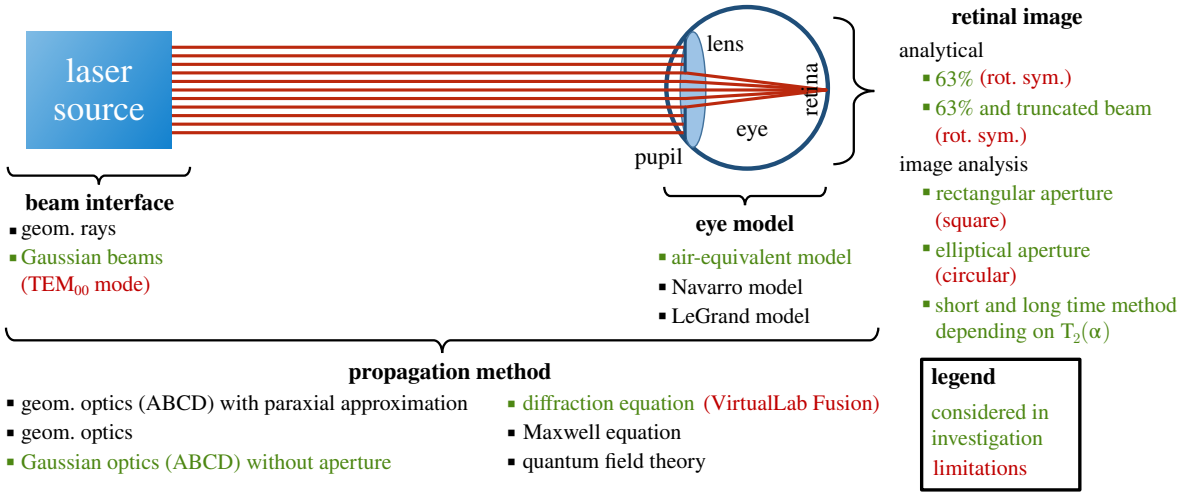

Figure 18: Overview of different eye models, propagation methods and retinal image analyses for laser safety evaluations.

damage takes place at the retina. For calculating the retinal image, an appropriate propagation method has to be applied where relevant aspects of laser propagation are taken into account. At last, the obtained retinal images have to be investigated with an analysis method which is in accordance with the laser safety standard. In Fig. 18, the three main issues are summarized and different possible approaches are shown. The used models and calculation methods for this investigation are marked in colour. The aim of this investigation is illustrated in Fig. 19 where an analytical formula is proposed to perform an eye safety evaluation for Gaussian beams.

Generally, simulations use an air-equivalent eye model which consists of a circular aperture, an ideal lens with a varying focal length and a plane detector. This model emulates a human eye with a refractive index equal to one and a single lens [Henderson and Schulmeister, 2003; Cain et al., 1997] is responsible for the refractive power. It is assumed that the human eye is able to accommodate between 10 cm and infinity. For the simulation of the retinal image, the choice of the appropriate propagation method is currently an open question. Software tools like Zemax Optic Studio [Zemax, LLC] or TracePro [LAMBDA Research Corporation, USA-01460 Massachusetts] use the rules of geometrical optics. However, especially for laser radiation, diffraction effects can occur which impact the eye safety evaluation. Furthermore, the IEC/TR 60825-13 [IEC, 2011] suggests to consider wave optics rather than ray optics to determine the angular subtense of the apparent source. For this reason, we calculate the physically correct retinal images with the software VirtualLab Fusion [LightTrans International UG, D-07745 Jena] solving the diffraction equations numerically. At last, an analysis method has to be applied to the retinal images to obtain the angular subtense of the apparent source which is an important parameter in eye safety evaluations. Here, the laser safety standard provides different approaches where for example the d_{63} diameter of

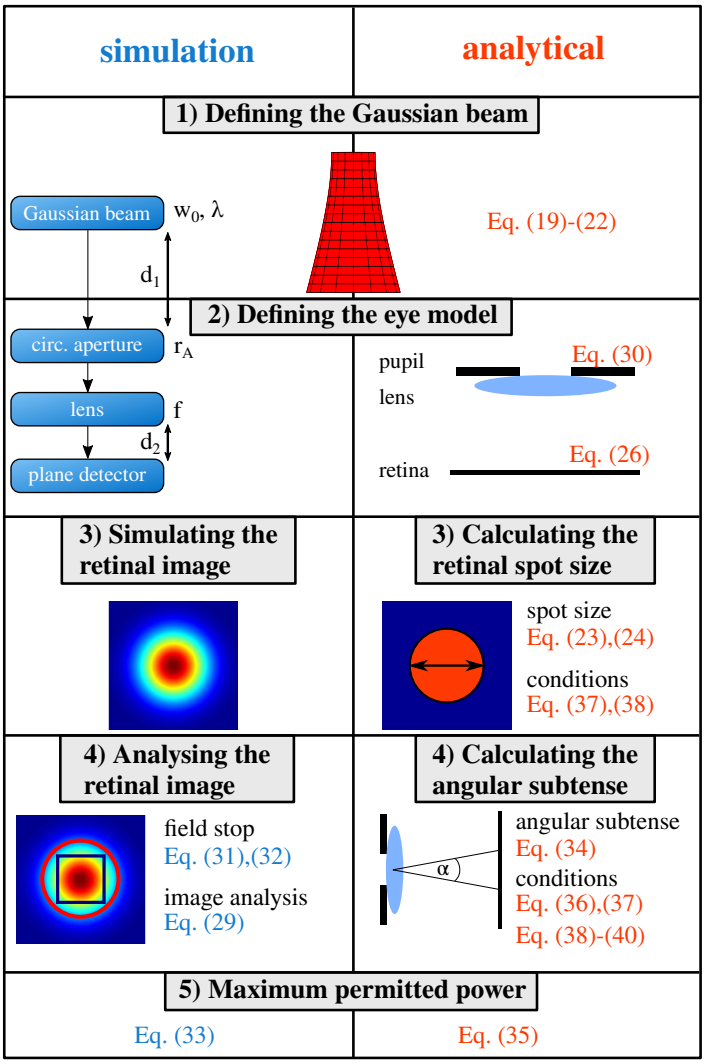

Figure 19: Comparison of the simulation based and analytical approach including a mapping of the essential equations. In the simulation, the propagation of the Gaussian beam is calculated using the diffraction equation and the retinal image is analysed. The analytical procedure proposes several equations replacing the simulations.

a Gaussian beam can be used or where an extensive image analysis is used involving either a rectangular or elliptical shaped measurement aperture [IEC, 2011].

Fig. 19 illustrates the main aspect of this investigation with the aim of providing analytical equations to replace the wave optical simulation of retinal images in laser safety evaluations. As radiation we assume the fundamental mode of a Gaussian beam. In the simulation based approach, the retinal image is simulated with an air-equivalent eye model and by solving the diffraction equations. For these retinal images, an extensive analysis method has to be applied to obtain the angular subtense of the apparent. As all calculation steps require a high computational effort, it would be beneficial to analytically describe the retinal image or to be more precise the angular subtense of the apparent source where the essential wave optical phenomena are included. In

this investigation, a set of analytical equations is proposed and validated against the simulation based evaluation.

A1.3 Gaussian beam propagation through the air-equivalent eye model

The air-equivalent eye model is generally used in theoretical eye safety evaluations as well as experimental setups in laser safety test laboratories. Compared to realistic eye models where the complex point-spread function includes effects such as optical aberrations [Artal et al., 1988], the air-equivalent eye model provides idealized retinal images resulting in conservative eye safety evaluations. Another effect that is neglected in this model is thermal lensing which appears in the near-infrared wavelength region [Vincelette et al., 2007, 2009]. Due to a strong absorption of the vitreous body, local temperature changes lead to the development of a negative lens in case of Gaussian beams. As a result, the retinal spot sizes increase lowering the hazard. Thermal lensing is a relatively unexplored effect and is discussed in more detail with regard to experimental threshold data by Vincelette *et al.* [Vincelette et al., 2008].

In the following, the Gaussian beam propagation will be derived for the air-equivalent eye model. By using the paraxial Helmholtz equation, an analytical description of laser radiation can be derived [Pedrotti et al., 2017]. The Helmholtz equation yields several modes of the beam whereas we focus on the fundamental mode, the TEM_{00} mode. For this mode, the normalized spatial intensity distribution $I(r, z)$ is expressed by

$$I(r,z) = \frac{2}{\pi w(z)^2} \exp\left(-2\frac{r^2}{w(z)^2}\right). \tag{19}$$

Here, it is assumed that the z-axis is the direction of propagation. The distance perpendicular to the z-axis is the radius r. The TEM_{00} mode in equation (19) shows a Gaussian distribution. The width of the distribution is defined by the beam radius $w(z)$ which describes a decrease by a factor of e^2. With this radius, the free space propagation of the Gaussian beam is defined by

$$w(z) = w_0\sqrt{1 + \left(\frac{z - z_0}{z_\mathrm{R}}\right)^2}. \tag{20}$$

The radius w_0 is the beam waist located at z_0. The Rayleigh length z_R can be calculated using

$$z_\mathrm{R} = \frac{\pi}{\lambda} w_0^2. \tag{21}$$

Only two parameters, namely the beam waist w_0 and the wavelength λ, are required

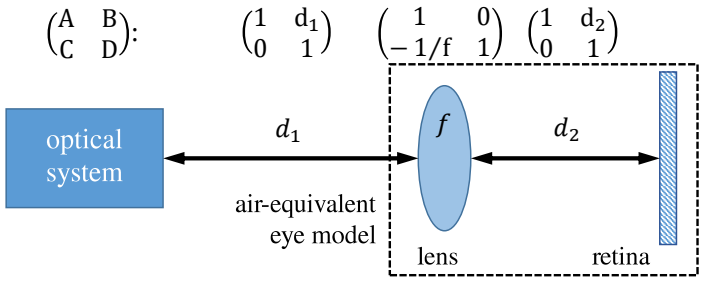

Figure 20: Description of the air-equivalent eye model in paraxial approximation using the ray transfer matrices.

to completely characterize a Gaussian beam. The relation between the waist and the divergence is given by the beam parameter product

$$w_0\theta = \frac{2\lambda}{\pi}. \tag{22}$$

Equation (20) describes the free space propagation of the Gaussian beam according to the Fresnel-Kirchhoff diffraction [Zinth and Zinth, 2013]. For the propagation through an optical system, the ray transfer matrices, also known as ABCD matrices can also be used for the Gaussian beam propagation [Zinth and Zinth, 2013; Bodem and Reidenbach, 1976].

As shown in Fig. 20, three essential matrices describe the propagation through the air-equivalent eye model. One matrix represent the refraction at an ideal lens and the other two are translation matrices.

It is assumed that the eye model is located at a distance d_1 from the waist of the Gaussian beam. According to the laser safety standard, the refractive power of the eye model shall be varied for accommodations between infinity and 10 cm. As the distance d_2 between the lens and the detector is set to 17 mm, the focal length f of the lens varies between 14.52 mm and 17 mm. With the description in Fig. 20, the retinal irradiance distribution is given by a Gaussian distribution with the beam radius w_r

$$w_r = w_0\sqrt{\left(1-\frac{d_2}{f}\right)^2 + \left(\frac{1}{z_\mathrm{R}}\right)^2\left(d_1 + d_2\left(1-\frac{d_1}{f}\right)\right)^2}. \tag{23}$$

The same result is described in a previous investigation by Galbiati in 2001 [Galbiati, 2001]. However, in this description the human pupil which is represented by a circular aperture is excluded. According to the laser safety standard, the circular aperture, also referred to as aperture stop, has a diameter of 7 mm. The applicability of equation (23) is restricted to Gaussian beams much smaller than the pupil aperture. Generally, the propagation through the eye is affected by diffraction at the edges of the aperture.

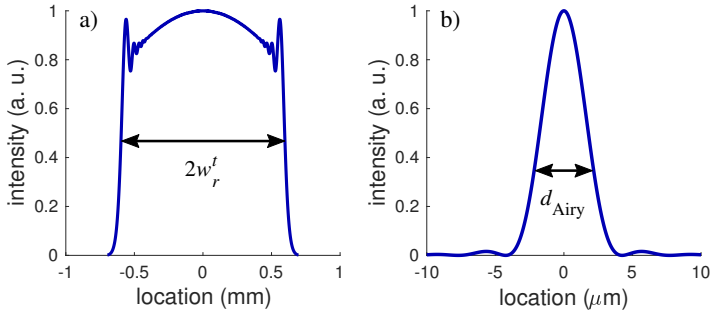

Figure 21: Both plots show the intensity profile for a specific accommodation of the artificial eye for an incident Gaussian beam with $\lambda = 1400\,\text{nm}$ and $w_0 = 10\,\text{mm}$. The left plot a) shows the intensity distribution on the retina for $f = 14.53\,\text{mm}$ (focusing on a distance of 10 cm). In the right plot b), the radiation is focused on the retina with $f = 17\,\text{mm}$ (accommodating to infinity). The propagation was simulated using VirtualLab Fusion [LightTrans International UG, D-07745 Jena].

This results in a truncated Gaussian beam with a cut off of outer parts. In a previous publication [Kotzur and Frederiksen, 2018], a more general formula was proposed to describe the truncated retinal image. The formula is obtained by multiplying a specific factor to equation (23). This factor is calculated by the ratio between the radius r_A of the aperture and the radius of the Gaussian beam at the aperture. The radius w_r^t of the truncated retinal image size is given by

$$w_r^t = r_\text{A} \sqrt{\frac{\left(1-\frac{d_2}{f}\right)^2 + \left(\frac{1}{z_\text{R}}\right)^2 \left(d_1 + d_2\left(1-\frac{d_1}{f}\right)\right)^2}{1+\left(\frac{1}{z_\text{R}}\right)^2 d_1^2}}. \tag{24}$$

This parameter w_r^t does not follow the previous diameter definition like in equation (20) and (23) since it describes the location on the retina where the irradiance is cut off. Equation (23) and (24) describe two physically different propagations for a Gaussian beam entering the eye. Both are examined with regard to their application for eye safety calculations.

A1.4 Wave optical phenomena in the field of eye safety

Several aspects of the human vision like spherical aberrations or astigmatism can be explained using geometrical optics. However, especially for laser radiation the application of wave optics is more precise since two wave optical effects have an impact on the eye safety evaluation. One effect is the characteristic that the radiation cannot be focused on an infinitely small spot and the other effect is the truncation of the Gaussian beam at the pupil aperture. Both phenomena are shown in Fig. 21.

In Fig. 21 the size of the collimated Gaussian beam is larger than the aperture

which leads to interference. In case the radiation is not focused on the retina, which is depicted in the left plot of Fig. 21, the Gaussian beam is truncated and accompanied by oscillations. The calculation according to equation (23) would result in a diameter d_{63} of 2.3 mm whereas the hazard potential is underestimated compared to the real imaged radiation, which shows a smaller extent. With equation (24) the diameter is approximated to 1.2 mm. Since this formula assumes a beam profile in which no oscillations occur, the question arises whether this approximation is sufficiently precise for eye safety calculations.

The other effect which is depicted in the right plot of Fig. 21, represents the diffraction limit d_{Airy} caused by the circular aperture of the pupil. The characteristic intensity pattern consists of a circular main lobe maximum, referred to as 'Airy disc', and several concentric sidelobes with decreased peak intensities. This intensity distribution is described by the far field approximation of the diffraction equation, the Fraunhofer diffraction, whereas the far field image corresponds to the imaged radiation in the focal plane of the ideal lens. The calculation of the distribution in the right plot of Fig. 21 is based on the Fourier transform of the circular aperture whereby the intensity peaks are given by the Bessel function of the first kind [Zinth and Zinth, 2013]. The width of the main lobe maximum can be estimated by

$$d_{\mathrm{Airy}} \approx 1.22 \frac{\lambda}{2 r_{\mathrm{A}}} d_2. \tag{25}$$

According to this equation, the width of the 'Airy disc' is calculated to approximately 4.1 μm for the beam parameters in Fig. 21. This limit cannot be obtained with the propagation formula for a Gaussian beam in equation (23) because the diameter of the imaged Gaussian beam decreases continuously for increasing incident beam widths.

The laser safety standards [IEC, 2014; ANSI, 2014] also include a minimum spot size. It is stated that laser sources which produce retinal spots smaller than the minimum spot size are referred to as point sources. The ICNIRP guidelines [ICNIRP, 2013b] explain the imaging behavior of point sources due to the eye resolution [Gross et al., 2008a]. The smallest spot is set to an angular subtense of 1.5 mrad which corresponds to an absolute size of 25.5 μm [Sliney and Wolbarsht, 1980]. The deviation from the theoretical expectation according to equation (25) of about one order of magnitude is due to the assumption of an idealized eye model. However, the question of the minimum spot size for the human eye is rather complex and currently there is no definite answer. Experimental measurements on rhesus monkeys show that there are marginal dependencies of the injury thresholds on spot sizes smaller than 5 mrad [Lund et al., 2007; Zuclich et al., 2008]. In these measurements the spot size of 5 mrad could be interpreted as minimum spot size. The retinas of rhesus monkeys represent a suit-

able model to derive exposure limits as they are more sensitive compared to human retinas [Marshall et al., 1975; Stuck, 1984; Schulmeister and Jean, 2017]. However, a possibly smaller spot size cannot be excluded for human retinas. For this reason, the thresholds of the above mentioned measurements are used for the exposure limits for point sources whereby a safety margin of 10 was applied [Schulmeister et al., 2011]. In addition, there are studies, which show that it is possible to produce smaller spot sizes on the retina. Experimental measurements with rabbit eyes done by Birngruber *et al.* in 1979 [Birngruber et al., 1979] demonstrate that an advantageous beam position leads to a minimum spot size of 7 μm representing the diffraction limit. However, due to scattering there is an intensity loss of about fifty percent. It was found that also for the human eye a diffraction limited focus can be achieved [Campbell and Gubisch, 1966; Gubisch, 1967]. In another study which was done by Lund *et al.* in 2008 [Lund et al., 2008] measurements on non-human primates were performed by using wavefront-corrected beams to reduce refractive errors and aberrations. Though the results show lower thresholds than without using wavefront correction the retinal spot size could not be determined. More detailed examinations regarding the minimum spot size in the fields of laser safety can be found in further literature [Sliney, 2005; Jean and Schulmeister, 2017, 2014b].

In consequence of the uncertainties regarding the accurate determination of the minimum spot size, the description of point sources from the laser safety standards [IEC, 2014; ANSI, 2014] is used in this investigation. The size of the analysed intensity patterns is set to a minimum value of 25.5 μm in case the actual sizes have a lower value. The other effect, the truncation of the beam, is not mentioned in the current laser safety standards. The propagation of a Gaussian beam through a circular aperture is numerically studied in previous works [Kuttner, 1986; Campbell, 1987]. In this investigation we propose an analytical formula for the width of a truncated Gaussian beam which can directly be used for the determination of the angular subtense of the apparent source. We simulate the retinal images with the air-equivalent eye model using the software VirtualLab Fusion [LightTrans International UG, D-07745 Jena] and compare them to the analytical descriptions according to equation (23) and (24) in terms of eye safety. Furthermore, two wavelengths 400 nm and 1400 nm will be investigated as they define the borders of the wavelength range which is imaged on the retina according to the laser safety standards.

A1.5 Laser safety evaluation of retinal images

An eye safety evaluation for retinal images can be performed in two different ways, namely assuming a point source or an extended source. By assuming a point source, the whole radiation is considered to be contained within the minimum spot size. In

case the retinal image shows an irradiance distribution that is much larger than the minimum spot size this approach is over restrictive. According to the laser safety standards, the accessible emission limits increase for larger spots of extended sources. The spot size is expressed by the angular subtense of the apparent source. However, an extensive calculation method has to be applied to the retinal image to obtain the angular subtense [Schulmeister, 2005, 2015; Kotzur et al., 2020b]. The size of an arbitrary retinal image could be characterised by different beam diameter definitions like the second moment diameter or the FWHM criterion used for different applications. In terms of the eye safety, such diameter definitions are not suitable to determine the angular subtense [Schulmeister et al., 2006]. The tophat and the Gaussian profile are the only exceptions. For a tophat profile, the angular subtense is equal to the extent of the profile. In case of a Gaussian profile, the laser safety standards state that the d_{63} diameter can be used for a conservative evaluation. It should be emphasized that this method can only be used if the laser beam creates a Gaussian irradiance profile on the retina.

A1.5.1 Image analysis for extended sources

For the classification of an extended source, the angular subtense α is needed. This size is obtained by analysing the retinal image. The general procedure is to determine the most restrictive size for the angle of acceptance γ, which defines a field stop used to calculate the 'accessible emission' (AE). This worst case is found by varying γ to maximize the ratio between AE and the 'accessible emission limit' (AEL). This procedure is referred to as image analysis and is illustrated in Fig. 22 for a Gaussian intensity distribution where the variation of the angle of acceptance γ and the angular subtense α of the apparent source are shown. It is stated in the laser safety standards [IEC, 2014; ANSI, 2014], that the field stop can either be placed in front of a detector or close to the apparent source. In our simulation-based method the field stop is on the retinal image. There are two possible shapes of the field stop defined, namely an elliptical and a rectangular shape [IEC, 2011].

The AE and the AEL depend on the angular subtense α. By assuming a laser source with the total radiation power P_0, the AE can be given with

$$\mathrm{AE}\,(\alpha) = P_0\,\eta_{\mathrm{pupil}}\,\eta_{\mathrm{retina}}\,(\alpha)\,. \tag{26}$$

The factor η_{pupil} is the extraocular factor and gives the power percentage of P_0 that passes the pupil and enters the eye. The factor $\eta_{\mathrm{retina}}\,(\alpha)$ is the intraocular factor and is calculated by dividing the radiation energy contained within the field stop by the total energy of the retinal image. For an unknown angular subtense, the field stop is

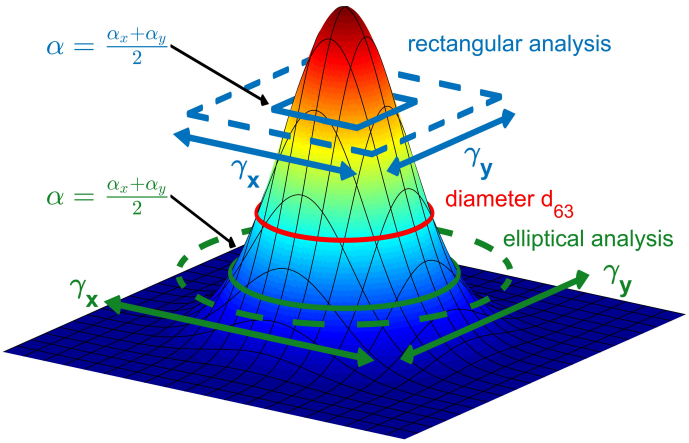

Figure 22: Illustration of the image analysis for a Gaussian distribution with the diameter d_{63} (solid red line) using elliptical shaped (green) and rectangular shaped (blue) field stops. By varying the angle of acceptance γ_x and γ_y (dashed lines) the angular subtense α (solid lines) is determined.

defined by the angle of acceptance γ_x and γ_y representing both orthogonal directions. By performing the image analysis, both γ_x and γ_y are varied within the limitations defined in the laser safety standards. In addition, the location of the field stop in the retinal image has to be varied for a complete analysis. It should also be noted that the field stops have to be rotated from 0° to 90°. However, rotating the field stops is not necessary in this investigation as the analysed retinal images are rotationally symmetric.

The AEL increases with the angular subtense α and the laser safety standard defines two different functional behaviors. Depending on the emission duration t, the α dependencies are given by the piecewise function

$$\kappa\left(\alpha\right) = \begin{cases} \alpha, & \text{if } t \leq T_2\left(\alpha\right) \\ \alpha\, 10^{-\frac{\alpha}{394\,\mathrm{mrad}}}, & \text{if } t > T_2\left(\alpha\right) \end{cases} \tag{27}$$

with the time $T_2\left(\alpha\right)$ defined in the laser safety standard IEC 60825-1:2014 [IEC, 2014]

$$T_2\left(\alpha\right) = 10 \times 10^{[(\alpha-\alpha_{\mathrm{min}})/98.5\,\mathrm{mrad}]}\,\mathrm{s}. \tag{28}$$

In the following, the image analysis for $t \leq T_2\left(\alpha\right)$ is referred to as 'short-time method' and for the other case the term 'long-time method' is used. As the time T_2 depends on the angular subtense, the value is determined during the image analysis. Here, for times greater than 10 s both the short and long-time have to be applied whereas the most restrictive result is used.

The angular subtense α of the apparent source is not directly a characteristic of

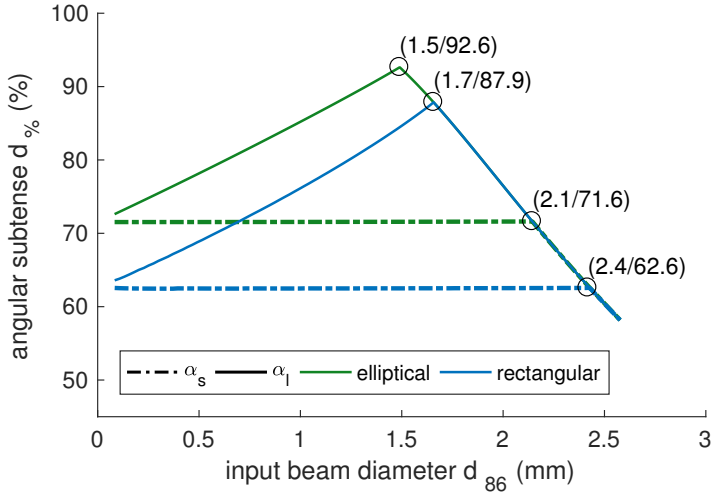

Figure 23: The results of the image analysis for a symmetric Gaussian intensity distributions differ for the short- and long-time method (α_s and α_l) as well as for the choice of the field stop (elliptical and rectangular). The x-axis shows different extents of the Gaussian distribution defined by the d_{86}-diameter and the y-axis shows the determined angular subtense expressed as $d_{\%}$-diameter. The markers show all kinks in the curves.

the source of the radiation. But it is derived from the retinal images the laser source produces. The image analysis is defined with

$$\left\{ \gamma \left| \max \frac{\eta_\mathrm{retina}\left(\gamma\right)}{\kappa\left(\gamma\right)} \right\} \right|_{\gamma=\alpha} \tag{29}$$

in case of radially symmetric retinal images where γ_x equals γ_y and is illustrated in Fig. 22. The calculation for the angular subtense can differ depending on the evaluation time according to equation (27). Fig. 23 illustrates the behavior for a Gaussian retinal image with varying widths.

The kinks of all curves arise from the limitation of the angular subtense to 100 mrad. While both angular subtenses stay approximately constant for the short-time method an increasing curve can be seen for the long-time method. For the symmetric Gaussian intensity distribution, the choice of a rectangular field stop leads to a smaller angular subtense than for an elliptical field stop.

As the TEM_{00} mode of the Gaussian beam is investigated, see equation (19), the retinal images are radially symmetric. Thus, the retinal intensity distributions expressed in polar coordinates is $I_\mathrm{RI}(r)$. The extraocular factor η_pupil is given with

$$\eta_\mathrm{pupil} = 1 - \exp\left(-2 \frac{r_\mathrm{A}^2}{w_0^2} \left(1 + \frac{d_\mathrm{l}^2}{z_\mathrm{R}^2} \right)^{-1} \right). \tag{30}$$

The intraocular factor η_retina depends on the shape and size of the field stops. Due to

radial symmetry, the center of the field stops coincide with the center of the intensity pattern and the shape is circular or square. Therefore, the factor is given by

$$\eta_{\text{retina}}^{\text{S}}(\alpha) = \frac{8}{P_{\text{RI}}} \int_0^{\frac{\pi}{4}} \int_0^{\sqrt{1+\tan^2\varphi}\, d_2 \tan\frac{\alpha}{2}} I_{\text{RI}}(r) r \,\mathrm{d}r \,\mathrm{d}\varphi \tag{31}$$

in case of a square field stop and

$$\eta_{\text{retina}}^{\text{C}}(\alpha) = \frac{2\pi}{P_{\text{RI}}} \int_0^{d_2 \tan\frac{\alpha}{2}} I_{\text{RI}}(r) r \,\mathrm{d}r \tag{32}$$

in case of a circular field stop. The radiation power P_{RI} describes the total power within the retinal image and is equal to P_0 times the extraocular factor. The upper limit of the surface integral in equation (31) and equation (32) depends on the angular subtense or in case of the image analysis on the angle of acceptance. This shows that each retinal image leads to a different behavior of AE.

All results are expressed by the maximum allowed power P_0. This power is calculated by equating AE and AEL. For emission durations greater than T_2 the emission limit from IEC 60825-1:2014 [IEC, 2014] is used to calculate a wavelength-independent power with

$$\frac{P_0}{C_4 C_7} = \frac{7 \times 10^{-4} \frac{\alpha}{\alpha_{\min}} \left(\frac{T_2(\alpha)}{1\,\text{s}}\right)^{-\frac{1}{4}}}{\eta_{\text{pupil}}\, \eta_{\text{retina}}(\alpha)}\,\text{W}. \tag{33}$$

The wavelength of the radiation does not appear on the right side of equation (33) and determines both correction factors C_4 and C_7. For wavelengths smaller than 700 nm, both factors are not defined according to the laser safety standard and they are set to one.

A1.5.2 Proposed extended simplified method for Gaussian beams

For Gaussian beams, there is a procedure described in the laser safety standards [IEC, 2014; ANSI, 2014] to determine the angular subtense. The d_{63} diameter can be used to calculate the angular subtense with the requirement that the total radiation power entering the eye is assumed to be contained in α. With this requirement, the described method is more restrictive than the image analysis. However, as this method is only applicable to Gaussian intensity distribution on the retina, it is not suitable in case of a beam truncation. We propose a piecewise defined function to extend this method given by

$$\alpha = \begin{cases} 2\arctan\frac{w_r}{\sqrt{2}d_2}, & \frac{w_0}{\sqrt{2}}\sqrt{1+\frac{d_1^2}{z_{\text{R}}^2}} < r_{\text{A}} \\ 2\arctan\frac{w_r^t}{d_2}, & \frac{w_0}{\sqrt{2}}\sqrt{1+\frac{d_1^2}{z_{\text{R}}^2}} \geq r_{\text{A}} \end{cases} \tag{34}$$

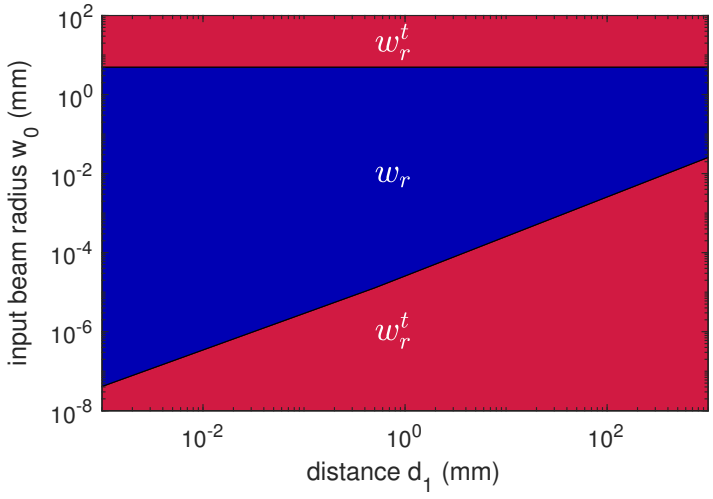

Figure 24: Region plot using the conditions from equation (34) to illustrate which case of the piecewise function applies for a specific distance d_1 and beam radius w_0. The plot is for a wavelength of 400 nm. Other wavelengths up to 1400 nm show a similar upper horizontal boundary line of w_r. The lower diagonally rising boundary line of w_r shifts up to a factor of three for the w_0 values.

where both conditions on the right side ensure a continuous transition of the functions. The regions showing which function from equation (34) has to be used are illustrated in Fig. 24 for different distances d_1 and input beam radii w_0. Analogous to equation (33), the wavelength-independent maximum allowed power is determined with

$$\frac{P_0}{C_4 C_7} = \frac{7 \times 10^{-4} \frac{\alpha}{\alpha_{\min}} \left(\frac{T_2(\alpha)}{1\,\mathrm{s}} \right)^{-\frac{1}{4}}}{\eta_{\mathrm{pupil}}} \,\mathrm{W}. \tag{35}$$

The intraocular factor η_{retina} is set to one. This proposed extended method will be compared with the results from the image analysis to verify its applicability.

A1.6 Results

In this section collimated and divergent Gaussian beams with the wavelengths 400 nm and 1400 nm are investigated with regard to eye safety. Here, the beam parameters as well as the parameters of the eye model are varied to simulate retinal images which are analysed with the image analysis and compared to the proposed analytical formula.

A1.6.1 Collimated Gaussian beams

In the following, collimated Gaussian beam showing divergences smaller than 0.5 mrad are investigated. As the distance d_1 is a negligible factor for the simulated retinal images it is set to zero. Therefore, the minimum beam waist w_0, the wavelength λ and

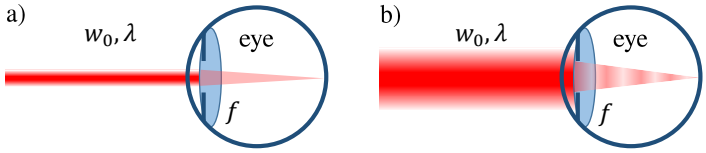

Figure 25: The figure shows the free parameters to create all possible retinal images in case of collimated beams. The left image a) shows a configuration where the Gaussian beam is smaller than the eye pupil and in the right image b) the beam size exceeds the pupil which leads to non-negligible diffraction effects.

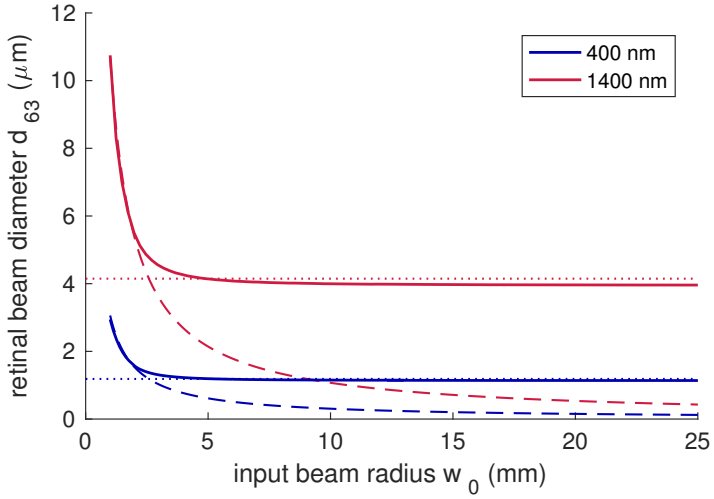

Figure 26: The plot shows the retinal image size expressed as the d_{63} diameter for different input beam waists. The solid lines show the wave optical simulation. The dashed lines correspond to equation (23) and the dotted lines to the estimation of the diffraction limit using equation (25).

the focal length f of the eye model are the essential parameters to define all possible configurations. The free parameters and the eye model are shown in Fig. 25.

As it was previously shown in Fig. 21, there are two major diffraction effects. The diffraction limit occurs when focusing the radiation on the focal plane (f=d_2=17 mm). The size of the simulated retinal image in dependence of the input beam waist as well as the theoretical expectations as defined in equation (23) and (25) are shown for the two essential wavelengths in Fig. 26.

For a sufficiently small beam radius w_0, estimated to be smaller than 1.9 mm, the Gaussian beam propagation from equation (23) where the circular aperture is excluded can be used for a correct calculation. However, for an increasing beam waist the diffraction at the aperture influences the image and the deviation increases. For larger input beam waists, the calculation for the diameter d_{63} is primarily based on the main lobe maximum and can be approximated by the diffraction limit from equation (25). These retinal images show spots smaller than the minimum spot size and are classified as point sources according to the laser safety standards.

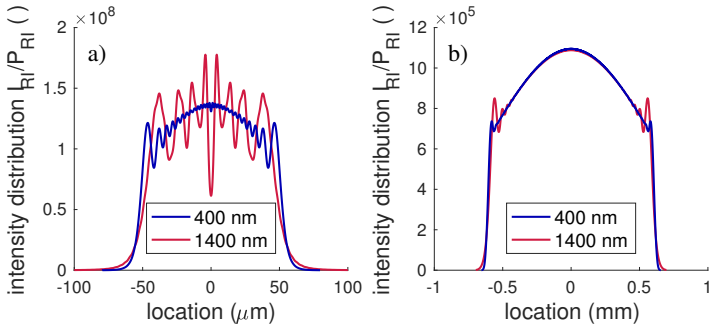

Figure 27: Retinal images for a Gaussian beam with an input beam waist of 7 mm and for 400 nm and 1400 nm where the normalized intensity distribution along a symmetry is plotted. The focal length of the eye model is set to 16.7 mm in plot a) and 14.5 mm in plot b). The simulation was performed with VirtualLab Fusion [LightTrans International UG, D-07745 Jena].

For focal lengths smaller than 17 mm the beam truncation occurs. This can be seen in Fig. 27 where the retinal images show oscillations. The frequency and amplitudes of the oscillations differ significantly for both wavelengths. A wavelength of 1400 nm generally leads to lower frequencies and higher amplitudes compared to the wavelength of 400 nm. The angular subtense α is calculated with equation (29) using a circular and square field stop. All results obtained by varying the focal length of the eye are shown in Fig. 28 together with the analytical calculation from equation (34).

The calculation using w_r in equation (23) yields much larger α values leading to an underestimation of the eye hazard. Here, the w_r^t calculation from equation (24) shows more accurate results. Furthermore, depending on the shape of the field stop, the image analysis gives slightly different angular subtenses. The circular field stop according to equation (32) leads to larger α values than the square field stop from equation (31). The figure depicts only the results for 400 nm as both wavelengths were found to be identical in case of the theoretical calculation which can be seen in Table 6. Regarding the image analysis, the differences are less than 1 %.

The results for a Gaussian beam with a varying beam waist at a fixed focal length of 14.53 mm can be seen in Fig. 29. As a result of the truncation effect there is a maximum retinal image size. For beam waists above approximately 5 mm the angular subtense show a saturation value. For the circular field stop, a kink occurs and the saturation value is at about 72 mrad. The image analysis using the square field stop has a lower maximum value which is at 66 mrad. The analytical calculation for the truncated radius w_r^t from equation (24) fits the image analysis results. The maximum α value describes a retinal image with a spot size of 1.2 mm. For beam waists smaller than 4 mm, equation (23) which describes the radius w_r is more suitable to calculate the angular subtense. With the angular subtense α and the intraocular factor, the wavelength-independent maximum allowed power can be calculated according to equation (33)

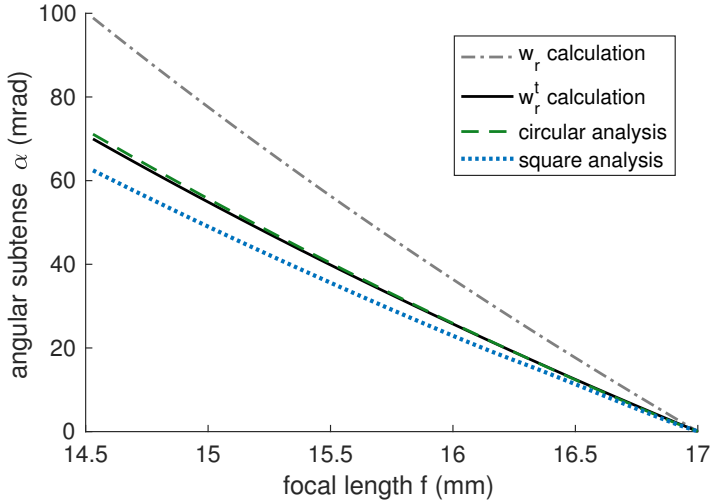

Figure 28: The angular subtense α for a Gaussian beam with a beam waist of 7 mm and a wavelength of 400 nm where the focal length of the eye is varied. The angular subtense is calculated using the analytical approach (w_r and w_r^t calculation) and using the image analysis (circular and square field stop).

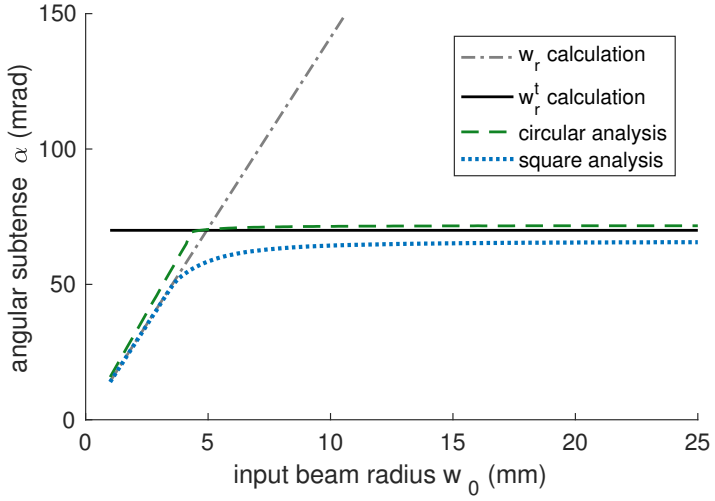

Figure 29: Calculation of the angular subtense for a Gaussian beam with a wavelength of 400 nm where the beam waist is varied. The eye model is defined for a focal length of 14.53 mm.

and equation (35). The obtained radiation power is shown in Fig. 30.

For larger beam waists, the w_r calculation method gives an allowed power more than ten times higher than with the image analysis. At about 7 mm, there is a discontinuity due to the limitation of the angular subtense to 100 mrad. The w_r^t calculation fits the results of the image analysis for large beam radii where the effect of truncation appears. Table 6 lists the maximum allowed power for specific beam waists regarding a wavelength of 400 nm and 1400 nm.

In general, it can be stated that the differences for both wavelengths 400 nm and 1400 nm are negligibly small. This means that the oscillations in the retinal images

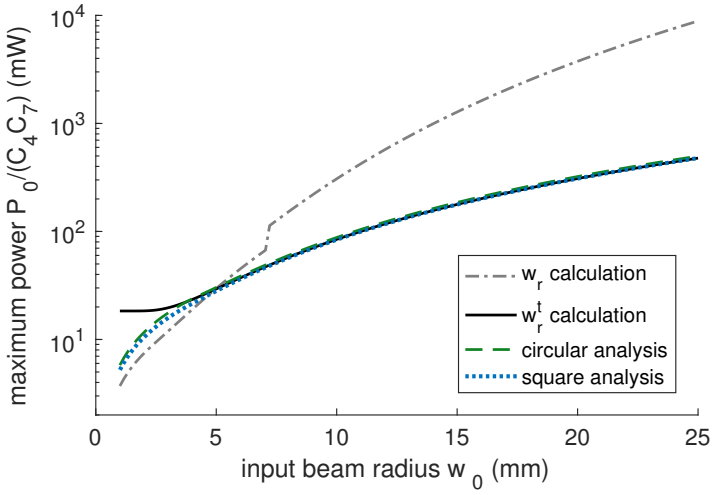

Figure 30: Determination of the maximum allowed power for the beam parameters from Fig. 29.

shown in Fig. 27 have no decisive influence on the evaluation. Regarding both image analysis methods, the maximum allowed power is higher for a circular field stop than for a rectangular field stop. The difference between both methods decreases with increasing beam radius from 10 % to about 4 %.

In case of small beam waists where no truncation occurs, the w_r calculation from equation (35) is more restrictive than both image analysis methods. In this beam radius region, the w_r^t calculation method leads to incorrect results. The piecewise function defined in equation (34) contains both above mentioned calculation methods with corresponding conditions to define their scope. The conditions are derived from the intersection between equation (23) and (24). The application of the piecewise function is more restrictive than the image analysis using circular field stops. For a collimated Gaussian beam, the piecewise function can be extended. A further condition checks if a classification according to an extended source has to be performed which is given by

$$f \leq \frac{d_2}{1 + \frac{\sqrt{2}\,25.5\,\mu\mathrm{m}}{w_0}}. \tag{36}$$

In a second condition a boundary for the minimum beam radius is set to

$$w_0^{\mathrm{B}} = \sqrt{r_{\mathrm{A}}^2 + \sqrt{r_{\mathrm{A}}^4 - \frac{\lambda^2}{\pi^2} d_1^2}}. \tag{37}$$

In case the minimum beam waist w_0 is smaller than w_0^{B} the upper case of equation (34) applies and in the opposite case truncation occurs and the lower equation is used. The boundary w_0^{B} is equal to the upper boundary line from Fig. 24.

Table 6: Calculation of the maximum allowed power for different approaches to perform eye safety evaluations.

beam radius w_0	maximum allowed power $P_0/(C_4C_7)$ for 400 nm (mW) 1400 nm (mW)			
	theoretical calculation		image analysis	
	w_r	w_r^t	square	circular
1 mm	3.71	18.36	5.23	5.79
	3.71	18.67	5.28	5.76
2 mm	7.58	18.40	10.65	11.83
	7.59	18.42	10.67	11.80
3 mm	12.31	19.83	16.24	18.05
	12.31	19.84	16.26	18.03
5 mm	29.31	29.18	27.89	30.09
	29.30	29.18	27.90	29.95
7 mm	66.97	47.09	46.29	48.89
	66.96	47.09	46.32	48.93
10 mm	304.90	84.15	83.58	87.61
	304.84	84.15	83.55	88.82
25 mm	8875	477.50	477.60	498.20
	8875	477.50	476.60	500.50

A1.6.2 Divergent Gaussian beams

In comparison to collimated Gaussian beams, investigating divergent beams is more extensive as an additional degree of freedom, the distance d_1, has to be taken into account. Generally, a divergent Gaussian beam is obtained for a beam waist in the micrometer regime and is expressed by the full divergence angle which is calculated according to equation (22). Fig. 31 shows the free parameters varied in this investigation.

At first, the focal length f is varied for a divergent beam illustrated in the right configuration of Fig. 31. Here, the distance d_1 is 0.3 m and the Gaussian beam has a divergence angle of 50.9 mrad. This divergence is obtained for a beam waist of $w_0 = 5\,\mu$m in case of a wavelength of 400 nm and for $w_0 = 17.5\,\mu$m in case of 1400 nm. By accommodating to the beam waist, the minimal spot size is achieved. Accommodation to other distances result in larger retinal images with truncation. Fig. 32 shows the truncation for two examples. Both curves show a sudden decrease in the intensity distribution. Varying the focal length leads to different retinal image sizes. By applying all calculation methods, the corresponding angular subtenses are shown in Fig. 33. It was found that the curves for both wavelengths slightly differ from each other in case of the image analysis. In case of the theoretical calculations the results for both

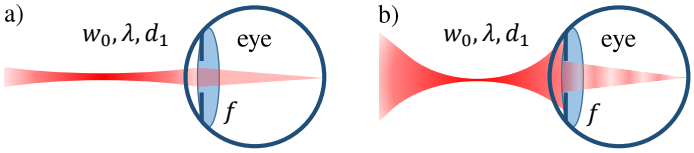

Figure 31: The figure shows the free parameters to produce all possible retinal images. In the left image a) the beam has a low divergence leading to a small beam size at the pupil. In the right image b) the high divergence leads to diffraction effects at the pupil.

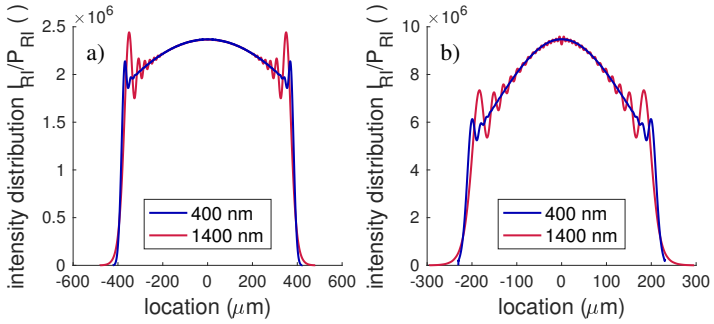

Figure 32: Retinal images for accommodating to 10 cm a) and to infinity b). The intensity distributions for a wavelength of 400 nm and 1400 nm are shown. The results were obtained with VirtualLab Fusion [LightTrans International UG, D-07745 Jena].

wavelengths were identical. For this reason, only the curve for the wavelength 400 nm is plotted.

The angular subtense minimizes for a focal length of about 16.1 mm which corresponds to an accommodation to the beam waist. Using the w_r diameter from equation (23) incorrectly results in a too large angular subtense. The w_r^t calculation from equation (24) fits the image analysis results. With equation (33) and (35) the maximum allowed power is calculated which is shown in Fig. 34. For focal lengths around 16 mm, the maximum power is at 1.15 mW. This value is reached for all calculation methods due to the minimum spot size limitation from the laser safety standard. Table 7 lists the maximum allowed power for specific focal lengths and for both wavelengths of 400 nm and 1400 nm.

Though the differences for both wavelengths are generally larger than compared to the investigation done for collimated beams, the differences are still negligibly small. Therefore in case of divergent Gaussian beams, the effect of the oscillations can also be neglected. Furthermore, the analysis with circular field stops gives about 4-6 % higher allowed powers than the analysis with square field stops. The w_r^t calculation turns out to be more restrictive in case of focal lengths from 16 mm to 17 mm than both image analysis methods. For other focal lengths, the results are slightly higher.

For the proposed extended simplified method from equation (34), further conditions

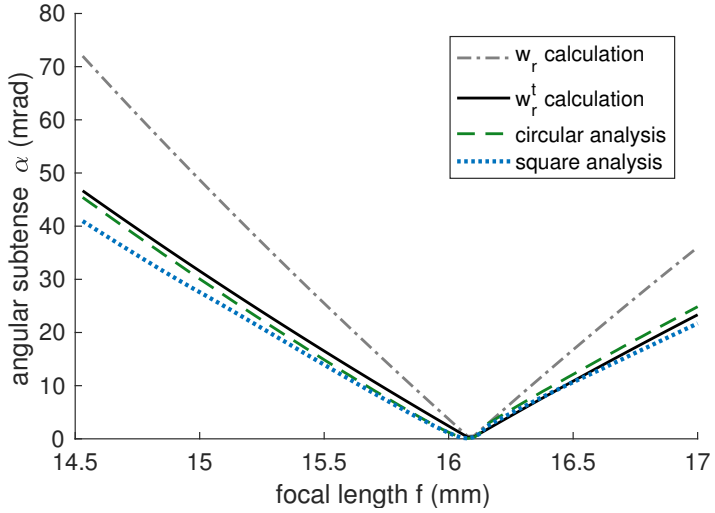

Figure 33: Determination of the angular subtense for a divergent Gaussian beam with a wavelength of 400 nm and a divergence angle of 50.9 mrad. The distance d_1 is 0.3 m.

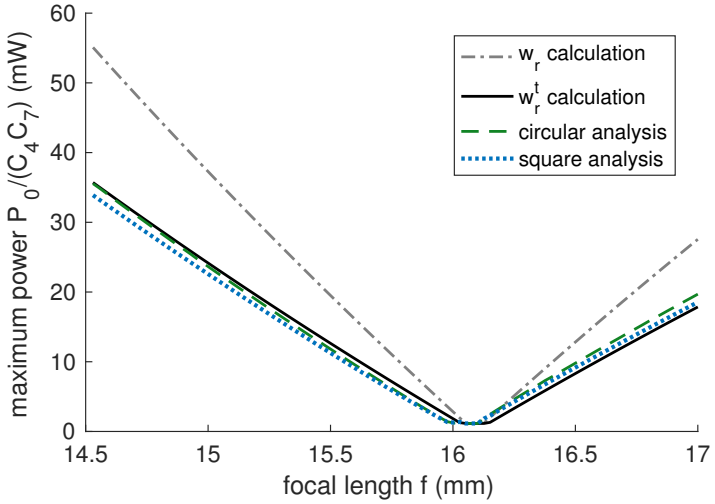

Figure 34: Determination of the maximum allowed power for the investigation from Fig. 32.

can be given. The first conditions are the inequalities

$$f \leq \left[\frac{d_1}{d_1^2 + z_\mathrm{R}^2} + \frac{1}{d_2} - \frac{z_\mathrm{R}}{d_2 \left(d_1^2 + z_\mathrm{R}^2\right)} \times \sqrt{\frac{\left(25.5\,\mu\mathrm{m}\right)^2}{2w_0^2} \left(d_1^2 + z_\mathrm{R}^2\right) - d_2^2} \right]^{-1} \tag{38}$$

and

$$f \geq \left[\frac{d_1}{d_1^2 + z_\mathrm{R}^2} + \frac{1}{d_2} + \frac{z_\mathrm{R}}{d_2 \left(d_1^2 + z_\mathrm{R}^2\right)} \times \sqrt{\frac{\left(25.5\,\mu\mathrm{m}\right)^2}{2w_0^2} \left(d_1^2 + z_\mathrm{R}^2\right) - d_2^2} \right]^{-1} . \tag{39}$$

For focal lengths that meet the conditions, the retinal image is larger than the min-

Table 7: Calculation of the maximum allowed power for specific focal lengths regarding the investigated beam from Fig. 34 for both wavelengths 400 nm and 1400 nm.

focal length f	maximum allowed power $P_0/(C_4C_7)$ for 400 nm (mW) 1400 nm (mW)			
	theoretical calculation		image analysis	
	w_r	w_r^t	square	circular
14.53 mm	55.08	35.70	33.89	35.54
	55.09	35.70	33.76	35.70
15.00 mm	37.13	24.06	22.49	23.55
	37.13	24.06	22.34	23.73
15.50 mm	19.40	12.57	11.19	11.75
	19.40	12.57	11.15	11.93
16.08 mm	1.15	1.15	1.15	1.15
	1.15	1.15	1.15	1.15
16.50 mm	12.85	8.33	9.19	9.82
	12.85	8.33	9.07	9.81
17.00 mm	27.56	17.86	18.54	19.69
	27.56	17.86	18.42	19.79

imum spot size and a classification according to an extended source can be performed. Furthermore, a boundary beam waist can be defined with

$$w_0^{\mathrm{B}} = \sqrt{r_{\mathrm{A}}^2 - \sqrt{r_{\mathrm{A}}^4 - \frac{\lambda^2}{\pi^2} d_1^2}}. \tag{40}$$

For beams waists smaller than w_0^{B} the lower case of equation (34) applies and for beam waists larger than w_0^{B} the upper case is used. The boundary w_0^{B} is equal to the lower boundary line from Fig. 24.

The validity of these conditions is demonstrated in Fig. 35 where the beam waist is varied in its size as well as in its position. Due to the variation of the distance d_1, the boundary condition from equation (40) for the correct calculation of the beam radius changes. For smaller distances the effect of the truncation occurs for a smaller beam radius. In addition, for 400 nm the truncation appears for smaller beam waists than for 1400 nm as the divergence angle appears to be generally higher for larger wavelengths. The theoretical calculation gives generally smaller angular subtenses than the image analysis. As the factor η_{retina} is set to one in the theoretical calculation, the results for the maximum allowed power are more restrictive than using the image analysis.

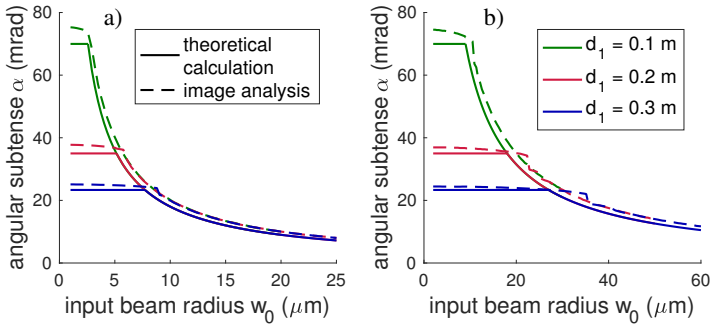

Figure 35: The angular subtense α is shown for the theoretical calculation based on equation (34) and for the image analysis where the circular field stop was used. The parameters d_1 and w_0 of the divergent Gaussian beam are varied and the focal length is 17 mm. The left plot a) shows the result for a wavelength of 400 nm and the right plot b) for a wavelength of 1400 nm.

A1.7 Summary and Conclusion

A simulative approach to perform laser safety evaluations for radiation in the visible and near-infrared region is used to determine the angular subtense of the apparent source. The diffraction equations for radiation entering an air-equivalent eye model are solved to calculate the retinal image. An image analysis according to the laser safety standards is used to the retinal images to obtain the angular subtense.

This procedure is applied to the Gaussian beam and compared with analytical equations from the laser safety standard where the d_{63} diameter is used to determine the angular subtense. For a coherent beam, it was found that the analytical calculation according to the standards can lead to significantly larger angular subtenses when truncation occurs due to the diffraction at the pupil. This results in an underestimation of the hazard as larger retinal spot sizes would be assumed.

We propose a new analytical formula to correctly calculate the angular subtense for possible configurations of collimated and divergent Gaussian beams. This proposed extended method was compared to the correct results from the simulative approach. It was found that our proposed analytical approach is sufficiently precise and can be applied to Gaussian beams in the visible and near-infrared wavelength region. The major advantage of this method is that the angular subtense α can be directly calculated where there is no need to extensively simulate and analyse the retinal image.

In conclusion, it can be stated that the wave optical propagation is essential for a simulation-based classification of a laser system. The use of common Gaussian beam propagation equations can lead to wrong results and an underestimation of the hazard. For the fundamental mode of the Gaussian beam, an alternative calculation method was proposed and validated.

A1.8 Outlook

In a future study, the investigation can be expanded to elliptical or simple astigmatic coherent Gaussian beams where there are more free parameters. According to the laser safety standards, the angular subtense is calculated by averaging the size along both orthogonal directions. Here, the proposed formula can be applied to each direction to obtain the angular subtense. A comparison with the results of an image analysis could verify the applicability for these beams.

An important aspect of this study is that the investigated Gaussian beams are coherent. In reality, laser radiation deviates from ideal Gaussian beams which is described by the M^2 factor [ISO, 2005]. Partial coherent beams can be described with the Gaussian Schell-modell beams [Sudol and Friberg, 1984]. Here, the diffraction behaves different and the truncation effect is reduced [Schulmeister, 2019]. In a further investigation, this model can be used to derive a more general formula to perform eye safety evaluations for Gaussian beams with an M^2 factor larger than one.

Conflict of Interest

The authors declare that there are no conflicts of interest related to this article.

Data Availability Statement

The data that support the findings of this study are available from the corresponding author upon reasonable request.

A2 Simulation of laser-induced retinal thermal injuries for non-uniform irradiance profiles and the applicability of the laser safety standard.

Kotzur, S., Wahl, S., & Frederiksen, A. (2021). Simulation of laser-induced retinal thermal injuries for non-uniform irradiance profiles and the applicability of the laser safety standard. Opt. Eng., 60(6), 0066115. doi:10.1117/1.OE.60.6.066115

A2.1 Abstract

Significance: A validated biophysical computer model simulating retinal thermal damage thresholds is used to investigate elongated retinal images. The ICNIRP guideline [ICNIRP, 2013b] and the laser safety standard IEC 60825-1:2014 [IEC, 2014] include a method for averaging non-uniform extended sources, however, there are no studies that have examined the applicability in detail. This study represents a method that can also support future research in the field of eye safety.

Aim: As there is currently no experimental data available for non-uniform irradiance profiles, the calculation procedure given in the laser safety standard is derived from symmetric retinal images. In our study, we aim to verify this calculation procedure for such profiles on the retina in the thermal hazard regime.

Approach: A three dimensional computer model which solves the heat transfer equation and the Arrhenius equation describing the denaturation of the proteins in the retina, is used to simulate the threshold values for the retinal thermal injury. In this study, three different non-uniform irradiance profiles, elliptical Gaussian, elliptical top-hat and rectangular top-hat distributions, are investigated for a wavelength of 530 nm. The profiles are varied in their sizes and simulated for different single pulse durations. By applying the laser safety standard, the maximum allowed energies are calculated and divided by the corresponding threshold values to obtain the reduction factor (RF) which is a crucial parameter in our study.

Results: Due to the thermal behavior in the retinal tissues, the Gaussian irradiance profiles yield larger threshold values than both top-hat profiles. Furthermore, the ratio between the threshold values and the maximum allowed energies are found to be the lowest for the Gaussian profiles.

Conclusion: The simulated retinal thermal injury thresholds for the three investigated non-uniform irradiance profiles show larger reduction factors than the minimum reduction factor found for symmetric profiles. This supports the applicability of the evaluation scheme of the laser safety standard for non-uniform retinal images.

A2.2 Introduction

Lasers with wavelengths in the visible and near-infrared region represent a potential hazard for the retina. Unlike other eye injuries, *e.g.* photokeratitis, retinal injuries are irreversible and impair the vision or lead to a permanent vision loss. Due to the focusing ability of the eye the radiation can be imaged on a small spot on the retina which increases the irradiance by a factor up to 10^5. The retinal injuries can be caused by photomechanical, thermomechanical, thermal or photochemical damage mechanisms. It depends on the wavelength, the emission duration and the peak power which of the listed mechanism dominates.

The definition of emission limits is needed for the development of safe laser products. These emission limits are derived predominately from experimental threshold values measured in the non-human primate (NHP) [Sliney et al., 2002; Marshall et al., 1975; Stuck, 1984; Schulmeister and Jean, 2017]. The International Commission on Non-Ionizing Radiation Protection (ICNIRP) reviews the experimental data and publishes guidelines with exposure limits. Based on the ICNIRP Guidelines [ICNIRP, 2013b], the International Electrotechnical Commission (IEC) develops a laser safety standard (current edition IEC 60825-1:2014 [IEC, 2014]) providing emission limits and calculation instruction for the evaluation and classification of laser systems. The emission limits depend on the wavelength, the emission duration and, regarding retinal limits, on the imaged spot size expressed by the angular subtense of the apparent source [Lund et al., 2007; Zuclich et al., 2008; Schulmeister et al., 2008].

All threshold experiments with NHPs are done with circular laser profiles with a Gaussian or a top-hat shape. For the eye safety analysis of arbitrary non-uniform retinal irradiance distributions, the laser safety standard and the ICNIRP guidelines instruct to measure the amount of the retinal radiant energy which is contained in a field stop and to compare it to the limit. This field stop has to be varied in its size, position and orientation to obtain the most restrictive result [Kotzur et al., 2020b]. It is stated that the averaged field stop size and therefore the averaged retinal image size is used for the calculation of the emission limit without giving a rationale. There are few studies that have specifically addressed this issue. The applicability of this calculation method is mainly supported by studies done by Freund *et al.* [Freund et al., 1996; Freund and Sliney, 1999]. Here, however, only the temperature course in the retina was simulated and no damage simulation was performed. An example of a laser product leading to a non-uniform retinal image is a line laser with a collimated and a divergent axis. A classification according to the laser safety standard IEC 60825-1 is based on the averaged size. Fig. 36 illustrates non-uniform rectangular and elliptical retinal images and their corresponding averaged size. Since there is no explicit definition of the shape

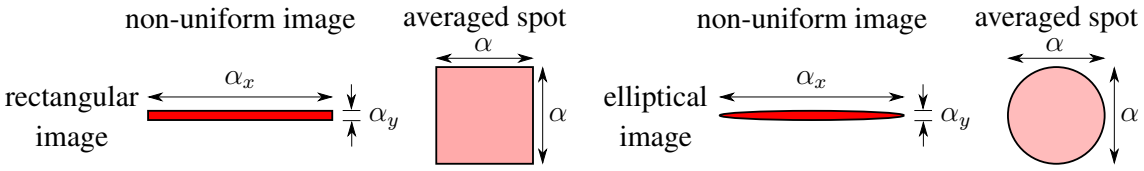

Figure 36: Illustration of non-uniform retinal images with the extents α_x and α_y and their average spot size according to the laser safety standard. In laser classifications, the averaged spots are assumed to contain the same radiant power as the non-uniform spot. In this example, both the extents α_x and α_y are each smaller than the maximum limitation $\alpha_{\max}$ defined in the laser safety standard.

of the field stop [IEC, 2011], a rectangular and an elliptical field stop are depicted. As both the non-uniform retinal image and the averaged spot are assumed to contain the same radiant power, the irradiance of the averaged spot is generally lower.

In this publication, the question if the procedure of the averaged spot size for non-uniform retinal profiles is suitable will be answered. The damage thresholds for such retinal images for which there are currently no experimental data available are simulated by means of a computer model and compared with the evaluation schemes and emission limits of the laser safety standard IEC 60825-1:2014. For the simulation of the threshold limits, we focus on the retinal thermal damage regime and use a computer model based on the work of Jean and Schulmeister [Jean and Schulmeister, 2017, 2014b].

A2.3 Theory of the Retinal Thermal Damage Mechanism

The retinal thermal injury mechanism is dominant for emission durations in the microsecond and second regime. It is a denaturation of the proteins within the retina and can be described as a thermal burn. As a consequence, necrosis of the cells occurs leading to vision loss in the concerned regions. If the retina is exposed to laser radiation, the radiant energy will be absorbed by the retinal pigment epithelium (RPE) [Ham et al., 1970; Beatrice and Steinke, 1972] leading to an increased temperature in the RPE.

The damage mechanism can be described analytically. As the reaction speed is independent of the temperature [Birngruber, 1980] the process can be given by a rate equation [Birngruber et al., 1985]

$$\frac{\mathrm{d}c\,(t)}{\mathrm{d}t} = -k\,(T\,(t))\,c\,(t)\,. \tag{41}$$

The value $c\,(t)$ is the concentration of not denatured molecules. The function k is the

temperature-dependent reaction rate

$$k\left(T\left(t\right)\right) = A \exp\left(-\frac{E}{RT(t)}\right). \tag{42}$$

Here, R is the ideal gas constant. A is a rate factor and E is the inactivation energy. Both values can be measured experimentally [Jacques, 2006]. With the rate equation (41) the Arrhenius equation can be derived to represent the denaturation [Jacques, 2006; Pfefer et al., 1999]

$$\Omega\left(t\right) = \ln\frac{c\left(0\right)}{c\left(t\right)} = A\int_0^t \exp\left(-\frac{E}{RT(t')}\right) \mathrm{d}t'. \tag{43}$$

The temperature dependence of A is negligibly small compared to the exponential function in the integrand and is assumed to be constant [Birngruber et al., 1985]. The value Ω represents the percentage of denatured molecules with the relation

$$c_{\mathrm{denatured}}\left(t\right) = 1 - \exp\left(-\Omega\left(t\right)\right). \tag{44}$$

In general, a thermal injury occurs for $\Omega > 1$. The computer model used in this investigation is based on the definition of a damage threshold where Ω equals one. This corresponds to a degree of denaturation of 63%. In another study it was suggested that 5% is sufficient to induce cell death [Lepock, 2003]. However, the frequency factor A was different which changes the meaning of the value Ω.

Equation (43) shows that the criterion for the denaturation process is not based on a temperature limit but rather on the temporal temperature profile. For this reason, the thermal damage is strongly coupled to the shape of the retinal image and the emission duration.

A2.4 Description of the Computer Model to Simulate Retinal Thermal Thresholds

In this section, the computer model used to predict the threshold values for non-uniform irradiance profiles is presented. These thresholds are defined as the ED_{50} values representing the 50 % probability of inducing retinal injuries. The principal procedure to build a retinal thermal injury model is to determine the retinal image with an eye model and derive a heat source within the retinal layers. Then, the heat transfer equation is numerically solved and the temporal temperature behavior is inserted into the Arrhenius equation (43) [Takata et al., 1974; Takata, 1977; Welch and Polhamus, 1984]. The procedure is illustrated in Fig. 37.

The used computer model is a further development of the Seibersdorf Laboratories

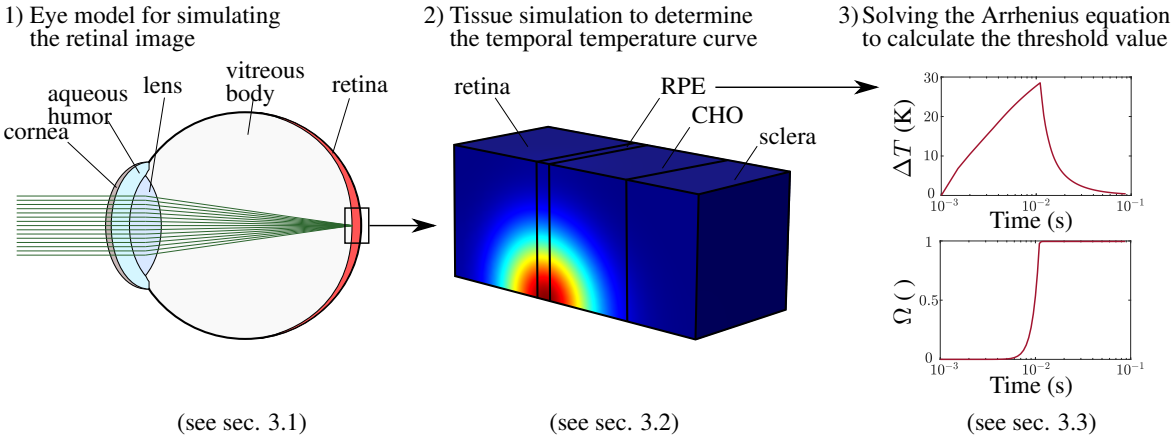

Figure 37: Procedure to simulate a retinal thermal injury threshold value. In the first step the retinal image is determined with an eye model. In the second step, the heat source within the tissue is defined and the heat transfer equation is numerically solved. In the last step, the threshold value is calculated with the Arrhenius equation Ω, for which the temperature increase ΔT is used.

Model (SLM). The SLM was build by Jean and Schulmeister who validated the model against 31 studies with 253 experimental ED_{50} values of NHPs [Jean and Schulmeister, 2017, 2014b]. As the retina of NHPs is more sensitive than the retina of humans, the thresholds for humans are higher [Marshall et al., 1975; Stuck, 1984; Schulmeister and Jean, 2017]. Based on the SLM, we developed a three dimensional model to investigate non-uniform retinal images. The model predicts the ED_{50} threshold value in terms of the total intraocular energy of the retinal irradiance profile. This refers to the amount of radiant energy to induce a minimal visible lesion (MVL) with a probability of 50 % [Sliney et al., 2002]. The computer model is valid for pulse durations longer than 100 μs and is therefore only applicable to retinal thermal injuries. In case of shorter pulse duration there is an increasing probability of inducing a retinal injury in the thermomechanical damage mechanism regime where microbubbles and shockwaves can be formed [Brinkmann et al., 2000; Gerstman et al., 1996; Kelly, 1997].

A2.4.1 Optical Properties of the Eye

The retinal image size is calculated with the LeGrand model for the relaxed human eye [LeGrand and ElHage, 1980]. The eye model consists of four layers, namely the cornea, the aqueous, the lens and the vitreous body, see Fig. 37. The sizes of these layers are scaled with a factor of 0.8 to approximate the eye properties of the NHP [Ham et al., 1970; Medeiros et al., 1979]. In the following, the laser beam is treated as a Gaussian beam and the size given by the divergence. The retinal image size is calculated using the elements of the ray transfer matrix representing the optical system [Zinth and Zinth, 2013]. As laser radiation cannot be focussed on an infinitely small spot, there

is a minimum spot size for the retinal image. The measurements with non-human primates show that the threshold values converge to a constant energy for laser sources smaller than 5 mrad [Zuclich et al., 1999, 2000; Lund et al., 2007; Zuclich et al., 2008]. This is set as the minimum spot size for NHPs in the computer model. The propagation of the laser radiation through the eye is accompanied by absorption at the layers of the eye model and by intraocular scattering [Birngruber et al., 1979; Piñero et al., 2010]. The amount of radiant energy that is not scattered out of the defined retinal image depends on the wavelength and on the beam size. It is distinguished between the total transmittance τ_{Total} and the direct transmittance τ_{Direct} [Boettner and Wolter, 1962]. The total transmittance refers to the whole radiant energy that is transmitted through the medium where the direct transmittance is measured within a narrow angle along the direction of propagation. Therefore, for small retinal images the direct transmittance and for relatively large retinal images the total transmittance is used.

It is suggested by Jean and Schulmeister [Jean and Schulmeister, 2017] to use an equation that ensures a continuous transition from small to large retinal spot sizes. The effective transmittance is given by

$$\tau_{\mathrm{eff}}\left(\lambda, r_{\mathrm{Spot}}\right) = \tau_{\mathrm{Total}}\left(1 - g\left(\lambda\right) h\left(r_{\mathrm{Spot}}\right)\right) \tag{45}$$

with

$$g\left(\lambda\right) = \frac{1}{2} \exp\left(-\frac{\lambda}{883\,\mathrm{nm}}\right) \tag{46}$$

and

$$h\left(r\right) = \exp\left(-\frac{2r}{600\,\mu\mathrm{m}}\right). \tag{47}$$

These functions were obtained by validating against ED_{50} data. Furthermore, the function $h\left(r\right)$ represents the suggestion by Boettner [Boettner and Wolter, 1962] where most of the radiant energy is within a cone of 3 deg and where about 35% is scattered out of an 1-deg cone. The effective transmittance from equation (45) describes the case of a circular spot on the retina. In the case of non-uniform retinal profiles, this equation cannot directly be applied, but is used as a basis to derive another function. This topic will be discussed in more detail later.

The radiation that propagates to the retina is absorbed by macular pigments, melanin and hemoglobin. The macular pigments are located in the neural retina of Henle's fiber layer [Subczynski et al., 2010] which is a part of the retina and the melanin is mostly concentrated in the RPE cells [Delori et al., 2001] but can also be found in the choroid (CHO) [Beatrice and Steinke, 1972]. The absorption is assumed to be homogeneous within the tissue layers which means that the pigments are assumed to be equally distributed. Most of the radiation energy that propagates to the retina is

Table 8: Thermal properties of the retina to simulate the heat transfer by a laser source [Jean and Schulmeister, 2017].

thermal property	value
conductivity k	$0.6305\,\frac{\mathrm{W}}{\mathrm{m\,K}}$
specific heat C	$4178\,\frac{\mathrm{J}}{\mathrm{kg\,K}}$
density ρ	$992\,\frac{\mathrm{kg}}{\mathrm{m}^3}$
initial temperature T_0	$310.5\,\mathrm{K}$

absorbed by the RPE and the choroid which supplies the retina with blood. [Geeraets and Berry, 1968; Vassiliadis, 1971]. The absorption within the sclera is neglected since it is lower than in the RPE or the CHO [Vogel et al., 1991]. In addition, the front side of the RPE and the back side of the CHO show a reflection behavior [Delori and Pflibsen, 1989]. In this model multiple reflections are neglected and only one reflection at the tissue boundary is considered. The detailed optical properties of the tissue can be seen in the work of Jean [Jean and Schulmeister, 2017].

A2.4.2 Thermal Interaction at the Retina

The amount of radiant energy that is absorbed by the retinal layers will be directly converted into thermal energy and therefore the absorption behavior of the tissue defines a heat source $q\left(t,\vec{r}\right)$. The heat transfer equation in biological tissues is given by

$$\rho C\frac{\partial T}{\partial t}=k\Delta T+q\left(t,\vec{r}\right)+q_b\left(T\right). \tag{48}$$

The thermal properties of the tissue are listed in Table 8. They are assumed to be homogenous and similar to water since more than 80% of the retina consists of water [Berman et al., 1974]. However, the melanosomes show a higher mass density ρ with about $1400\,\mathrm{kg\,m^{-3}}$ and a lower specific heat capacity C with about $2700\,\mathrm{J\,kg^{-1}\,K^{-1}}$ than water [Neumann and Brinkmann, 2005]. As both of these values appear in equation (48) as a product the calculation results in a similar value as for water. The term $q_b\left(T\right)$ on the right-hand side of the heat equation describes the heat convection in the vascular layers and depends on the specific heat C, the density ρ, the perfusion rate and the arterial blood temperature [Ooi and Ng, 2008]. In the computer model, the heat convection term $q_b\left(T\right)$ is implicitly considered in the boundary conditions of the system. Furthermore, the thermal properties are assumed to be independent of the temperature which results in a linear behavior with regard to the heat source or in case of a laser irradiated retina, to the laser power.

The heat transfer equation is numerically solved with a finite element method. As only a finite volume representing a part of the retina can be modelled, the Neumann

boundary condition is used.

A2.4.3 Evaluation of Thermal Injury Thresholds

To determine the thermal injury threshold value, the Arrhenius equation (43) has to be solved. Here, the temporal temperature behavior of the RPE layer is needed since the lesion forms within this layer [Ham et al., 1970; Beatrice and Steinke, 1972; Lund et al., 2000]. In addition, the model was validated with the definition that there is a MVL which has a diameter of 50 μm for the non-human primate. Therefore, to determine the threshold value the temperature in the RPE layer at the edge of the MVL circle has to be considered. This will result in a value of $\Omega \geq 1$ within the MVL area where all enclosed cells are damaged [Schulmeister et al., 2011]. Smaller damaged areas are not considered to be a lesion. In the computer model the factors of the Arrhenius equation (43) have to be correctly chosen. Here, the frequency factor is set to

$$A = 1.05 \times 10^{95} \, \frac{1}{\mathrm{s}} \tag{49}$$

and the inactivation energy to

$$E = 5.99 \times 10^{5} \, \frac{\mathrm{Joule}}{\mathrm{mol}}. \tag{50}$$

The above mentioned values are adopted from the study of Jean [Jean and Schulmeister, 2017]. With these factors the Arrhenius equation can predict the energy that is needed for a specific heat source to induce an injury.

We would like to emphasize that we have built our model based on the SLM and up to this point the only difference is that we have added a spatial dimension to be able to evaluate non-uniform retinal images. In section A2.5.1, we will discuss another difference, where we introduce an adjusted transmittance function, which is necessary for the investigated beam profiles. We validated our model by comparing the simulation results for circular beam profiles with results of the two dimensional SLM which is described in the work of Jean and Schulmeister [Jean and Schulmeister, 2017]. Here, we have investigated a circular top-hat as well as a circular Gaussian beam profile with different wavelengths between 400 nm and 1000 nm. We performed the simulations for a selected data set where emission durations ranged from 100 μs to 10 s and spot sizes ranged from 1.5 mrad to 100 mrad. The compared parameters are the simulated threshold values and the maximum temperature reached at the RPE. Regarding the injury thresholds, the mean deviation is 0.47 % with a standard deviation of 0.29 %. The results for the maximum temperature have a mean deviation of 0.86 % with a standard deviation of 1 %. These deviations are negligible small and can be explained

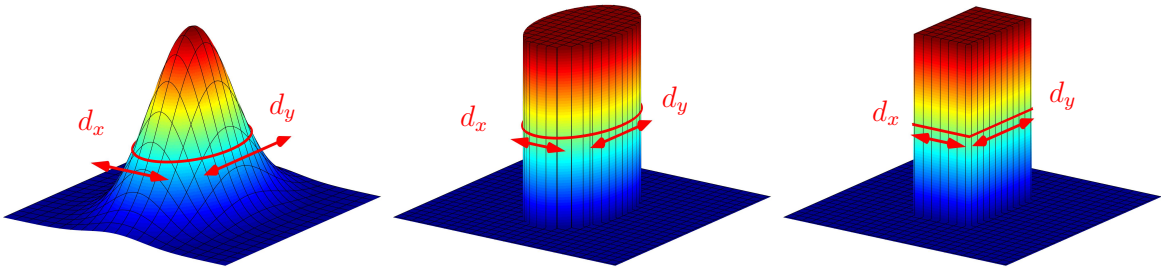

Figure 38: Depiction of an elliptical Gaussian (left) an elliptical top-hat (middle) and rectangular top-hat (right) retinal irradiance profile used to simulate the thermal injury threshold values.

by uncertainties arising from the discretization in the used finite element method. This analysis shows that our model is validated and yields the same results as the SLM.

A2.4.4 Threshold Values for the Human Eye

The SLM is validated against NHP threshold data [Jean and Schulmeister, 2017]. However, the main issue of this investigation is to predict the laser-induced threshold values for non-uniform retinal images regarding human eyes. Therefore, the minimum visible lesion is set to 20 μm even though such small lesions are not detected by ophthalmoscopes. Usually, a minimum lesion diameter of 25 μm or larger can be detected in threshold experiments. [Lund et al., 2001]. Furthermore, the minimum spot size for retinal images is set to 25 μm [Schulmeister et al., 2011; IEC, 2014; ICNIRP, 2013b; Sliney, 2005]. At last, the focal length of the relaxed human eye is set to 16.68 mm [Atchison and Smith, 2000; LeGrand and ElHage, 1980].

The changes made here allow small spot sizes to be considered restrictively. The laser safety standard also assumes smaller spot sizes than those resulting from experimental measurements with NHPs [Kotzur et al., 2021b].

A2.5 Methods and Materials

A2.5.1 Irradiance Profiles on the Retina

In this investigation three different irradiance profiles are considered, the elliptical Gaussian, the elliptical top-hat and the rectangular top-hat. The irradiance profiles are illustrated in Fig. 38. In the following, the irradiance profiles are given in a coordinate system with an x- and y-axis. All profiles are characterized by the two widths d_x and d_y representing the extent of the image in the corresponding orthogonal axis. The Gaussian distribution as well as the elliptical top-hat can be described by an elliptical

shape. With the use of polar coordinates this shape is defined by

$$S^{\text{ell}} : r = r^{\text{ell}}(\varphi), 0 \leq \varphi \leq 2\pi \tag{51}$$

with

$$r^{\text{ell}}(\varphi) = \frac{d_x d_y}{4\sqrt{\left(\frac{d_x}{2}\sin(\varphi)\right)^2 + \left(\frac{d_y}{2}\cos(\varphi)\right)^2}}. \tag{52}$$

The rectangular top-hat is given by a rectangular shape which can be expressed in Cartesian coordinates with

$$S^{\text{rect}} : \begin{cases} -\frac{d_x}{2} \leq x \leq \frac{d_x}{2}, & \text{for} \quad y = \pm\frac{d_y}{2} \\ -\frac{d_y}{2} \leq y \leq \frac{d_y}{2}, & \text{for} \quad x = \pm\frac{d_x}{2} \end{cases}. \tag{53}$$

The top-hat profiles show a constant irradiance value within the area defined by the shapes S^{ell} and S^{rect}. The elliptical Gaussian irradiance distribution is defined by

$$I_{\text{Gaussian}}(r, \varphi) = \exp\left(-4r^2\left(\frac{\cos^2\varphi}{d_x^2} + \frac{\sin^2\varphi}{d_y^2}\right)\right) \tag{54}$$

where d_x and d_y refer to the 1/e-diameter definition. As both profiles are axisymmetric the heat transfer equation (48) can be simplified by defining two symmetry planes where only two octants of the three dimensional model have to be solved.

For the application of the computer model, which is validated using circular retinal images, two issues have to be discussed. The first issue is the determination of the transmittance which gives the amount of radiant energy that propagates to the retina. In case of circular spots, this is given by equation (45) where the effect of intraocular scattering is taken into account. Regarding non-uniform retinal profiles, it was found in our previous investigation [Kotzur et al., 2020c] that a new transmittance equation which is based on equation (45) can be used. Here, equation (45) is integrated along the retinal image shape and divided by the limits of the integration.

For an elliptical top-hat irradiance profile with the widths d_x and d_y the averaged effective transmittance is calculated by

$$\tau_{\text{eff}}^{\text{ell}}(\lambda, d_x, d_y) = \frac{2}{\pi}\int_0^{\frac{\pi}{2}} \tau_{\text{eff}}\left(\lambda, r^{\text{ell}}(\varphi)\right)\, \mathrm{d}\varphi. \tag{55}$$

Here $r^{\text{ell}}(\varphi)$ is described in equation (52).

For a rectangular top-hat irradiance profile the averaged transmittance is calculated

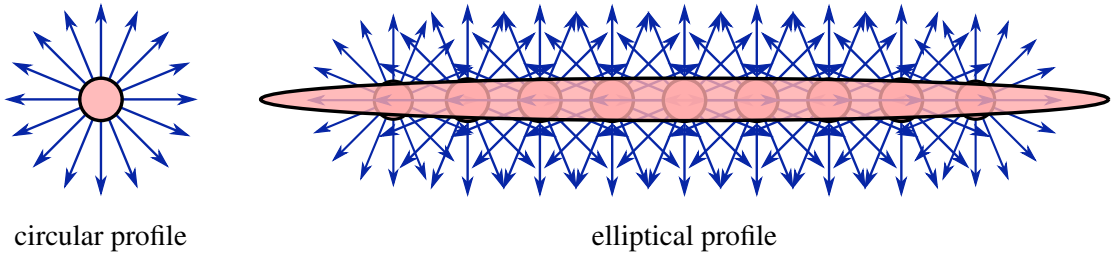

Figure 39: Illustration of intraocular scattering in case of a circular (left) and elliptical (right) irradiance profile. The amount of radiant energy that is scattered out of the defined retinal image is represented by the blue arrows.

by

$$\tau_{\text{eff}}^{\text{rect}}\left(\lambda, d_x, d_y\right) = \frac{2}{\pi}\left(\int_0^{\varphi_C} \tau_{\text{eff}}\left(\lambda, \frac{d_x}{2\cos\left(\varphi\right)}\right) \mathrm{d}\varphi + \int_{\varphi_C}^{\frac{\pi}{2}} \tau_{\text{eff}}\left(\lambda, \frac{d_y}{2\sin\left(\varphi\right)}\right) \mathrm{d}\varphi\right) \tag{56}$$

with

$$\varphi_C = \arctan\left(\frac{d_y}{d_x}\right). \tag{57}$$

The question of how to physically determine the transmittance of non-uniform retinal images is complex and approximations are needed. In the case of circular spots, a function is proposed in the study by Jean and Schulmeister [Jean and Schulmeister, 2017] that depends on the spot size, see equation (45). For smaller spot sizes on the retina, the amount of radiant energy scattered out of the spot increases. In these cases there is mostly forward scattering and the studies of Birngruber *et al.* [Birngruber et al., 1979] show that for spot sizes near the diffraction limit about 50 % of the energy is scattered out. According to equation (45), a circular spot with a diameter of 83.4 μm results in a transmittance of about 77 % of τ_{Total}. Fig. 39 shows schematically in the left figure that for such a circular spot the out scattered radiant energy is isotropic according to equation (45). The right illustration shows an elliptical profile composed of a juxtaposition of circular spots qualitatively explaining the out scattered radiant energy. It can be seen that the radiation scattered out to the left and right of the symmetrical spots compensate each other in the elliptical profile. Above and below the elliptical profile, the radiant energy is still scattered out. Our proposed equation describes this behavior, averaging along the image shape. In the exemplary case of an elliptical profile with widths of 83.4 μm and 1668 μm, the transmittance is approximately 81 % of τ_{Total}. The complex issue of intraocular scattering especially for non-uniform retinal images is approximated by our approach.

The other issue is the definition of the minimal visible lesion (MVL) from section A2.4.4 where the MVL is set as a circle with a diameter of 20 μm. In case of a non-uniform irradiance profile, the temperature curve will show higher values along the

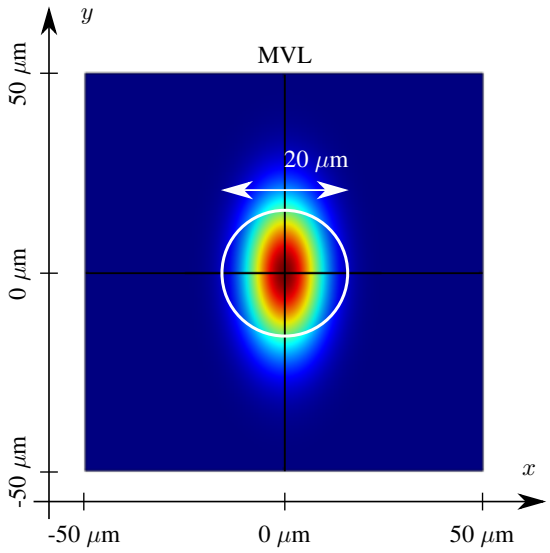

Figure 40: Temperature profile within the RPE layer for an elliptical Gaussian irradiance profile. The MVL is represented by the white circle.

larger image width as there is less cooling. This can be seen in Fig. 40. According to the MVL definition, the Arrhenius integral has to yield values greater than one within the circular area. For this reason, the temperature increase along the shorter axis of the irradiance profile has to be used in equation (43). This issue dominates for retinal irradiance profiles where one width is in the region of the minimal spot size and the other width is much larger. However in this investigation, the profiles have a minimum width of about 85 μm which is about four times the size of the MVL. For this reason, both the temperature increase along the x- and y-direction can be used.

A2.5.2 Maximum Allowed Energy according to the Laser Safety Standard

In this study, the maximum allowed energy (MAE) refers to the total radiant energy entering the eye for which the accessible emission limit (AEL) for laser Class 1 according to the laser safety standard [IEC, 2014] is reached. As the computer model also gives the thresholds in terms of the total intraocular energy, these can be compared directly with the MAE values. When applying the laser safety standard, the eye pupil is described by a 7 mm circular aperture. To calculate the MAE, the angular subtense of the apparent source α and the intraocular factor η_{retina} are needed. The angular subtense α is a term from the laser safety standard [IEC, 2014] and describes the retinal image size. The AEL increases for larger retinal profiles and is therefore dependent on the angular subtense. The angular subtense is determined by varying the angle of acceptance with a field stop in the retinal image [Kotzur et al., 2020b] according to the laser safety standard [IEC, 2014] and the ICNIRP guidelines [ICNIRP, 2013b]. The shape of the

field stop can either be an ellipse or a rectangle with the widths γ_x and γ_y which are referred to as angles of acceptance [IEC, 2011].

The intraocular factor is calculated by dividing the radiant energy contained in the field stops by the total radiant energy of the whole retinal image, which is equal to the energy entering the eye. For normalized irradiance profiles I_{RI}, the total radiant energy is equal to one and the intraocular factor is calculated with

$$\eta_{\mathrm{retina}}^{\mathrm{ell}}\left(\gamma_x, \gamma_y\right) = \int_0^{2\pi} \int_0^{\frac{g_x g_y}{4\sqrt{\left(\frac{g_x}{2}\sin\varphi\right)^2+\left(\frac{g_y}{2}\cos\varphi\right)^2}}} I_{\mathrm{RI}} r \,\mathrm{d}r\mathrm{d}\varphi \tag{58}$$

in case of an elliptical field stop and with

$$\eta_{\mathrm{retina}}^{\mathrm{rect}}\left(\gamma_x, \gamma_y\right) = \int_{-\frac{g_y}{2}}^{\frac{g_y}{2}} \int_{-\frac{g_x}{2}}^{\frac{g_x}{2}} I_{\mathrm{RI}} \,\mathrm{d}x\mathrm{d}y \tag{59}$$

in case of a rectangular field stop. The lengths g_x and g_y are obtained by

$$g_k = 2\tan\left(\frac{\gamma_k}{2}\right) 17\,\mathrm{mm}, \quad \text{with } k = x, y. \tag{60}$$

The length 17 mm is explained by the air-equivalent eye model used in laser safety evaluations and correspond to the distance between the eye lens and retina. The angular subtense is determined by maximizing the relation between the intraocular factor and the AEL from the laser safety standard

$$\left\{ \gamma_x, \gamma_y \left| \max \frac{\eta_{\mathrm{retina}}\left(\gamma_x, \gamma_y\right)}{\mathrm{AEL}\left(\frac{\gamma_x+\gamma_y}{2}\right)} \right\} \right|_{\gamma_x=\alpha_x, \gamma_y=\alpha_y}, \quad \text{with } \gamma_k \in \left[\alpha_{\min}, \alpha_{\max}\left(t\right)\right]. \tag{61}$$

The angular subtense of the apparent source α is then calculated by averaging as follows

$$\alpha = \frac{\alpha_x + \alpha_y}{2}. \tag{62}$$

This procedure is also illustrated in interpretation sheet 1 of the laser safety standard [IEC, 2017]. The limitations $\alpha_{\min}$ and $\alpha_{\max}\left(t\right)$ are defined in the laser safety standard. Using the current standard IEC 60825-1:2014, the minimum limitation is given with

$$\alpha_{\min} = 1.5\,\mathrm{mrad} \tag{63}$$

and the maximum limitation is given with

$$\alpha_{\max}(t) = \begin{cases} 5\,\text{mrad}, & \text{for} \quad t < 625\,\mu\text{s} \\ 200\sqrt{t}\,\text{mrad}, & \text{for} \quad 625\,\mu\text{s} \leq t \leq 0.25\,\text{s} \\ 100\,\text{mrad}, & \text{for} \quad t > 0.25\,\text{s} \end{cases}. \tag{64}$$

The accessible emission limit depends on the averaged angle of acceptance of the field stop. Solving equation (61) gives the angular subtense and the intraocular factor η_{retina}. The MAE is calculated with the relation

$$\text{MAE} = \frac{\text{AEL}(\alpha)}{\eta_{\text{retina}}(\alpha)}. \tag{65}$$

The determination of the angular subtense according to the procedure given in equation (61) strongly depends on the emission duration. There are two time-dependent functions that have an influence on the resulting angular subtense. The first is the maximum limitation in equation (64) which is a decisive factor for retinal image sizes larger than 5 mrad. The second function concerns the behavior of the AEL depending on the angular subtense. For emission durations longer than 10 s, the AEL can show two different behaviors which can be described with the piecewise function [Kotzur et al., 2020b]

$$\kappa(\alpha) = \begin{cases} \alpha, & \text{for} \quad t \leq T_2(\alpha) \\ \alpha\, 10^{-\frac{\alpha}{394\,\text{mrad}}}, & \text{for} \quad t > T_2(\alpha) \end{cases}. \tag{66}$$

The time T_2 is a factor from the laser safety standard which depends on the angular subtense according to

$$T_2(\alpha) = \begin{cases} 10\,\text{s}, & \text{for} \quad \alpha \leq \alpha_{\min} \\ 10 \times 10^{\frac{\alpha - \alpha_{\min}}{98.5\,\text{mrad}}}, & \text{for} \quad \alpha_{\min} < \alpha \leq 100\,\text{mrad} \\ 100\,\text{s}, & \text{for} \quad \alpha > 100\,\text{mrad} \end{cases}. \tag{67}$$

To avoid possible discontinuities in the behavior of AEL, both function behaviors have to be considered, resulting in two α values. Both solutions must be used in equation (65) to find the most restrictive result [Kotzur et al., 2020a].

A2.5.3 Reduction Factor

The reduction factor (RF) is an essential parameter in laser safety [Sliney et al., 2002]. All available emission limits [IEC, 2014; ICNIRP, 2013b] are derived from ED_{50} values which represent the 50 % probability of injury and are understood as threshold values

(THR). In this study, the threshold value is given in terms of the total intraocular energy. By applying the laser safety standard [IEC, 2014] to the investigated retinal images the corresponding maximum allowed energies (MAE) are calculated. The reduction factor is defined as

$$\mathrm{RF} = \frac{\mathrm{THR}}{\mathrm{MAE}}, \tag{68}$$

where both the THR and MAE represent the total intraocular energy which is the radiant energy passing through the 7 mm circular aperture.

The definition of a suitable RF depends on several factors, *e.g.* the general uncertainty of the measured threshold data, the knowledge about the damage mechanism or the differences between the NHP and the human. For this reason, the reduction factor does not always exactly reflect a safety margin between the threshold values and emission limit as there may be different uncertainties in the measured data. The greater the uncertainty is the greater the safety margin is set to derive the emission limit. Different damage mechanisms can lead to different RFs. As for example the photochemical damage mechanism show several uncertainties the reduction factor are relatively high compared to the retinal thermal damage mechanism. In a study by Lund *et al.* where the retina is irradiated for 100 s with a laser of the wavelength 441 nm the reduction factor was determined to be 23 [Lund et al., 2006].

The measured threshold data are investigated with the probit curve introduced by Finney [Finney, 1971]. From the slope of the probit curve the uncertainty can be derived. The probit curve reflects the biological variability and the influences of experimental errors. With the definition of the slope s as

$$s = \frac{\mathrm{ED}_{84}}{\mathrm{ED}_{50}} = \frac{\mathrm{ED}_{50}}{\mathrm{ED}_{16}} \tag{69}$$

the value of one would correspond to the ideal case. For retinal thermal and thermomechanical damage the slope of the probit curve is about 1.15 to 1.2 [Sliney et al., 2002]. Therefore, in case of retinal limits the reduction factor can be below one order of magnitude. The heat source behaves linear in the heat transfer in equation (48) where it is assumed that the retinal thermal properties from Table 8 are constant and independent from the temperature. As the equation is linear to the heat source it is also linear to the laser power. In case of thermal injury if the temperature increase that produces a damage is about 20 K, then half the incoming radiant energy would lead to half the temperature increase. A reduction factor of 10 would therefore lead to a temperature increase of 2 K which can be compared to having a fever. As the thermal injury behaves in a non-linear way this would not result in an activation of photocoagulation. [Birngruber et al., 1978] As a result, a high reduction factor is not needed for the retinal thermal injury thresholds.

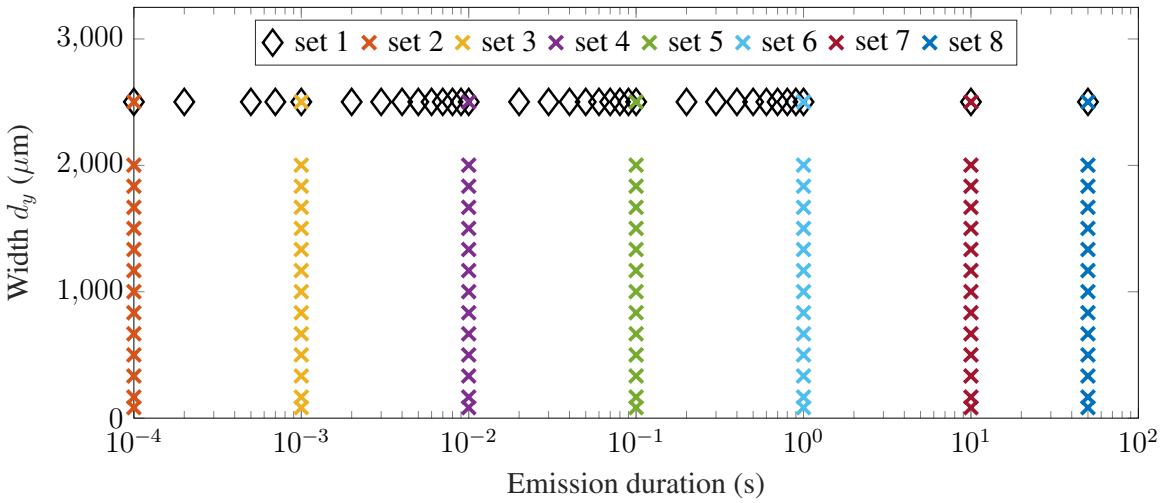

Figure 41: Parameter sets used for the computer model to predict the retinal thermal threshold values for single pulse emissions. For all parameter sets, the width d_x is 83.4 μm.

However, threshold experiments with the minimal spot size have a greater uncertainty and can show slopes larger than 2. Here a reduction factor of one order of magnitude for the minimum spot size is needed as there are several uncertainties with the minimum spot size [Kotzur et al., 2019]. In case of extended sources the actual size of the retinal spot can be experimentally measured and the probit curves show a decreased uncertainty regarding the threshold values. For this reason, a reduction factor of two is sufficient [ICNIRP, 2013b].

A2.5.4 Overview of Simulation Parameters

The computer model was applied to the three types of irradiance profiles from Fig. 38 for a wavelength of 530 nm as the RF is here the lowest for single pulses [Jean et al., 2017, 2019]. Eight parameter sets shown in Fig. 41 were simulated. The widths d_x and d_y refers to the 1/e-definition in case of a Gaussian irradiance profile. In the first parameter set, the emission duration is varied for an elongated profile with the widths d_x=83.4 μm and d_y=2502 μm. For parameter set 2 to 8, the size of the irradiance profile in x-direction is constant whereas in y-direction it is varied from 83.4 μm to 2502 μm. In total around 130 different variations are investigated for each of the three irradiance profiles. As a note, it is mentioned that the term emission duration refers to the duration during which the eye is exposed to the radiation.

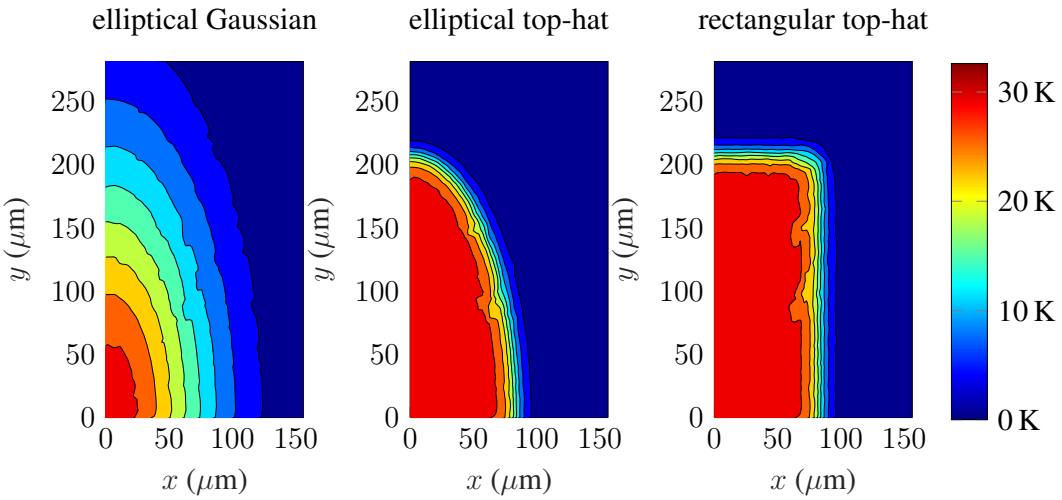

Figure 42: Isothermal curves for an elliptical Gaussian (left), elliptical top-hat (center) and rectangular top-hat (right) irradiance profile with the widths $d_x = 166.8\,\mu$m and $d_y = 417\,\mu$m for a pulse duration of 1 ms. The curves show the temperature increase within the RPE layer at the end of the pulse. Due to axial symmetry, the first quadrant is plotted.

A2.6 Results

A2.6.1 Threshold Values from the Computer Model

The three irradiance profiles from section A2.5.1 lead to different heat propagation within the tissue layers. The thermal behavior in the RPE layer is illustrated by the isothermal curves in Fig. 42. The total radiation energy of the profiles is set to the threshold value and the isothermal curves show the temperature at the end of the pulse. For the elliptical Gaussian profile, the threshold value is about 388 μJ. Regarding the elliptical and rectangular top-hat profiles the thresholds are 375 μJ and 477 μJ. The isothermal curves of both top-hat profiles clearly show a constant temperature increase at the locations where the irradiances are also constant. This causes a strong temperature gradient at the edge of the top-hat profiles. As a finite element method is used, the isothermal curves show fluctuations during the heating process. In case of the rectangular top-hat the corners of the curves are rounded and do not appear as sharp as they would be in an ideal rectangular distribution. The reason for this is that the heat propagation behaves in an isotropic way. On the other side, the Gaussian irradiance profile causes a smoother temperature gradient as the irradiance decreases continuously for larger distances to the center of the profile. For this reason, the inner tissue is better cooled than compared to both top-hats. This can be seen in Fig. 42 where the area with the highest temperature increase is smaller than for the top-hat profiles. As a result, a higher peak irradiance at the center of the profile is needed

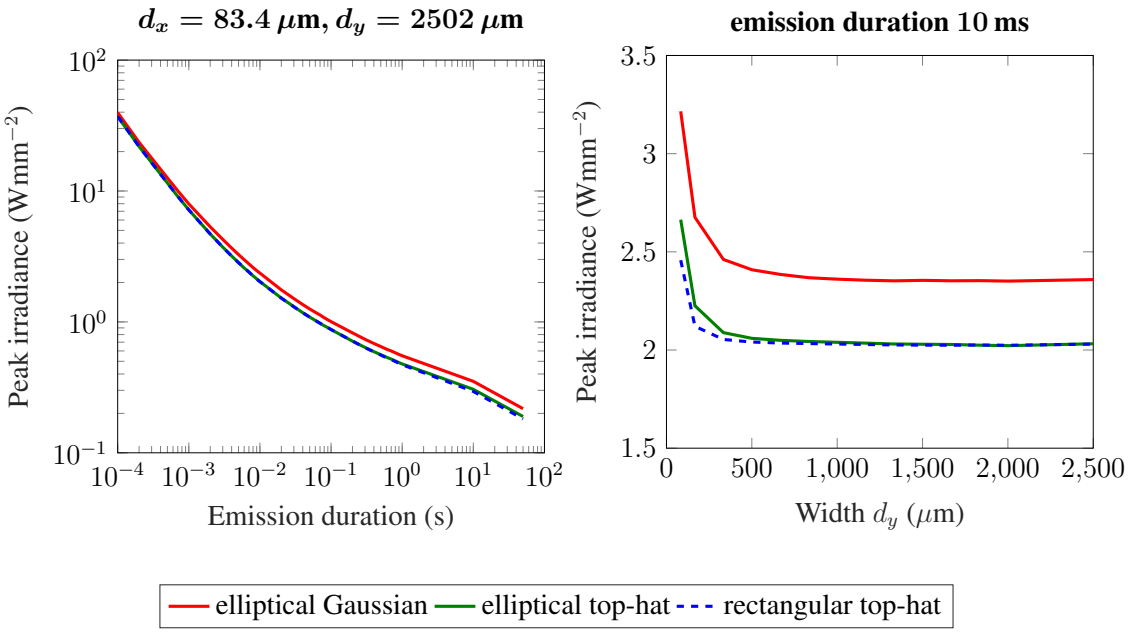

Figure 43: Threshold values expressed by the irradiance at the center of the profile for the elliptical Gaussian, elliptical top-hat and rectangular top-hat profile regarding parameter set 1 (left plot) and 4 (right plot) from Fig. 41. In the left plot the emission duration is varied and in the right plot the width d_y is varied.

for a retinal damage. In the example of the elliptical Gaussian irradiance distribution the peak irradiance is about 7.1 Wmm^{-2}. In case of the top-hat profiles, the threshold irradiances are about 6.8 Wmm^{-2}. 2.5 ms after the pulse, which is not shown in the figure, the hottest region is cooled down by the surrounding tissue and the temperature increase is approximately the half of the maximum temperature increase at the end of the pulse for all profiles. After 20 ms the area of increased temperature is about twice the size of the initial heat region and the maximum temperature increase is about 4 K.

For all parameter sets from Fig. 41 the threshold values are simulated with the computer model for the three irradiance profiles. A comparison is done using the peak irradiance at the center of the profile. Two exemplary results are shown in Fig. 43. For larger emission durations, the peak irradiance to induce thermal damage decreases. The denaturation process can be described by the Arrhenius equation (43) where the temporal temperature behavior is decisive. It follows from this equation that the maximum temperature reached decreases for longer emission durations which lowers the irradiance. In the left plot of Fig. 43 there is no visible difference between the irradiances of both top-hat profiles. This is caused by the similar temperature behavior which can be seen in the isothermal curves in Fig. 42. Both cases result in a large area with the same temperature increase with similar cooling behavior. For the Gaussian profile, the peak irradiance has to be larger to induce a retinal thermal injury due to better tissue cooling of the center.

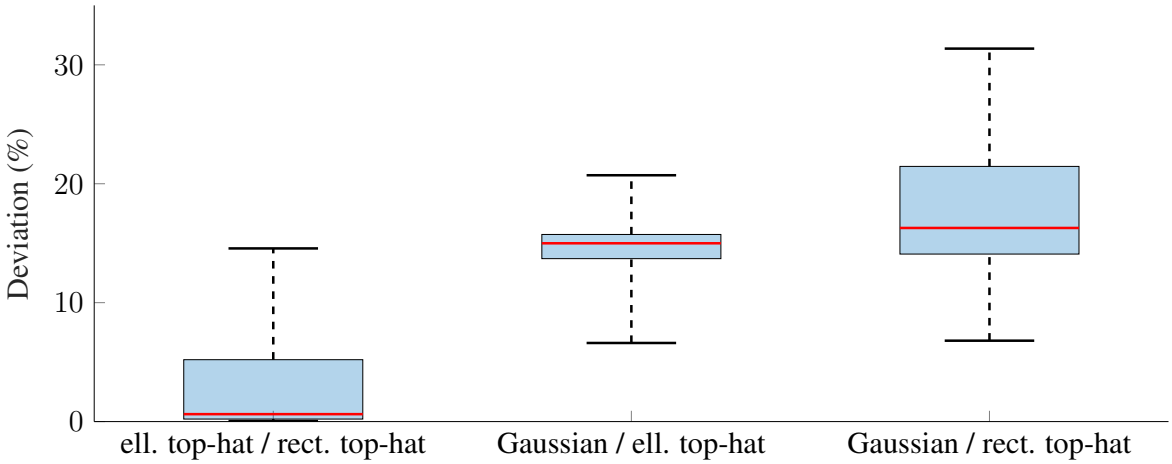

Figure 44: Deviation of the irradiance thresholds for comparing the elliptical top-hat with the rectangular top-hat (left), the Gaussian with the elliptical top-hat (center) and the Gaussian with the rectangular top-hat (right). The median value (red line), the first and third quartile (blue rectangle) and the minimum and maximum values (dashed line) are shown.

By varying the width d_y of the irradiance profiles, the threshold values converge to a constant value. This is caused by a plateau in temperature formed in a larger area in the RPE layer where the cooling from the surrounding tissue is not sufficient to allow a higher irradiance level. Furthermore, this plot shows a larger deviation between the two top-hat profiles. The deviation increases for smaller widths d_y and results from different transmittance values. For decreasing d_y widths, the intraocular scattering is more dominant which leads to a larger difference between the transmittance calculation for an elliptical profile according to equation (55) and for a rectangular profile according to equation (56). A detailed analysis of the deviation between the profiles is shown in Fig. 44 where all parameter sets are included. The deviation between the top-hat profiles is the lowest. Here, the elliptical top-hat show slightly larger irradiance thresholds than the rectangular top-hat. The median deviation is about 0.6 %. The minimum deviation is 0.04 % which appears in parameter set 4 for 10 ms emission duration and the maximum deviation is about 14.6 %. The maximum deviation appears for parameter set 7 (emission duration 10 s) with both widths having a size of 83.4 μm. Between the Gaussian and the both top-hat profiles, the deviations are higher which is due to the thermal behavior. Both minimum deviations appear in parameter set 2 for an emission duration of 10^{-4} s since the pulse is too short for heat propagation. The maximums are reached for parameter set 4 (emission duration 10 ms) regarding the comparison with the elliptical top-hat and for parameter set 5 (emission duration 100 ms) regarding the rectangular top-hat. The maximums are 20.7 % and 31.4 % and appear for a width d_y of 83.4 μm. In case of the right plot of Fig. 44 the maximum deviation is larger than in the center plot. In addition, the standard deviation of the

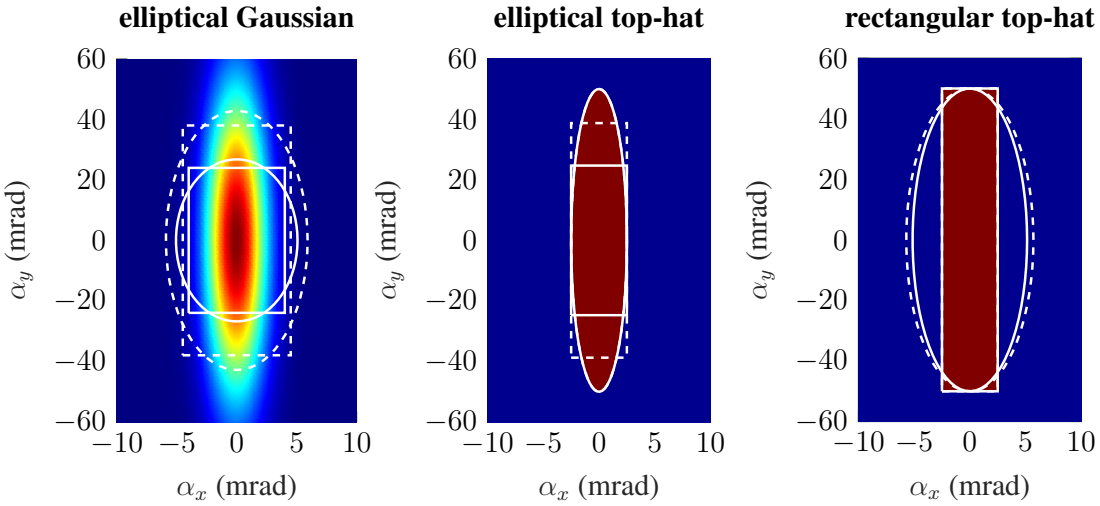

Figure 45: The three different irradiance profiles are shown for parameter set 8 with the emission duration 50 s from Fig. 41 with the width d_y=1668 μm. The angular subtenses are depicted with the white lines. The shape of the white lines correspond to the used field stop shape. All solid white lines show the short time α and the dashed white lines show the long time α. In the plots, the axes are scaled differently and the y axis extends over a longer spatial range than the x axis.

distribution in the right plot is about 6.2 % whereas in the center plot it is about 3.2 %. The reason lies in the different transmittance calculation.

A2.6.2 α and MAE Results according to the Laser Safety Standard

The size of the retinal image is needed for an eye safety evaluation according to the IEC 60825-1:2014 [IEC, 2014]. This size is expressed by the angular subtense of the apparent source and cannot be based on common diameter definitions, *e.g.* the second moment or the Full-width-half-maximum, but has to be derived from the retinal image with the image analysis from equation (61). According to the technical report of the laser safety standard [IEC, 2011] either a rectangular or elliptical shaped field stop can be used for the determination of α. In this investigation, both field stop shapes were applied to calculate the MAE values for the parameter sets from Fig. 41. As previous studies showed [Kotzur et al., 2020b], it must be taken into account that two different α values have to be calculated for emission durations longer than 10 s. This issue is discussed in section A2.5.2. For a better differentiation the two analysis methods are referred to as short time ($t \leq T_2$) and long time ($t > T_2$) method.

As a result, up to four different angular subtenses can be determined for a single retinal image of a specific simulation parameter. In Fig. 45 the α values are shown for an exemplary configuration from Fig. 41 for the three irradiance profiles. The exact sizes

Table 9: List of all α values shown in Fig. 45. For the three irradiance profiles the short and long time method were applied for both a rectangular (rect) and an elliptical (ell) field stop. The angular subtense α is the average of α_x and α_y. In addition, the intraocular factor is calculated.

profile	**Gaussian**				**elliptical top-hat**				**rectangular top-hat**			
α method	short		long		short		long		short		long	
field stop	rect	ell	rect	ell	rect	ell	rect	ell	rect	ell	rect	ell
α_x (mrad)	8.0	10.1	9.0	11.8	5.0	5.0	5.0	5.0	5.0	10.3	5.0	11.4
α_y (mrad)	47.9	53.3	76.0	85.5	49.4	100	77.5	100	100	100	100	100
α (mrad)	28.0	31.7	42.5	48.7	27.2	52.5	41.3	52.5	52.5	55.2	52.5	55.7
η_{retina} (%)	49.0	51.7	70.9	74.8	60.2	100	87.6	100	100	95.9	100	96.7

of the angular subtenses as well as the intraocular factor η_{retina} are listed in Table 9. For the top-hat irradiance profiles (center and right plot of Fig. 45), the angular subtense is equal to the distribution in case of the corresponding field stop shape. Here, the size of the angular subtense in x-direction is 5 mrad and the size in y-direction is 100 mrad for both the short and long time method. Furthermore, the resulting angular subtense contains the total radiant energy leading to an intraocular factor η_{retina} of one. Regarding the Gaussian irradiance distribution (left plot of Fig. 45), all angular subtenses differ. The short time method gives smaller α values than the long time method. The use of the rectangular field stop also leads to smaller angular subtenses than the elliptical shaped field stops. In general, the AEL increases for larger α values as the radiant energy is distributed over a larger area on the retina decreasing the hazard potential. On the other hand, a larger α is accompanied by a higher intraocular factor. For this reason, the most restrictive calculation method cannot be derived directly from the angular subtense but from the MAE calculation. In Fig. 46 the deviation for MAE and α between the elliptical and rectangular field stop is shown. For all results, the analysis with the elliptical field stop yields higher MAE and α values than the analysis with the rectangular field stop. In case of emission durations longer than 10 s where both the long and short time method have to be applied, the most restrictive result was used to obtain the MAE value. The average MAE deviation is about 15.8 %. A minimum deviation of 2.6 % is present in parameter set 8 (emission duration 50 s) for the elliptical top-hat profile where the width d_y is 83.4 %. The maximum deviation is 27.3 % and appears for the rectangular top-hat profile in parameter set 1 with an emission duration of 0.5 ms. A deviation of 27 %, has the highest number of counts in one bin. This is due to parameter set 1 (varying emission duration), set 2 (emission duration 100 μs) and set 3 (emission duration 1 ms) for the elliptical and rectangular top-hat profile. For set 1 the maximum deviation appears for an emission duration of 0.1 ms and for set 2 almost all d_y variations are close to the maximum. For set

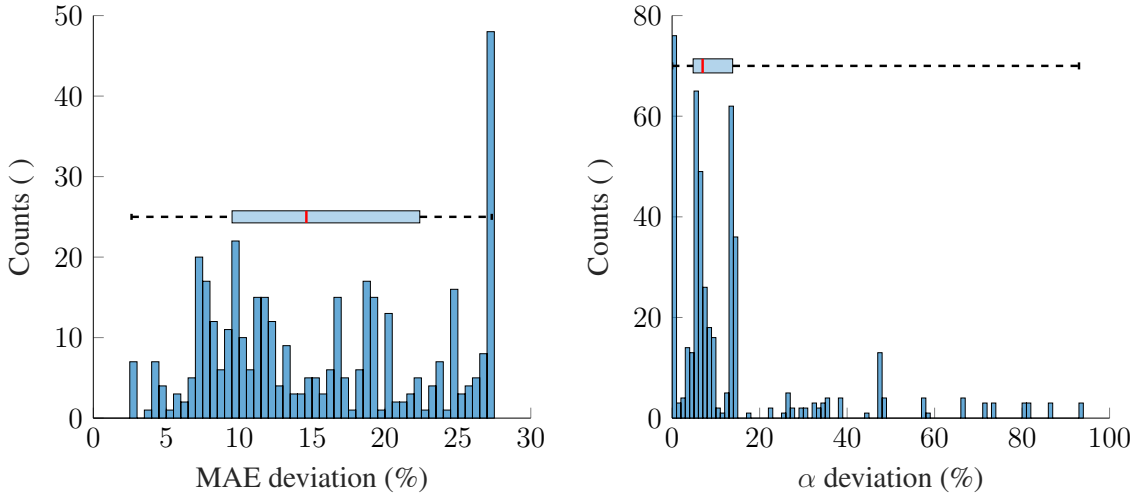

Figure 46: Comparison between the analysis with an elliptical and a rectangular field stop. In the left histogram the deviation regarding the MAE values is shown for a bin size of 0.5 % and in the right histogram the deviation of the α values can be seen for a bin size of 1 %. In addition, the median value (red line), the first and third quartile (blue rectangle) and the minimum and maximum values (dashed line) are presented.

3 a maximum appears for a width d_y of 2502 μm. In general, high deviations are accompanied by short durations and high differences between the d_x and d_y width. In the right histogram of Fig. 46 the α deviation is based on the averaged value between α_x and α_y. The average deviation is about 14 % and the maximum is at 93 % (elliptical top-hat profile, parameter set 8, emission duration 50 s, d_y=1668 μm, short time method). This deviation can also be seen in the center plot of Fig. 45 where the elliptical shaped white line is compared to the rectangular solid white line. A minimum deviation of almost 0 % is primarily reached for all profiles in parameter set 2 for an emission duration of 100 μs as the investigated retinal image sizes are larger than the maximum α limitation according to the laser safety standard. The obtained angular subtenses are limited by $\alpha_{\max}$ which is 5 mrad for an emission duration of 100 μs, see equation (64). In addition, a minimum deviation is also reached for parameter set 3 (emission duration 1 ms) and 4 (emission duration 10 ms) in case of the elliptical top-hat where the width d_y is much larger than d_x. In the right histogram of Fig. 46 there are two peaks with more than 60 counts, respectively. The left peak is located at a deviation of 5.5 % and comes from the rectangular top-hat profile. The right peak appears at 13.5 % and is caused by the Gaussian irradiance profile.

A2.6.3 Reduction Factors

For all parameter sets from Fig. 41 the thresholds were simulated with the computer model, see section A2.6.1, and compared to the laser safety evaluation according to

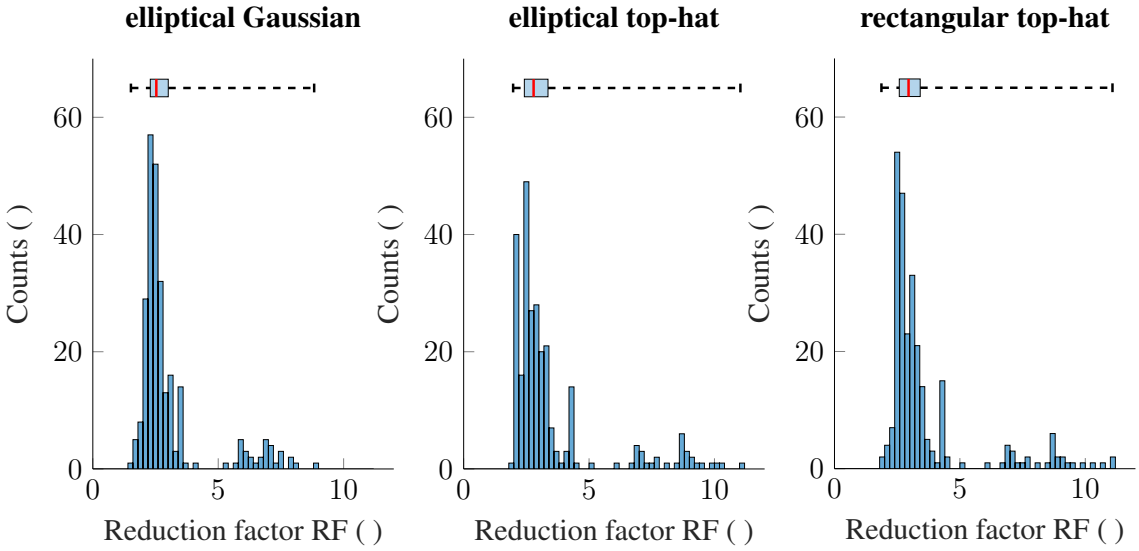

Figure 47: Histograms for the calculated RFs regarding all parameter sets from Fig. 41 for the three irradiance profiles and the two field stop shapes. The bin size of the histograms is set to 0.2. The median value (red line), the first and third quartile (blue rectangle) and the minimum and maximum values (dashed line) are shown. Further statistical values are listed in Table 10.

Table 10: List of statistical values regarding the RFs for all parameter sets from Fig. 41 based on the three irradiance profiles. The RFs based on both elliptical and rectangular shaped field stops were analysed to obtain the statistical data.

Statistics \ Irradiance Profile	ell. Gaussian	ell. top-hat	rect. top-hat	combined
1st quartile	2.29	2.42	2.58	2.42
median	2.53	2.79	2.95	2.72
3rd quartile	3.01	3.36	3.42	3.34
minimum	1.52	1.97	1.87	1.52
maximum	8.83	11.03	11.08	11.08
mean	3.05	3.48	3.62	3.38
standard deviation	1.46	1.93	1.91	1.80

the IEC 60825-1:2014 [IEC, 2014], see section A2.6.2, and the RF is calculated with equation (68). For each of the three irradiance profiles around 250 RFs are calculated. Fig. 47 shows the histogram of all RF for each profile. The corresponding statistical values are listed in Table 10. In general, the RFs are the lowest for the Gaussian profile with a median RF of 2.5 and a minimum RF of 1.5. All minimum RFs from Table 10 are reached for parameter set 4 for an emission duration of 10 ms with d_x=d_y=83.4 μm in case of the elliptical analysis method. The maximum RF appears in parameter set 2 (emission duration 100 μs) for d_y=83.4 μm for the rectangular top-hat profile evaluated

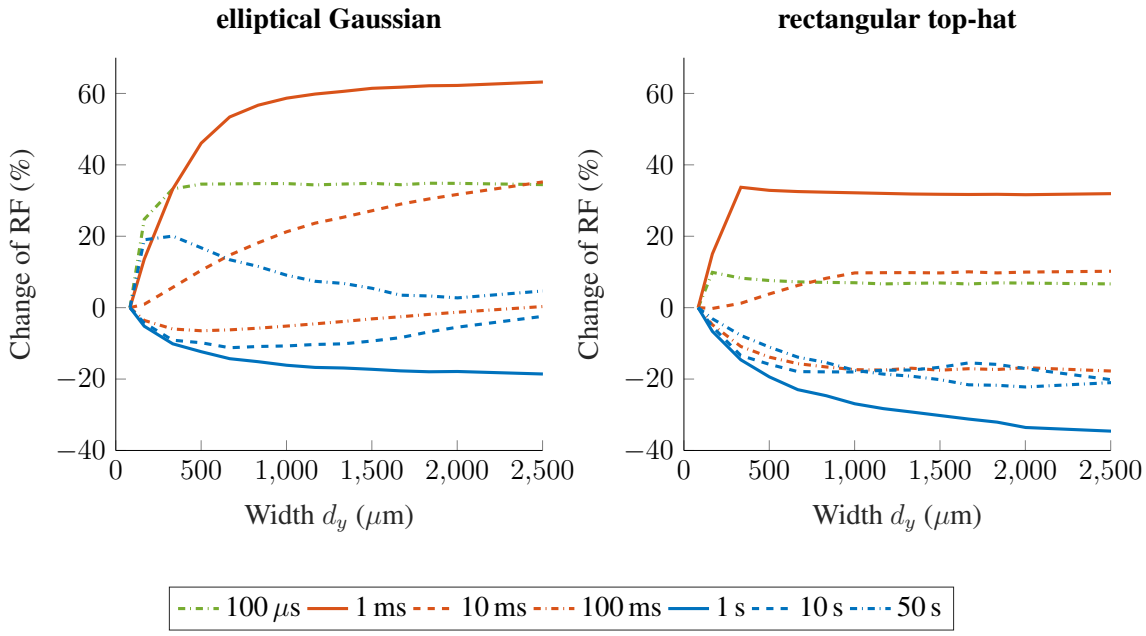

Figure 48: Relative variation of RF as a function of the width d_y for the elliptical Gaussian (left) and rectangular top-hat (right) irradiance profile analysed with rectangular field stops. The plot shows the results for the different emission durations from the parameter sets 2 to 8 of Fig. 41. The relative variation of the RF is calculated by referring to the RF for d_x=d_y=83.4 μm.

by the rectangular analysis method. For the elliptical top-hat the highest RF of 11.03 is reached for parameter set 1 for an emission duration of 10^{-4} s using the rectangular analysis method. This is consistent with the results from the previous section where the rectangular analysis method leads to a more restrictive laser safety evaluation than the elliptical analysis method.

In the following, the relative variation of the RF is investigated for a varying width d_y. As the minimum RF is reached when d_y equals d_x for parameter set 4 (emission duration 10 ms) from Fig. 41, the RF increases for larger d_y values. However, this is not the case for all other parameter sets, which can be seen in Fig. 48 using the example of the elliptical Gaussian and rectangular top-hat irradiance profile. The plot shows an increase in the RF for the emission durations 100 μs, 1 ms, 10 ms and 100 ms. Additionally, the RF has an asymptotic behavior which is more pronounced in the top-hat than in the Gaussian profile. With longer emission durations, the RF for elongated irradiance profiles decreases compared to symmetric profiles. As the RF in these cases has always been above two, the evaluation procedure is nevertheless sufficiently safe [ICNIRP, 2013b]. The analysis of the elliptical top-hat also leads to similar results compared to the rectangular top-hat. The same statements and similar results are obtained for using rectangular field stops.

In summary, all reduction factors are shown in Fig. 49 combining the results for all

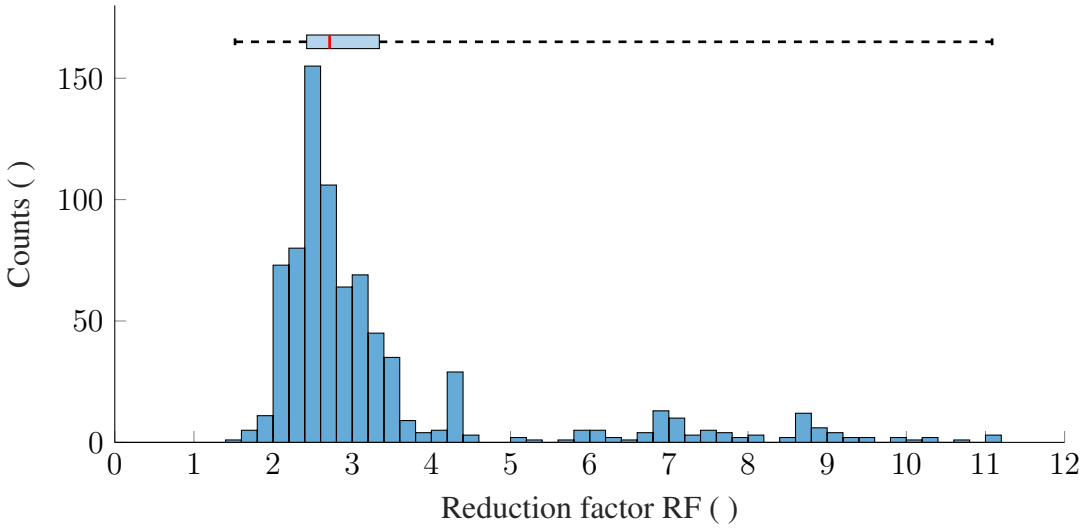

Figure 49: Histogram of all calculated RFs from Fig. 47. The bin size of the histograms is set to 0.2. In addition, the median value (red line), the first and third quartile (blue rectangle) and the minimum and maximum values (dashed line) are shown. Further statistical values are listed in Table 10.

irradiance profiles. The statistical values for all approximately 800 reduction factors are listed in the right column of Table 10. The largest count number in Fig. 49 is reached at a value of 2.5. At this value the elliptical top-hat and rectangular top-hat profile also show the maximum number of counts in Fig. 47. The maximum count number for the Gaussian profile is at a value of 2.3. In total, 17 reduction factors are below a value of two whereas a total of three counts come from the elliptical and rectangular top-hat profile.

A2.7 Summary and Conclusion

In our study, we investigated the applicability of the laser safety standard for non-uniform retinal images. For this purpose, a three dimensional computer model based on the SLM was used to predict the thresholds laser-induced retinal injuries for non-uniform irradiance profiles. The SLM solves the heat equation and the Arrhenius integral with the temporal temperature behavior and is only valid for pulse durations greater than 100 μs.

With an integrating transmittance calculation [Kotzur et al., 2020c], we investigated an elliptical Gaussian, an elliptical top-hat and a rectangular top-hat as retinal irradiance distribution and compared the simulated threshold values with laser Class 1 according to the laser safety standard IEC 60825-1:2014 [IEC, 2014].

We analysed eight different parameter sets with varying emission durations and profile widths. It was found that due to a better tissue cooling for a Gaussian distribution, a higher irradiance than with both top-hats is required to induce a retinal

injury. Here, the average threshold is about 13.9 % higher compared to the elliptical top-hat and 17.3 % regarding the rectangular top-hat. The threshold irradiances for both top-hats are approximately the same in most cases due to their similar thermal tissue behavior.

The calculation of the maximum allowed energy is performed with an image analysis according to the laser safety standard [Kotzur et al., 2020b] with a rectangular and an elliptical shaped field stop. The elliptical shaped field stop leads to larger angular subtenses and larger MAE values then a rectangular shaped field stop. The average deviation for the MAE is about 15.8 % and about 13.6 % for the angular subtense. Short emission durations and large differences between the d_x and d_y width show high MAE deviations with a maximum of 27.3 %. This indicates that for irradiance profiles showing one local maximum or plateau, an eye safety evaluation using rectangular shaped field stops is more restrictive than using elliptical field stops.

At last, the reduction factors are calculated by the ratio between the threshold values and the maximum allowed energies. It was found that the Gaussian irradiance profile shows lower reduction factors than both top-hats. Furthermore, the elliptical top-hat yields lower reduction factors than the rectangular top-hat. For increasing d_y widths, the reduction factors increase for emission durations in the millisecond regime and decrease for the second regime. The total average reduction factor is at 3.38 which verifies the calculation method from the laser safety standard [IEC, 2014] for the investigated irradiance profiles. A total of 17 RFs were found to be smaller than two. The minimum value of 1.52 is reached for a circular Gaussian profile with a width of 83.4 μm and an emission duration of 0.1 ms where the elliptical analysis method is applied.

Complex laser systems have many different parameters affecting the damage thresholds. The available experimental data is limited and it is not possible to analyse all parameters by experiments with NHPs. Therefore, research questions in the field of eye safety can be investigated with simulation models, which have been validated using the available experimental data.

A2.8 Outlook

This publication focuses on single pulse emissions for elongated retinal images based on three types of irradiance profiles. For future investigations, a more broad variety of retinal images should be analysed with regard to the applicability of the calculation procedure according to the laser safety standard IEC 60825-1:2014 [IEC, 2014]. Unlike the investigated retinal images, more complex irradiance profiles can lead to a different thermal behavior where for example different heat regions are formed.

Additionally, the study can be expanded to the topic of pulse trains. For pulsed

emissions, the calculation procedure of the laser safety standard IEC 60825-1:2014 [IEC, 2014] requires three pulse criterions. Recently, a new calculation scheme regarding irregular pulse trains was validated in a study by Jean *et al.* [Jean et al., 2020]. This study was done for circular spots, but further investigations can be performed on non-uniform retinal images.

In general, the used computer model can be applied to spatially and temporally complex emission patterns in order to validate novel calculation schemes.

Disclosures

The authors declare that there are no conflicts of interest related to this article.

Acknowledgements

The authors would like to thank Mathieu Jean and Dr. Karl Schulmeister from the Seibersdorf Labor GmbH for inspiring discussions regarding the simulation of retinal thermal injury thresholds.

A3 Image analysis of retinal images in eye safety evaluations for optical systems

Kotzur, S., Wahl, S., & Frederiksen, A. (2023). Image analysis of retinal images in eye safety evaluations for optical systems. Opt. Eng., 62(1), 016102.
doi:10.1117/1.OE.62.1.016102

A3.1 Abstract

Optical systems that emit radiation between the visible and near-infrared wavelength region pose a potential hazard to human vision as the radiation is imaged on the retina. The radiation interacts with the retinal tissue in a photomechanical, photothermal and photochemical manner which can result in irreversible injuries. To ensure an eye safe system, it is important to correctly apply the laser safety standard IEC 60825-1:2014 or the lamp safety standard IEC 62471:2006. We aim to provide a general calculation procedure for both coherent and incoherent sources which are compliant with the respective safety standards. An air-equivalent eye model generates retinal images. Two software-based calculation methods are introduced which are referred to as image analysis. The first method calculates the angular subtense of the apparent source needed for photomechanical and photothermal limits. The second method applies to photochemical limits. Using exemplary optical systems, the image analysis is investigated. The proposed image analysis gives guidance for missing aspects in the standards and reduces ambiguity and complexity. The proposed method can be used for eye safety evaluations since it follows the concept of the safety standards with conservative approaches.

A3.2 Introduction

The hazard of common laser pointers to the human eye is well known [ICNIRP, 1999; Robertson et al., 2005; Hadler and Dowell, 2013; Löfgren et al., 2013; Schulmeister, 2013; Strzelecki et al., 2017]. Due to the focussing ability of the eye, the irradiance can be increased by a factor of 10^5 when imaged on the retina. Laser pointers with output powers of only a few hundred μW are considered as safe for intentional long-term viewing according to the laser safety standard IEC 60825-1:2014 [IEC, 2014]. In contrast, line lasers which have a collimated and divergent axis are generally allowed to have a higher laser output power as the radiation will be imaged on a larger area on the retina and additionally a less amount of power enters the eye. The determination of the laser class for line lasers requires more extensive calculations in comparison to

laser pointers. The laser classification according to the laser safety standard is more difficult for these systems and in some instances even unclear. This concerns emerging technologies like lidar [Fersch et al., 2017; Beuth et al., 2018] (light detection and ranging) or laser projection systems [Frederiksen et al., 2012; Heussner et al., 2014]. The issue does not only refer to laser systems but also to optical systems emitting incoherent radiation [Jäger and Sternecker, 2016]. By analogy to the laser radiation, these systems can be assigned to so called risk groups according to the lamp safety standard IEC 62471:2006 [IEC, 2006]. Nowadays, the use of light emitting diodes (LEDs) in lamp application is increasing. For example, LEDs are used for the interior and exterior lighting of a vehicle or for the backlight of a smartphone.

Generally, the optical light sources are divided into two groups, namely coherent and incoherent sources. The 'International Comission on Non-Ionizing Radiation Protection' (ICNIRP) publishes guidelines with limits for coherent [ICNIRP, 2013b] and incoherent sources [ICNIRP, 2013a]. To ensure the safety of an optical product, the limits from the laser safety standard IEC 60825-1:2014 [IEC, 2014] and the lamp safety standard IEC 62471:2006 [IEC, 2006] which are generally based on the corresponding ICNIRP documents have to be taken into account. For retinal hazards it is possible to perform an evaluation according to an extended source. In this evaluation procedure, retinal images which are created by placing the light source in front of an eye model are analysed. This procedure is not explicitly described in the current safety standards, which means that there can either be a certain scope for interpretation or some facts are not correctly implemented and the hazard of optical radiation can be underestimated. For this reason, users of the relevant safety standards, for example a manufacturer, a laser safety officer or test laboratories, apply different interpretations which are not always in conformity with the standards and might not be restrictive enough. Therefore, a novel procedure is presented in this publication, which is described in detail and remedies the described problems. This procedure comprises two general image analysis methods for retinal eye safety evaluations according to both safety standards. In one method the angular subtense of the apparent source is determined and in the other method an evaluation regarding the photochemical hazard is performed. The angular subtense describes the retinal spot size and determines the emission limits of the corresponding safety standards. The emission limits depend on the angular subtense and can be assigned to the photomechanical, thermomechanical and thermal retinal injury mechanisms. The limits for the photochemical injury do not depend on the angular subtense. As it was shown in previous investigations [Schulmeister, 2005, 2015, 2019; Kotzur et al., 2019, 2021b, 2020b] the definition of the angular subtense does not follow a common beam diameter definition and is a characteristic value for a specific retinal image. The use of other definitions which are not in accordance with the safety stand-

ards could therefore lead to an underestimation of the hazard. The great advantage of our presented analysis method is that it introduces an unambiguous definition for the angular subtense of the apparent source leading to conservative eye safety evaluations.

The paper is structured as follows. First, the methods are presented, showing how the retinal image analysis procedure is developed in compliance with the requirements of the safety standards. This is followed by the results section, in which this analysis procedure is applied to examples and new findings are drawn from it. Finally, a conclusion and an outlook on further topics follow.

A3.3 Methods

This section details the steps to perform a correct eye safety calculation according to the laser safety standard IEC 60825-1:2014 and the lamp safety standard IEC 62471:2006 for optical systems in the visible and near-infrared wavelength region. To gain a better understanding of the emission limits, this section begins with a brief overview of the possible retinal injuries, namely the photomechanical, thermomechanical, thermal and photochemical damage. This is followed by an outline of the requirements of the two safety standards that contain the emission limits which represent the possible retinal injuries previously mentioned. This forms the framework under which the retinal image analysis procedure is constructed. The following section describes how the accessible emission for retinal images is determined. The accessible emission is an important quantity from the safety standards, since it is directly compared to the accessible emission limits. Finally, in the last section, our developed image analysis is introduced, which is used to perform eye safety evaluations. Here it is distinguished between an analysis concerning the photochemical limits and an analysis for the determination of the angular subtense of the apparent source, which is used for the other retinal limits.

A3.3.1 Retinal Injuries

The most sensitive part of the human eye is the retina where irreversible damages can lead to a permanent loss of vision. A retinal injury can occur for wavelengths in the visible and near-infrared region. The damage mechanism depend on the exposure time, the radiant power and the wavelength of the radiation. Generally there are four different kinds of retinal injuries, the photomechanical, thermomechanical, thermal and photochemical damage.

A3.3.1.1 Photomechanical damage

The photomechanical damage is caused by radiation with pulse durations in the femtosecond and picosecond regime and high irradiances. Here two different processes, the

plasma-induced ablation and the photodisruption, can occur [Niemz, 2004]. In the first process, plasma is formed within the tissue where the whole energy is released in the region of the exposure. The surrounding tissue is not ablated and therefore the damage region is well defined. In case the energy is high enough, the photodisruption occur where a shockwave is formed spreading through the tissue and causing further injuries.

A3.3.1.2 Thermomechanical damage

The thermomechanical damage mechanism appears for exposure duration in the nanosecond and low microsecond regime. Due to a rapid localized heating within the retinal pigment epithelium (RPE) microbubbles around the melanosomes are formed and causing a rupture of the cell structure (intracellular damage) [Brinkmann et al., 2000; Gerstman et al., 1996; Kelly, 1997]. After this microcavitation process, there is a probability that the formed bubble will collaps. This induces shockwaves and acoustic transients which lead to extracellular damage and possibly also to the rupture of blood vessels (haemorrhage). This probability is correlated with the size of the formed microbubble.

A3.3.1.3 Thermal damage

The third damage mechanism is the thermal injury which is dominant for exposure durations between the microsecond and second regime. These injuries are basically a burned area within the retina and are visible within 24 hours after exposure. The thermal damage is the denaturation of the proteins due to the heating of the tissue [Birngruber et al., 1985]. The heating of the tissue results from the absorption of the radiation mainly within the RPE layer [Ham et al., 1970; Beatrice and Steinke, 1972]. Since the absorption in the RPE layer is largely independent of wavelength, the only wavelength dependence of this damage mechanism is the transmission behavior during propagation through the eye. The damage criterion is not based on a temperature increase limit but rather on the temporal temperature profile. Analytically, the thermal retinal injury can be described using the Arrhenius equation which gives the concentration of denatured molecules [Jacques, 2006; Pfefer et al., 1999; Kotzur et al., 2020c, 2021a]. The thermal damage mechanism is strongly coupled to the shape and size of the retinal image and the exposure duration. Larger retinal images result in higher injury thresholds as the radiant energy is distributed over a larger area. However above a certain maximum spot size the hazard does not decrease any more, since the tissue in the center of the spot is no longer sufficiently well cooled. The criterion for this maximum thermal spot size depends on the exposure time [Schulmeister et al., 2008].

A3.3.1.4 Photochemical damage

The last retinal injury mechanism is the photochemical damage. It is a long-time cumulative process primarily for the blue wavelength region. Radicals are formed which can cause photic retinopathy for exposure durations longer than 1 s [Wu et al., 2006; Hunter et al., 2012; Ivanov et al., 2018]. The photon energy causes the creation of singlet oxygen which is a reactive form of oxygen and leads to reactions with the surrounding molecules (photo-oxidation). The molecule bonds of several molecules can break resulting in the death of a cell. The damage develops after a period of 24 to 48 hours after exposure. There are two types of photochemical damage mechanisms, namely the Noell damage [Noell et al., 1966a] (class I damage) and Ham damage [Ham et al., 1978] (class II damage). The class I damage mainly refers to reactions concerning the photoreceptors and its action spectrum approximately behaves like the visual pigment absorption spectrum. In case of class II photochemical damage, the RPE layer is mainly damaged and the action spectrum shows a peak in the ultraviolet range, which is why this damage is also referred to as 'blue-light hazard'. Current laser and lamp safety standards provide emission limits on class II photochemical damage. Unlike the thermal damage, the photochemical damage strongly depends on the wavelength and is independent on the size of the retinal image. It is indicated that the photochemical damage favours the pathogenesis of age-related macular degeneration.

The laser safety as well as the lamp safety standard provide several emission limits which represent the different retinal injury mechanisms. The emission limits depend on the wavelength of the radiation, the emission duration and in case of photomechanical, thermomechanical and thermal limits on the retinal spot size expressed by the angular subtense of the apparent source α. As it is shown in this investigation, the angular subtense can be obtained by an image analysis applied on the retinal image. The angular subtense is a characteristic value that depends on the irradiance distribution on the retina. The photochemical limits do not depend directly on the retinal spot size, but have to be applied to a fixed area on the retina.

A3.3.2 Requirements Defined in the Standards

In the following, the methods to perform eye safety evaluations for systems emitting optical radiation described in the laser safety standard IEC 60825-1:2014 and the lamp safety standard IEC 62471:2006 are used. Both standards require the use of an imaging system representing the human eye for the generation of retinal images. Table 11 and Table 12 summarize the most important specifications for the retinal hazard evaluation. The retinal hazard region for incoherent sources (380 nm to 1400 nm) is larger than for

Table 11: List of the relevant specifications of the laser safety standard for the evaluation of the retinal hazard. The capital letter (M) represents the 'magnifying measurement condition' of the laser safety standard. Some parameters have a dependence on the emission duration t.

Specification	IEC 60825-1:2014 [IEC, 2014]
Wavelength region (i) Thermal/thermomechanical hazard (ii) Photochemical hazard	 400 nm to 1400 nm 400 nm to 600 nm
Diameter of aperture stop	7 mm, 50 mm (M)
Minimum angular subtense $\alpha_{\min}$	1.5 mrad, 1.5/7 mrad (M)
Maximum angular subtense $\alpha_{\max}$	$\alpha_{\max}(t) = \begin{cases} 5\,\text{mrad}, & \text{if } t < 625\,\mu\text{s} \\ 200\sqrt{t/1\,\text{s}}\,\text{mrad}, & \text{if } 625\,\mu\text{s} \le t \le 0.25\,\text{s} \\ 100\,\text{mrad}, & \text{if } t > 0.25\,\text{s} \end{cases}$ $\alpha_{\max}(t)/7$ (M)
Angle of acceptance γ_{ph} (for photochemical hazards)	$\gamma_{\text{ph}}(t) = \begin{cases} 11\,\text{mrad}, & \text{if } 10\,\text{s} < t \le 10^2\,\text{s} \\ 1.1\sqrt{t/1\,\text{s}}\,\text{mrad}, & \text{if } 10^2\,\text{s} < t \le 10^4\,\text{s} \\ 110\,\text{mrad}, & \text{if } 10^4\,\text{s} < t \le 3\times10^4\,\text{s} \end{cases}$ $\gamma_{\text{ph}}(t)/7$ (M)

Table 12: List of the relevant specifications of the lamp safety standard for the evaluation of the retinal hazard. Some parameters have a dependence on the emission duration t and luminance L_{V}.

Specification	IEC 62471:2006 [IEC, 2006]
Wavelength region (i) Thermal hazard (ii) Photochemical hazard	 380 nm to 1400 nm 300 nm to 700 nm
Diameter of aperture stop	$d_{\text{Ap}}(t, L_{\text{V}}) = \begin{cases} 3\,\text{mm}, & \text{if } t > 0.25\,\text{s},\ L_{\text{V}} > 10\,\frac{\text{cd}}{\text{m}^2} \\ 7\,\text{mm}, & \text{else} \end{cases}$
Minimum angular subtense $\alpha_{\min}$	1.7 mrad
Maximum angular subtense $\alpha_{\max}$	100 mrad
Angle of acceptance γ (field-of-view)	$\gamma(t) = \begin{cases} \alpha_{\min}, & \text{if } t \le 0.25\,\text{s} \\ \alpha_{\min}\sqrt{t/0.25\,\text{s}}\,\text{mrad}, & \text{if } 0.25\,\text{s} < t \le 10\,\text{s} \\ 11\,\text{mrad}, & \text{if } 10\,\text{s} < t \le 100\,\text{s} \\ \min\left(11\sqrt{t/100\,\text{s}}\,\text{mrad}, \alpha_{\max}\right), & \text{if } 10^2\,\text{s} < t \le 10^4\,\text{s} \\ \alpha_{\max}, & \text{if } t > 10^4\,\text{s} \end{cases}$

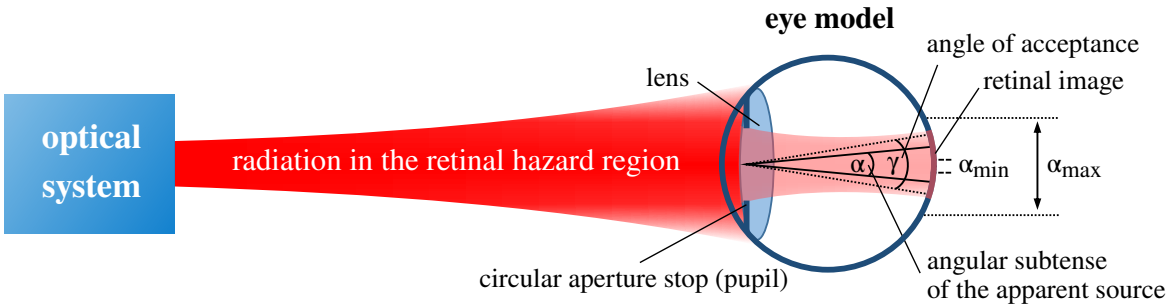

Figure 50: Illustration of the requirements from the laser and lamp safety standard listed in Table 11 and Table 12 for evaluating the retinal hazard using an eye model. In this exemplary figure, a divergent laser beam enters a relaxed eye and creates a large retinal image.

coherent sources (400 nm to 1400 nm). To generate the retinal images for radiation in these wavelength regions, it is necessary to consider an eye model. Fig. 50 shows the eye model as ideal imaging system according to the safety standards. Both safety standards refer to a circular aperture stop with 7-mm diameter representing a wided pupil. In addition, the lamp safety standard makes an exception for sources with emission durations longer than 0.25 s and having luminances above $10\,\mathrm{cd\,m^{-2}}$ where the diameter is assumed to be 3 mm. This refers to a contraction of the eye pupil, which adjusts to the surrounding brightness. Usually the effect is accounted for by the fact that a measurement is still performed with a 7-mm aperture stop, but the corresponding limit values are increased by a factor of $(7/3)^2$. The aperture stop defines the intraocular radiant power and in case of coherent radiation it can also influence the shape of the retinal image [Kotzur et al., 2019, 2021b].

The size of the retinal image is expressed by the angular subtense of the apparent source. In both standards there is a lower and upper limitation of the angular subtense. The lower limit α_{min} considers that the radiation cannot be focused on an infinitely small spot. This size is often associated with the resolution of the human vision [ICNIRP, 2013b; Gross et al., 2008a]. However, as scattering effects influence the minimum spot size this value was rather derived by experimental measurements [Sliney, 2005]. As a counterpart to the minimum spot size there is also a maximum spot size defined. The angle α_{max} represent the thermodynamic behavior for large retinal spots where the surroundings cannot sufficiently dissipate the heat of the center of the spot. Therefore the emission limits do not increase further for angles α larger than α_{max}. The definition of the maximum spot size is time dependent in the laser safety standard which is not the case for the lamp safety standard. In addition to the angular subtense α of the apparent source, the angle of acceptance is defined which is a fixed measurement angle. In case of the laser safety standard, the angle of acceptance γ_{ph} is used to determine the accessible emission which is compared to photochemical emission limits.

For incoherent sources, the lamp safety standard defines an angle of acceptance γ that is used as the field-of-view to determine the radiance representing the accessible emission. The time dependent definition of the field-of-view $\gamma(t)$ is usually not needed as the risk group classification is performed for specific emission durations, namely 0.25 s, 100 s and 10 000 s according to the lamp safety standard. For these emission durations the field-of-views are 1.7 mrad, 11 mrad and 100 mrad.

Another difference is the 'magnifying measurement condition' (M) which is only defined in the laser safety standard (IEC 60825-1:2014 [IEC, 2014], Table 10, Condition 1). This measurement condition represents the use of viewing aids, *e.g.* telescopes or binoculars potentially increasing the hazard. In these cases the retinal image is generated with an aperture stop with a diameter of 50 mm. To simulate an enlarged retinal image, the obtained angular subtense of the apparent source is increased by a factor of 7 for the calculation of the emission limit. As a consequence, the corresponding α limitations and the angle of acceptance γ_{ph} are reduced by this factor.

A3.3.2.1 Limits for coherent sources

The laser safety standard [IEC, 2014] defines a set of accessible emission limits (AEL) which can be assigned to all kinds of retinal damage mechanisms, namely the photomechanical, thermomechanical, thermal and photochemical damage. Except for the photochemical limits, all other limits show a dependency on the size of the retinal image which is expressed by the angle that is subtended by the image. This angle is referred to as the angular subtense of the apparent source. All emission limits are either given in units of the radiant power Φ (in W) or the radiant energy Q (in J). The retinal limits that depend on the angular subtense follow the piecewise function κ^{C}

$$\kappa^{\mathrm{C}}(\alpha) = \begin{cases} \alpha, & \text{if } t \leq T_2(\alpha) \\ \alpha\, 10^{-\frac{\alpha}{394\,\mathrm{mrad}}}, & \text{if } t > T_2(\alpha) \\ \alpha\, 10^{-\frac{7\alpha}{394\,\mathrm{mrad}}}, & \text{if } t > T_2(7\alpha) \text{ and (M)} \end{cases}, \tag{70}$$

where the time $T_2(\alpha)$ is defined by

$$T_2(\alpha) = \begin{cases} 10\,\mathrm{s}, & \text{if } \alpha \leq \alpha_{\min} \\ 10 \times 10^{\frac{\alpha-\alpha_{\min}}{98.5\,\mathrm{mrad}}}\,\mathrm{s}, & \text{if } \alpha_{\min} < \alpha \leq 100\,\mathrm{mrad} \\ 100\,\mathrm{s}, & \text{if } \alpha > 100\,\mathrm{mrad} \end{cases}. \tag{71}$$

This time T_2 is a characteristic value from the laser safety standard. For emission durations higher than T_2, the limit is temporally constant in terms of the radiant power. The biophysical reason are eye movements blurring the retinal image for long-

term exposures.

The photochemical limits are independent of the angular subtense α or the angle of acceptance γ_{ph} and only depend on the wavelength of the radiation and on the emission duration. It is not necessary to specify the photochemical limits here, as they do not influence the image analysis for photochemical hazards.

A3.3.2.2 Limits for incoherent sources

For incoherent sources, the lamp safety standard [IEC, 2006] provides photochemical limits and limits depending on the angular subtense of the apparent source. All limits are given in radiance L or time-integrated radiance. One exception is the photochemical limit for small sources where the limit is given in terms of the irradiance. However, this limit is derived from the general photochemical limit that is expressed in radiance and therefore the photochemical limit for small sources is not considered here. Similar to the laser safety standard, the photochemical limits do neither depend on the angular subtense nor the angle of acceptance γ_{ph}. Therefore, it is not necessary to provide the limits as the image analysis is not affected in case of the photochemical regime.

The other retinal limits in the lamp safety standard that depend on the angular subtense refer to the thermal hazard. The retinal thermal emission limit is given in radiance and follows

$$\kappa^{\mathrm{I}}(\alpha) = \frac{1}{\alpha}. \tag{72}$$

This is a further difference to the laser safety standard which provides limits for the thermal, thermomechanical and photomechanical hazard. Another difference is that the lamp safety standard [IEC, 2006] defines the angular subtense of the apparent source by the 50% emission points of the retinal image. In a further note of the lamp safety standard it is defined that for multiple source elements the limit has to be compared to each source element and the source as a whole.

A3.3.2.3 Implementation of the standard requirements

The laser safety standard and the lamp safety standard give the requirements for performing eye safety evaluations of optical systems. Based on these requirements, we developed the image analysis which is applied on retinal images. Here, a distinction is made between two analysis procedures, namely the determination of the angular subtense of the apparent source α and the analysis with photochemical retinal limits. Fig. 51 shows an overview on how to perform the image analysis and shows where to find the relevant evaluation steps in the corresponding sections of this paper. In the first evaluation step, the retinal image has to be created. This is realized by placing the optical system in front of an eye model. The retinal image is given by the irradiance

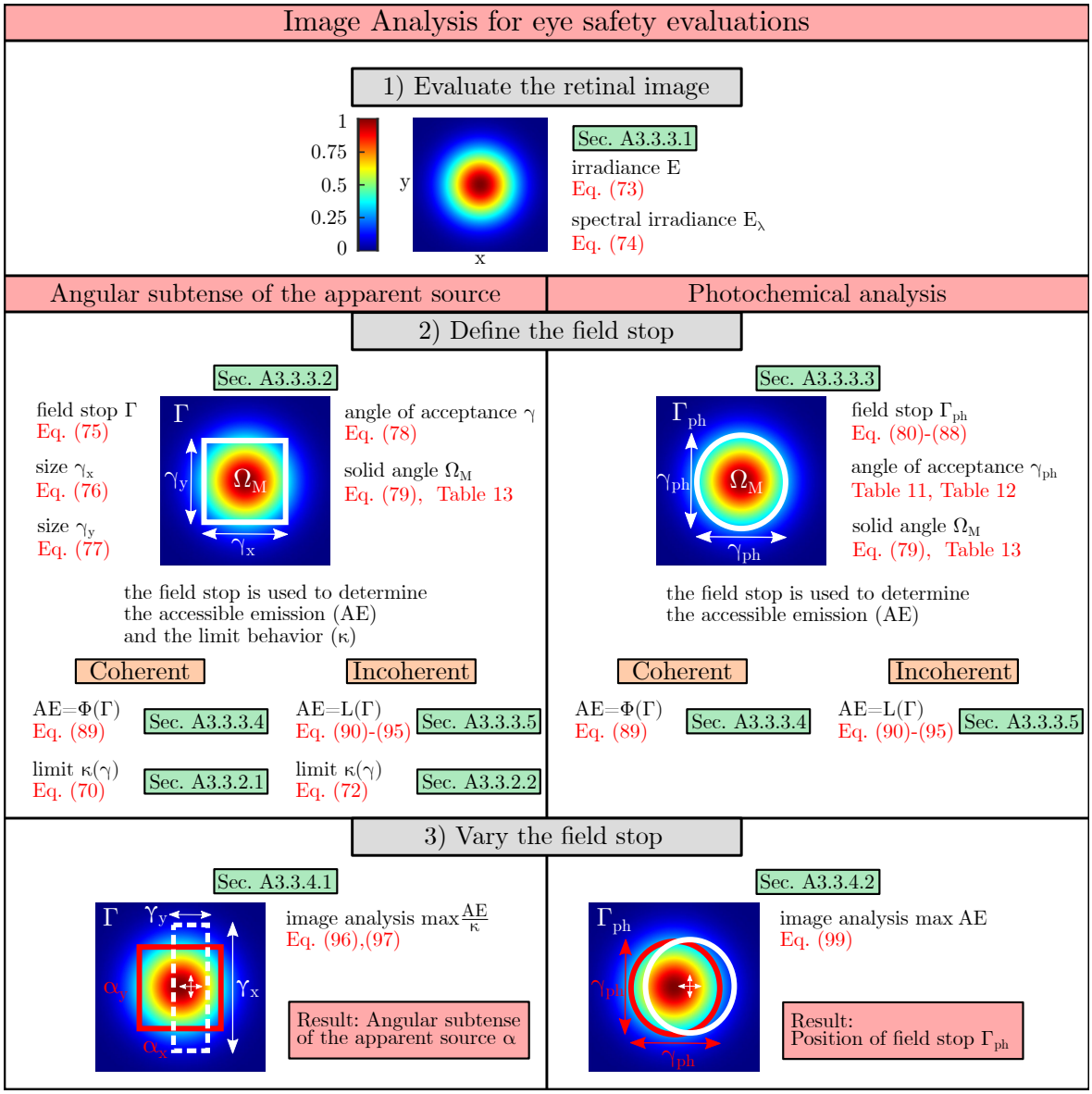

Figure 51: Illustration to give an overview over the image analysis used to perform eye safety evaluations on coherent as well as on incoherent sources. The green boxes show in which section of this paper the evaluation procedure is described and the red highlighted equations show where to find the corresponding formula. The image analysis can be used to obtain the angular subtense of the apparent source α and to perform an evaluation regarding the photochemical limits. The first step of this overview shows the colorbar that is used for all retinal images in this publication.

E or spectral irradiance E_λ distribution, see section A3.3.3.1. On the left side of the retinal image in the first step, the corresponding color bar is shown. Since the two analysis procedures are independent of the scaling of the irradiance distribution, the retinal image is normalized with respect to the maximum value. For this reason, the color bar has a value range from zero to one. As the normalization if performed on all retinal images in this study, the same color bar can be applied to them. In the

second step, a field stop is placed within the retinal image to determine the accessible emission. In case of the determination of the angular subtense the limit behavior κ is also evaluated. This procedure is described in section A3.3.3.2 and section A3.3.3.3. In the last evaluation step, the field stop is varied according to the procedure described in section A3.3.4.1 for determining the angular subtense α and section A3.3.4.2 for the photochemical analysis.

A3.3.3 Accessible Emission

The accessible emission (AE) is the measured or simulated physical quantity that has to be compared with the accessible emission limit. Since this paper presents a method for eye safety evaluations, it does not matter whether the quantities are measured or simulated, and the two terms measurement and simulation are used synonymously. Determining the accessible emission differs for coherent and incoherent sources. In case of coherent radiation, the accessible emission is either expressed in terms of the radiant power Φ or of the radiant energy Q. For the determination of the angular subtense it is irrelevant which one is used and here only the radiant power will be considered. In case of incoherent sources, the radiance L or the time-integrated radiance is needed. All quantities are evaluated by taking the amount of radiation into account that is contained within a field stop. According to the safety standards, the field stop is placed in the retinal image and subtends the angle of acceptance. For the determination of the AE, an eye model is needed with which the retinal images are created. In this study, an ideal air-equivalent eye model is used as it yields conservative results [Kotzur et al., 2021b] and shows a plane retina. It consists of a circular aperture with a diameter of d_{Ap}=7 mm simulating the eye pupil, an ideal lens with focal length f and a plane detector which represents the retina. The distance between the detector and the ideal lens is given by d_2=17 mm. The focal length of the lens can vary between 14.52 mm and 17 mm to simulate different accommodation distances from 10 cm to infinity. In Table 11 and Table 12 there are two exceptions listed regarding the definition of the circular aperture diameter. In the laser safety standard a diameter of 50 mm has to be used for the magnifying measurement condition and in the lamp safety standard a diameter of 3 mm is used for bright sources and long emission durations. Both exceptions will not be considered in this investigation as they have no influence on the evaluation procedure of retinal images.

In the following, the relevant measurand of the retinal image will be introduced. Then the procedure to calculate the angle of acceptance and the field stop for photochemical limits is shown. At last, the evaluation of the accessible emission expressed in radiant power and radiance is presented.

A3.3.3.1 The retinal image in eye safety evaluations

Different physical quantities are required for eye safety evaluations of coherent and incoherent sources. These required physical quantities can be calculated from the retinal image which is obtained by exposing the air-equivalent eye model to the radiation. The retinal image is the irradiance distribution at the detector for a specific focal length. The irradiance E is calculated from the radiant power Φ with

$$E = \frac{\mathrm{d}\Phi}{\cos\theta_\mathrm{e}\,\mathrm{d}A} \tag{73}$$

where the radiant power is divided by an infinitesimal element of a surface $\mathrm{d}A$ of the projected area having a normal vector at an angle of θ_e to the direction of the radiation. In case of incoherent sources or of coherent sources operating at multiple wavelengths, the spectral irradiance E_λ

$$E_\lambda = \frac{\mathrm{d}^2\Phi}{\cos\theta_\mathrm{e}\,\mathrm{d}A\,\mathrm{d}\lambda} \tag{74}$$

is needed. The procedure for considering spectral irradiance is described in detail in the lamp standard for incoherent sources where a weighted irradiance is determined. For the evaluation of coherent sources with multiple wavelengths, the ratios between the accessible emission and the accessible emission limit for the individual wavelengths must be evaluated additively according to the laser safety standard.

A3.3.3.2 Angle of acceptance and solid angle

The angle of acceptance is a term from the safety standards and refers to the size of a field stop which is used to determine the amount of radiant power Φ within the field stop. In the following, a general definition of the field stop and its solid angle will be introduced. It is emphasized that a field stop is used for all types of retinal limits. However, the eye safety evaluation differs. While the field stop is clearly defined for the photochemical limits, only an implicit indication is given for the other limits. The other limits depend on the angular subtense of the apparent source and the field stop to measure the AE has to be chosen to be identical to the angular subtense. As the angular subtense is an unknown parameter in the beginning of the evaluation, all possible field stops have to be taken into account to find the angular subtense. For this reason, the general definition of the field stop in this section is mainly used for the limits that depend on the angular subtense.

In general, the field stop can be varied in its size, orientation and position. In the

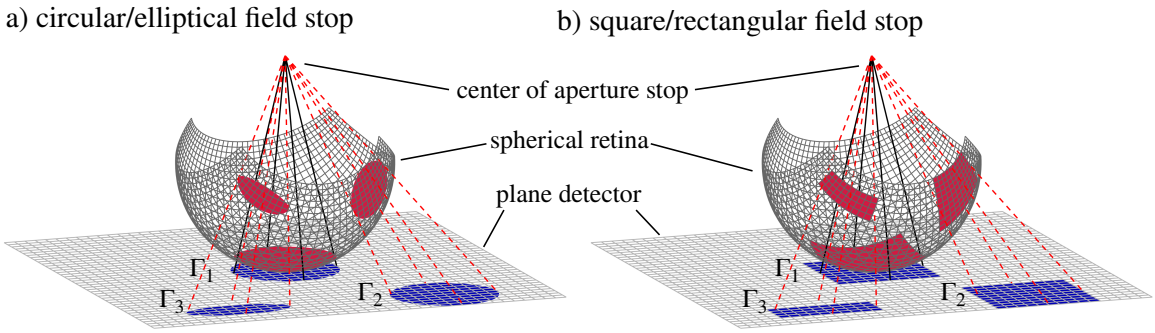

Figure 52: Visual difference between the measured irradiance profiles on the plane detector using the air-equivalent eye model (blue areas) and the actual retinal image of the human eye (red areas). In the left figure a) the profiles are measured with a circular shaped (Γ_1, Γ_2) and an elliptical shaped (Γ_3) field stop. In the right figure b) the field stops are square (Γ_1, Γ_2) and rectangular (Γ_3) shaped. The corresponding field stops in the left and right picture have the same angle of acceptances γ_x and γ_y.

following, the field stop is defined by an area Γ within the detector plane:

$$\Gamma : \quad (\gamma_x, \gamma_y) \mapsto \begin{pmatrix} x(\gamma_x, \gamma_y) \\ y(\gamma_x, \gamma_y) \end{pmatrix} \tag{75}$$

Here, the angles γ_x and γ_y are limited by the requirements from Table 11 and Table 12. As there is no specification regarding the shape of the field stop, we use either a rectangular shaped or an elliptical shaped field stop [IEC, 2011]. The reason why the angles γ_x and γ_y are used to express the size of the field stop can be seen in Fig. 52. As the air-equivalent eye model is used, the simulated retinal images are measured in a plane while in a realistic eye the radiation would be imaged on a sphere. Due to the projection, the area defined by a field stop Γ_i would be decreased on the curved retina. However, the size of the field stop expressed by the angles γ_x and γ_y remain unchanged. In Fig. 53 an exemplary measured retinal image is shown together with the field stop Γ with the half widths a and b, the center $\mathbf{M} = (x_0, y_0, d_2)$ and the rotation angle δ around the center. The angle of acceptance is defined as the angle between the vectors which are pointing from the center of the eye pupil (coordinate origin) to the edges of the field stop. For each angle γ_x and γ_y the field stop Γ can vary in its shape, position $\mathbf{M}$ and its rotation δ. Here, the rotation angle can be limited to be within a

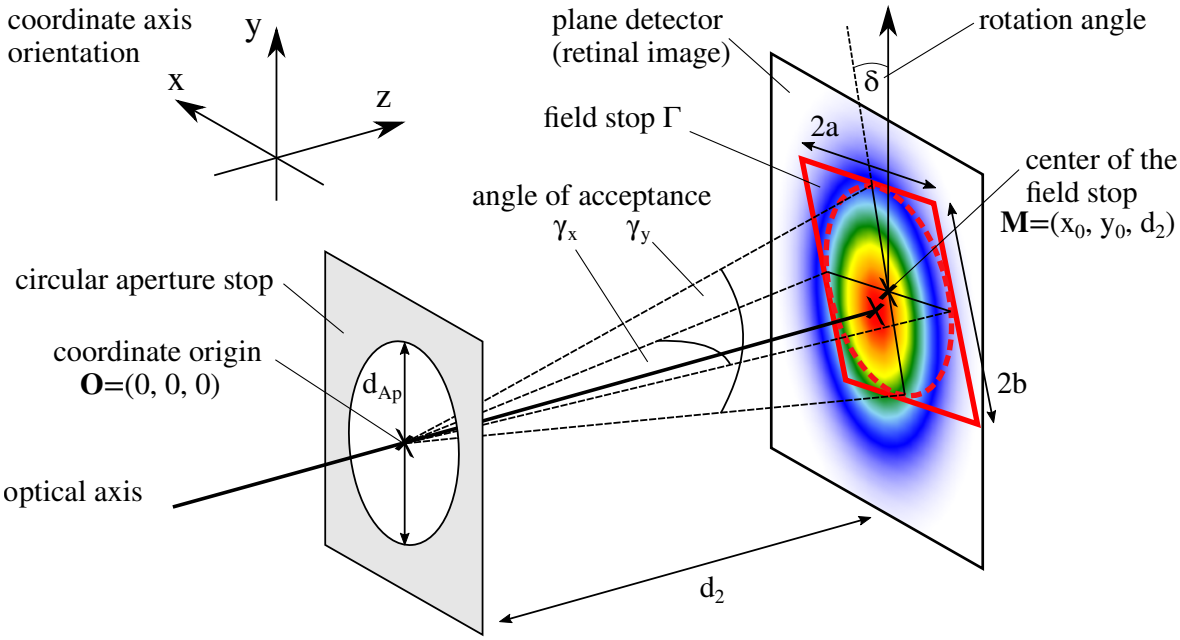

Figure 53: Illustration of the angle of acceptance in x-direction (γ_x) and y-direction (γ_y) for the field stop Γ which is placed in the retinal image. The shape of the field stop is shown as a rectangle (red solid line) and an ellipse (red dashed line) with the half widths a and b and the rotation angle δ. This figure also illustrates the air-equivalent eye model whereas the eye lens is not shown.

quarter rotation. The angle of acceptances in x- and y-direction are calculated by

$$\gamma_x(x_0, y_0, a, b, \delta) = \arccos\left(\frac{x_0^2 + y_0^2 - a^2 + d_2^2}{\sqrt{{d_2}^2 + (x_0 + a\,\cos\delta)^2 + (y_0 - a\,\sin\delta)^2}} \times \frac{1}{\sqrt{{d_2}^2 + (x_0 - a\,\cos\delta)^2 + (y_0 + a\,\sin\delta)^2}}\right), \tag{76}$$

$$\gamma_y(x_0, y_0, a, b, \delta) = \arccos\left(\frac{x_0^2 + y_0^2 - b^2 + d_2^2}{\sqrt{{d_2}^2 + (y_0 + b\,\cos\delta)^2 + (x_0 + b\,\sin\delta)^2}} \times \frac{1}{\sqrt{{d_2}^2 + (y_0 - b\,\cos\delta)^2 + (x_0 - b\,\sin\delta)^2}}\right), \tag{77}$$

where δ represents the direction of rotation from Fig. 53. For determining the angular subtense of the apparent source, the angles in both directions have to be limited according to α_{min} and α_{max} from Table 11 and Table 12. After limiting these angles the average is calculated by

$$\gamma = \frac{\gamma_x^{\text{lim}} + \gamma_y^{\text{lim}}}{2}. \tag{78}$$

This averaged value has to be inserted into the emission limits regarding the thermal,

Table 13: Formulas to calculate the solid angle Ω for different field stops located at the center of the detector plane ($\mathbf{M} = (0, 0, d_2)$) from Fig. 53.

field stop shape	solid angle Ω
square	$4 \arcsin\left(\sin^2 \frac{\gamma}{2}\right)$
rectangle	$\arcsin\left(\sin \frac{\gamma_x}{2} \sin \frac{\gamma_y}{2}\right)$
circle	$4\pi \sin^2 \frac{\gamma}{4}$
ellipse	$2\pi - 4 \int_0^{\frac{\pi}{2}} \frac{1}{\sqrt{1+\frac{\tan^2 \frac{\gamma_x}{2} \tan^2 \frac{\gamma_y}{2}}{\left(\tan \frac{\gamma_x}{2} \sin\varphi\right)^2 + \left(\tan \frac{\gamma_y}{2} \cos\varphi\right)^2}}} \mathrm{d}\varphi$

thermomechanical and photomechanical hazard and therefore into equation (70) for coherent sources and into equation (72) for incoherent sources with α=γ as function argument.

In case of incoherent sources, the radiance has to be evaluated from the retinal image. For this calculation, the solid angle Ω subtended by the angle of acceptance is needed. The solid angle is defined by projecting the field stop from Fig. 53 on the surface of a unit sphere located in the coordinate origin. Depending on the size and shape of the field stop, the corresponding solid angles can be calculated by the equations listed in Table 13.

These Ω calculations refer to a field stop located the center of the retinal image from Fig. 53. For field stops which are located at $\mathbf{M} = (x_0, y_0, d_2)$, the solid angle Ω_M can be determined with the solid angle Ω of the centered field stop by

$$\Omega_M = \frac{\Omega}{\sqrt{\frac{x_0^2+y_0^2}{d_2^2} + 1}}. \tag{79}$$

A3.3.3.3 Field stop Γ_{ph} for photochemical limits

For coherent as well as for incoherent sources, the eye safety evaluation of the photochemical hazard has to be performed for a fixed angle of acceptance γ_{ph}. According to the laser safety standard [IEC, 2014] and the lamp safety standard [IEC, 2006], the field stop Γ_{ph} that is placed within the retina to measure the accessible emission is formed by a right circular cone directed to the retina and having a full opening angle of γ_{ph}. Unlike before, where a field stop is placed in the retina and the corresponding angle of acceptances γ_x and γ_y are evaluated according to equations (76) and (77), the procedure for photochemical limits is the other way round. This can be shown in Fig. 53, where a right circular cone is positioned in the coordinate origin **O** and both angle of acceptances are equal to γ_{ph}. The field stop is defined by an area Γ_{ph} within

the detector plane

$$\Gamma_{\mathrm{ph}}: \ (\gamma_{\mathrm{ph}}) \mapsto \begin{pmatrix} x(\gamma_{\mathrm{ph}}) \\ y(\gamma_{\mathrm{ph}}) \end{pmatrix} \tag{80}$$

and is obtained by the intersection between the plane detector and the surface of the circular cone whereas the axis of the cone is hitting the detector at $(x_{\mathrm{Retina}}, y_{\mathrm{Retina}})$. For a circular cone hitting the detector perpendicular at its center, the field stop is a circle at $\mathbf{M} = (0, 0, d_2)$ with a radius $r = d_2 \tan \frac{\gamma_{\mathrm{ph}}}{2}$. In case of all other intersection points $(x_{\mathrm{Retina}}, y_{\mathrm{Retina}})$ between the cone axis and the detector, the incident angle of the cone changes and the resulting field stop is described by an ellipse. The intersection can be evaluated by rotating the cone around the x-axis with the angle θ_{V} (elevation) and afterwards around the y-axis with the angle θ_{H} (azimuth). Both angles are then defined by

$$\theta_{\mathrm{H}} = \arctan \frac{x_{\mathrm{Retina}}}{d_2}, \tag{81}$$

$$\theta_{\mathrm{V}} = \arctan \left(-\frac{y_{\mathrm{Retina}}}{d_2} \cos \theta_{\mathrm{H}} \right). \tag{82}$$

By intersecting the rotated cone with the plane detector, the field stop is defined by an elliptical curve in the coordinate system of the detector

$$\Gamma_{\mathrm{ph}}: \ \mathbf{C}_{\mathrm{Ell}}(\varphi) = \mathbf{x_0} + K_1 \cos\varphi \, \mathbf{n_1} + K_2 \sin\varphi \, \mathbf{n_2}, \quad 0 \leq \varphi < 2\pi. \tag{83}$$

The center of the ellipse $\mathbf{x_0}$ is given by

$$\mathbf{x_0} = \frac{2 d_2 \cos\theta_{\mathrm{H}} \cos\theta_{\mathrm{V}}}{\cos\gamma + 2\cos^2\theta_{\mathrm{H}} \cos^2\theta_{\mathrm{V}} - 1} \begin{pmatrix} \cos\theta_{\mathrm{V}} \sin\theta_{\mathrm{H}} \\ -\sin\theta_{\mathrm{V}} \end{pmatrix} = \begin{pmatrix} x_0 \\ y_0 \end{pmatrix} \tag{84}$$

and is not equal to the hitting point of the cone axis on the detector. The normalized vectors $\mathbf{n_1}$ and $\mathbf{n_2}$ are evaluated by

$$\mathbf{n_1} = \frac{1}{\sqrt{x_{\mathrm{Retina}}^2 + y_{\mathrm{Retina}}^2}} \begin{pmatrix} x_{\mathrm{Retina}} \\ y_{\mathrm{Retina}} \end{pmatrix}, \tag{85}$$

$$\mathbf{n_2} = \frac{1}{\sqrt{x_{\mathrm{Retina}}^2 + y_{\mathrm{Retina}}^2}} \begin{pmatrix} -y_{\mathrm{Retina}} \\ x_{\mathrm{Retina}} \end{pmatrix} \tag{86}$$

and describe both orthogonal directions of the ellipse. The half length of both directions are given by the scalar values K_1 and K_2. Here, K_1 is the half length of the first axis

$$K_1 = \frac{2 d_2 \cos\frac{\gamma}{2} \sin\frac{\gamma}{2}}{\cos\gamma + 2\cos^2\theta_{\mathrm{H}} \cos^2\theta_{\mathrm{V}} - 1} \tag{87}$$

and K_2 is the half length of the second axis

$$K_2 = \frac{\sqrt{2}d_2 \sin\frac{\gamma}{2}\sqrt{1-\cos\theta_{\mathrm{H}}\cos\theta_{\mathrm{V}}}\sqrt{1+\cos\theta_{\mathrm{H}}\cos\theta_{\mathrm{V}}}}{\sqrt{1-\cos^2\theta_{\mathrm{H}}\cos^2\theta_{\mathrm{V}}}\sqrt{\cos\gamma+2\cos^2\theta_{\mathrm{H}}\cos^2\theta_{\mathrm{V}}-1}}. \tag{88}$$

Alternatively, instead of placing an elliptical field stop into the retinal image it would also be reasonable to use a rectangular shaped field stop like in the procedure from section A3.3.3.2. Here, the rectangle would be located at $\mathbf{x_0}$ and would be having the same orientation according to equation (84) and the same half lengths K_1 and K_2 from equations (87) and (88). This alternative is not provided in both standards, but can safely be used as the rectangular shaped field stop encloses a greater area on the retinal image leading generally to a higher measured accessible emission than for using an elliptical shaped field stop having the same angle of acceptance γ_{ph}.

A3.3.3.4 Radiant power of coherent sources

For coherent sources, the AE has to be generally given in terms of the radiant power Φ which is enclosed by the field stop Γ

$$\Phi(\Gamma) = \int_{\Gamma} E \,\mathrm{d}\Gamma. \tag{89}$$

It is emphasized that there are accessible emission limits which are given in terms of the radiant energy Q. However, as it was mentioned before it is irrelevant for the determination of α to consider the radiant power or radiant energy. The mathematical conversion of the radiant energy into the radiant power is performed by a division of the time t for the accessible emission limits. Therefore this conversion does not affect the dependence on the angular subtense.

A3.3.3.5 Radiance of incoherent sources

In the lamp safety standard [IEC, 2006], the retinal limits for incoherent sources are either expressed by the radiance L or the time-integrated radiance if the photochemical limit for small sources is not taken into account and only the general photochemical limit is considered. The lamp safety standard [IEC, 2006] describes a method where the radiance L can be calculated by the irradiance E with the relation

$$L = \frac{\mathrm{d}E}{\mathrm{d}\Omega}. \tag{90}$$

By assuming a Lambertian source where the radiance does not depend on the solid angle Ω the relation can be simplified to

$$L = \frac{E}{\Omega}. \tag{91}$$

Here, a weighted irradiance is needed and the measured retinal image which is given by the spectral irradiance distribution E'_λ has to be weighted. According to the lamp safety standard, a weighted irradiance E' is evaluated from the retinal image by integrating over a weighting function. The weighted irradiance differs depending on which type of accessible emission limit is considered. In case of the thermal hazard regime, the irradiance is defined by

$$E' = \int_{380\,\mathrm{nm}}^{1400\,\mathrm{nm}} R(\lambda) E'_\lambda \,\mathrm{d}\lambda \tag{92}$$

and in case of the photochemical hazard regime, the irradiance is given by

$$E' = \int_{300\,\mathrm{nm}}^{700\,\mathrm{nm}} B(\lambda) E'_\lambda \,\mathrm{d}\lambda. \tag{93}$$

$R(\lambda)$ is the burn hazard weighting function. In general, this weighting function represents the biological absorption of the radiation. It shows relatively small values for the near-infrared wavelength region as more light is absorbed by the cornea and the lens of the eye in comparison to the visible wavelength region. The burn hazard weighting function shows a maximum at around 440 nm. The function $B(\lambda)$ is referred to as blue light hazard weighting function and also shows a maximum at the same wavelength as for $R(\lambda)$. For higher wavelengths, $B(\lambda)$ decreases and reduces by 10^3 at 600 nm. For lower wavelengths, the function also decreases and reduces by 10^2 at around 380 nm. The blue light hazard function emulates the sensitivity to photochemical hazard as a function of wavelength.

In the next step, an averaged irradiance E is determined by calculating the radiant power enclosed by the field stop Γ placed in the retinal image and dividing by the area of the circular aperture

$$E(\Gamma) = \frac{\int_\Gamma E' \mathrm{d}\Gamma}{\frac{\pi}{4}\left(d_{\mathrm{Ap}}\right)^2}. \tag{94}$$

At last, it has to be taken into account that the field stop Γ subtends a solid angle in which the averaged irradiance $E(\Gamma)$ was determined. By projecting the area of the field stop in the retinal image on the unit sphere, the solid angle $\Omega(\Gamma)$ can be calculated. The solid angle depends on the field stop size, shape and location. The calculation of the solid angle is shown in Table 13.

The radiance is determined by dividing the irradiance by the solid angle

$$L(\Gamma) = \frac{E(\Gamma)}{\Omega(\Gamma)}. \tag{95}$$

The retinal limits in the lamp safety standard are either expressed by the radiance or the time-integrated radiance. Here, the time-integration plays not an important role for the determination of the angular subtense of the apparent source and for defining the evaluation procedure regarding the photochemical limit and will therefore not be considered in detail.

A3.3.4 Retinal Image Analysis

The introduced retinal image analysis is an evaluation procedure that is used for eye safety evaluations of radiation that is imaged on the retina. This procedures is in accordance with the laser safety standard [IEC, 2014] as well as with the lamp safety standard [IEC, 2006] and can be applied both to coherent and incoherent sources. As the image analysis yields the most restrictive result of the eye safety evaluation, it is ensured that there is no underestimation of the hazard.

The basic principle of the analysis is to maximize the ratio between the accessible emission (AE) of the radiation and the corresponding accessible emission limit (AEL). However, as discussed before, there are two different types of retinal AELs, namely the photochemical limits and the limits that depend on the angular subtense of the apparent source α. The image analysis differs depending on which type of limit is considered and in the following both analysis procedures are introduced. Whereas for the photochemical hazard, the main scope of the image analysis is the correct position of the field stop, for the other retinal limits the main issue is the correct determination of the angular subtense of the apparent source.

A3.3.4.1 Angular subtense of the apparent source

In general, radiation imaged on the retina has a lower hazard potential if the radiation extends over a larger retinal area at the same radiant energy. This behavior is considered in the AELs of the safety standards where larger retinal spots increase the limits for coherent sources and decrease the limits expressed in radiance for incoherent sources. In the standards, the retinal image size is given by the angular subtense α and this value defines the limits. However, there is no explicit definition for the angular subtense and generally no beam diameter definitions for the sources or diameter definitions of the retinal images are suitable for determining the angular subtense as the eye safety evaluation could be underestimated. In addition, the AE describes the amount of radiant energy the angular subtense of the apparent source α encloses, and

is therefore also dependent on it. The image analysis is a procedure to determine the angular subtense where it is ensured to obtain the most restrictive eye safety result. We propose the following generalized definition of the image analysis:

$$\left\{ \Gamma(x_0, y_0, a, b, \delta) \middle| \max \frac{\mathrm{AE}\,(\Gamma)}{\kappa\,(\gamma)} \right\} \Bigg|_{\gamma=\alpha\ (\gamma_x=\alpha_x, \gamma_y=\alpha_y)} \tag{96}$$

The value γ refers to the averaged angle of acceptance from equation (78) of the field stop Γ. As a result, the angle of acceptance γ_k for both orthogonal directions of the field stop is varied within

$$\alpha_{\min} \leq \gamma_k \leq \alpha_{\max}. \tag{97}$$

The AEL is given by the function $\kappa(\alpha)$ which represents the α dependence of the limits. For incoherent sources, equation (72) is used for the emission limit κ and equation (95) for the accessible emission. In case of coherent radiation, κ is defined by equation (70) and the accessible emission by equation (89). According to the image analysis in equation (96), all possible field stops Γ have to be considered which means that all parameters x_0, y_0, a, b and δ, see illustration from Fig. 53, that define the field stop have to be varied. As the extents a and b are varied so that the angle of acceptances are within the interval from equation (97), the tilt angle δ has to be varied within

$$0\,\mathrm{deg} \leq \delta < 45\,\mathrm{deg}. \tag{98}$$

The field stop shape can either be rectangular or elliptical. The angle of acceptance γ associated with the field stop that yields the highest ratio between the AE and AEL, is the angular subtense of the apparent source α. The retinal image analysis is illustrated in Fig. 54.

A3.3.4.2 Photochemical analysis

The image analysis for photochemical limits differs in comparison to the analysis for the other limits and is less extensive. The corresponding limits do not depend on a retinal image size and are also independent of the angle of acceptance. Unlike in section A3.3.4.1, where the angle of acceptance γ had to be varied to determine the angular subtense α that yields the most restrictive ratio, the angle of acceptance is a fixed value equal to the photochemical angle of acceptance γ=γ_{ph} which is defined in the safety standards. In section A3.3.3.3 it is described that the field stop Γ_{ph} is a circular cone with an opening angle of γ_{ph} intersecting with the retinal plane. The field stop only defines the AE and the acceptance angle does not affect the AEL. As a result, the image analysis for photochemical limits in case of a field stop Γ_{ph} with a

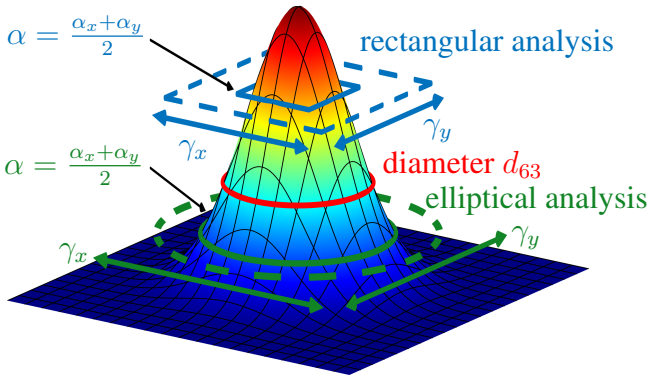

Figure 54: Example of an image analysis for a retinal image with a Gaussian irradiance distribution. The field stops are realized by a rectangle and an ellipse with varying extents given by the angles of acceptance γ_x and γ_y. The dashed green and blue line indicate the variation of the angle of acceptance and therefore the variation of the field stop Γ. The solid lines represent the solution α of the image analysis. In addition, the diameter d_{63} of the Gaussian distribution is shown. The variation of the rotation angle and the location is not depicted.

photochemical angle of acceptance γ_{ph} is defined by

$$\left\{ \Gamma_{\mathrm{ph}}(x_{\mathrm{Retina}}, y_{\mathrm{Retina}}) \middle| \max \mathrm{AE}\left(\Gamma_{\mathrm{ph}}\right) \right\}, \tag{99}$$

where x_{Retina} and y_{Retina} is the intersection point between the cone axis and the retinal plane. As a result, image analysis requires varying the intersection point for a given angle of acceptance to find the position that encloses the most radiant energy within the field stop.

A3.3.4.3 Radial symmetric retinal images

For radial symmetric retinal images, the irradiance distribution can be expressed in polar coordinates

$$E_{\mathrm{RI}}\left(r, \varphi\right) = E_{\mathrm{RI}}\left(r\right). \tag{100}$$

In the following it is assumed that the irradiance is monotonously decreasing for a higher radius r. As a consequence, the most restrictive field stop Γ has to be located at $r = 0$ and there is no need to vary the position and the orientation. The field stop has either a square or a circular shape with the half length or radius a. This size is determined by the angle of acceptance γ with

$$a = d_2 \tan \frac{\gamma}{2}. \tag{101}$$

In case of a square aperture the radiant power within the field stop is calculated by

$$\Phi^{\mathrm{S}}(\gamma) = 8 \int_0^{\frac{\pi}{4}} \int_0^{\sqrt{1+\tan^2\varphi}\, d_2 \tan\frac{\gamma}{2}} E_{\mathrm{RI}}(r) r \,\mathrm{d}r \,\mathrm{d}\varphi \tag{102}$$

and in case of a circular aperture by

$$\Phi^{\mathrm{C}}(\gamma) = 2\pi \int_0^{d_2 \tan\frac{\gamma}{2}} E_{\mathrm{RI}}(r) r \,\mathrm{d}r. \tag{103}$$

For incoherent sources the radiance is needed and equation (95) can be transformed to

$$L^{\mathrm{S}}(\gamma) = \frac{\Phi^{\mathrm{S}}(\gamma)}{\pi d_{\mathrm{Ap}}^2 \arcsin\left(\sin^2\frac{\gamma}{2}\right)} \approx \frac{\Phi^{\mathrm{S}}(\gamma)}{\frac{\pi}{4} d_{\mathrm{Ap}}^2 \gamma^2} \tag{104}$$

and

$$L^{\mathrm{C}}(\gamma) = \frac{\Phi^{\mathrm{C}}(\gamma)}{\pi^2 d_{\mathrm{Ap}}^2 \sin^2\frac{\gamma}{4}} \approx \frac{\Phi^{\mathrm{C}}(\gamma)}{\left(\frac{\pi}{4}\right)^2 d_{\mathrm{Ap}}^2 \gamma^2} \tag{105}$$

respectively. For small angles, both equations (104) and (105) can be approximated by the term on the right side. This approximation can be applied as the angle of acceptance is in the mrad regime. Since the angle of acceptance is limited by $\alpha_{\max}$, the deviation caused by the paraxial approximation is less than about 0.1 %. By inserting the radiance approximation and the κ behavior from equation (72) into the image analysis from equation (96), it can be seen that the same ratio has to be maximized as for coherent sources with emission durations shorter than T_2. For incoherent sources, the same image analyis is applied as for coherent sources with short emission durations.

In case of radial symmetric retinal images having a global irradiance maximum at $r = 0$, the complexity of the image analysis reduces. For the determination of the angular subtense α, see equation (96), only one parameter, namely the half length of the square field stop or the radius of the circular field stop, has to be varied. In the case of photochemical image analysis, no parameter needs to be varied. Here, the field stop to determine the AE is located in the center of the image and has a fixed size.

A3.4 Results

In this section, the developed image analysis procedure is applied to exemplary optical systems or retinal images, respectively, and relevant conclusions are made. Here, coherent and incoherent systems are considered separately regarding the determination of the angular subtense of the apparent source, since the requirements of the corresponding safety standards turn out differently which lead to a different behavior. It is started with the determination of the angular subtense of coherent radiation. Using

various examples, the application of retinal image analysis is demonstrated and it is shown what has to be taken into account and what the results mean. In the following section, the determination of the angular subtense for incoherent radiation is discussed. Here, it is presented how our developed method improves the current definitions in the lamp safety standard. Finally, the image analysis procedure is used to perform an eye safety evaluation for photochemical limits.

A3.4.1 Angular Subtense of Coherent Sources

In comparison to the standard for incoherent radiation [IEC, 2006], the standard for coherent radiation [IEC, 2014] shows far more complex correlations regarding the determination of the angular subtense of the apparent source. Here, the accessible emissions limits show three different dependencies on the angular subtense which are listed in equation (70). Furthermore, the limitations for the angular subtense follow different equations depending on the emission duration of the radiation and on the measurement condition. The different dependencies are listed in Table 11 and Table 12. In the following, four different exemplary retinal images are presented to illustrate the complexity of the angular subtense of the apparent source for coherent radiation. It is assumed that the retinal images are generated by the air-equivalent eye model where the distance between the lens and the retina is d_2=17 mm.

A3.4.1.1 Field stop shape and limit behavior

In this section, a radial symmetric Gaussian irradiance distribution defined by

$$E_{\mathrm{sym}}^{\mathrm{G}}(r) = \exp\left(-2\frac{r^2}{w^2}\right) = \exp\left(-8\frac{r^2}{d_{86}^2}\right) \tag{106}$$

will be analysed as retinal image. The width w refers to the $1/e$ definition of the distribution and is varied in this investigation. The formula can be rewritten with the corresponding d_{86}-diameter which is twice the size of the width w. The emission duration is assumed to be larger than 0.25 s which lead to a maximum limitation of $\alpha_{\max}$=100 mrad for the angular subtense. The Gaussian retinal image is analysed with a square and a circular field stop where the equations (102) and (103) are used to determine the enclosed radiant power. The calculated radiant power within the field stop Γ is the AE from the image analysis in equation (96). All three different behaviors of the emission limit κ^{C} are considered. Depending on the emission limits, the image analysis can yield different results. For a clear distinction between the cases of the κ^{C} from equation (70), the application of the image analysis using the first case will be referred to as short-time, the second as long-time and the third as long-time-

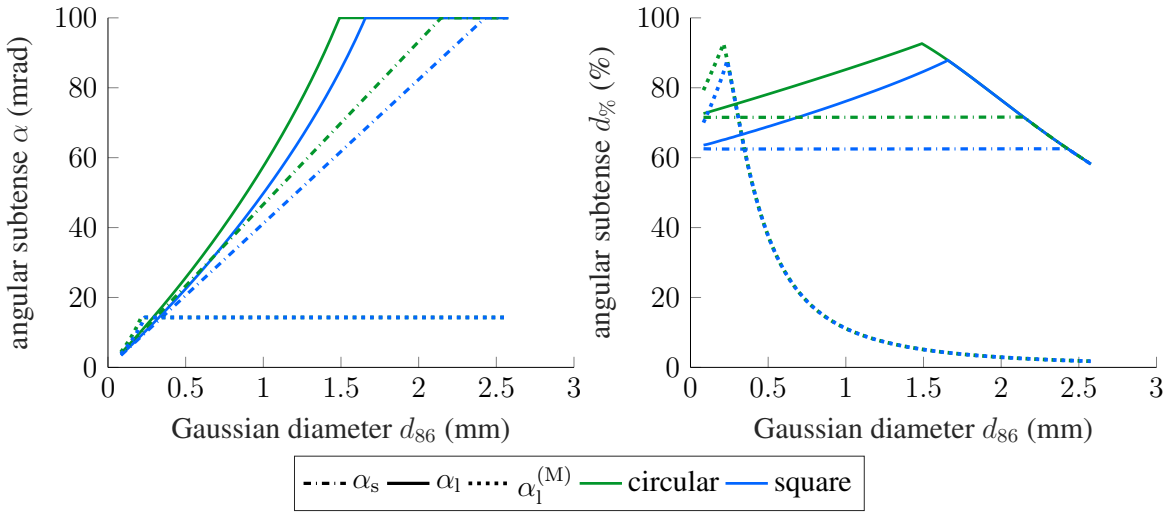

Figure 55: The results of the retinal image analysis for a radial symmetric Gaussian irradiance distributions differ for the short-time, long-time and long-time-magnifying method (α_s, α_l and $\alpha_l^{(M)}$) as well as for the choice of the field stop (circular and square). The x-axis shows different extents of the Gaussian distribution defined by the d_{86}-diameter. In the left plot the y-axis shows the angular subtense α and in the right plot the angular subtense is expressed as $d_{\%}$-diameter.

magnifying method. The results for the angular subtenses are shown in Fig. 55 for both field stop shapes and all analysis methods. The kink of all curves arises from the maximum limitation of the angular subtense to 100 mrad. The kink in the curve for $\alpha_l^{(M)}$ appears significantly earlier than for the other methods. The reason is the reduction of α_{max} by a factor of 7. For the symmetric Gaussian irradiance distribution, the choice of a square field stop leads to a smaller angular subtense than for using a circular field stop. In addition, in regions where the angular subtense is not limited by its maximum and minimum value the results are generally smaller using the short-time method. Furthermore, the long-time-magnifying method shows the largest results before reaching the maximum limitation. This can clearly be seen in the left plot of Fig. 55.

The investigation also shows that the angular subtense does not follow a specific beam diameter definition. This can be seen in the right plot of Fig. 55 where the angular subtense is recalculated as $d_{\%}$-diameter and shows a varying behavior. The only exception is the short-time method where the angular subtense remains approximately constant for an increasing width of the distribution. In case of the square field stop, the angular subtense can be defined by the $d_{62.5}$-diameter and in case of the circular field stop by the $d_{71.5}$-diameter. In the special case of a Gaussian distribution, the d_{63}-diameter can be used for the calculation of the angular subtense according to the laser safety standard. Here, in contrast to the image analysis, the total radiation power

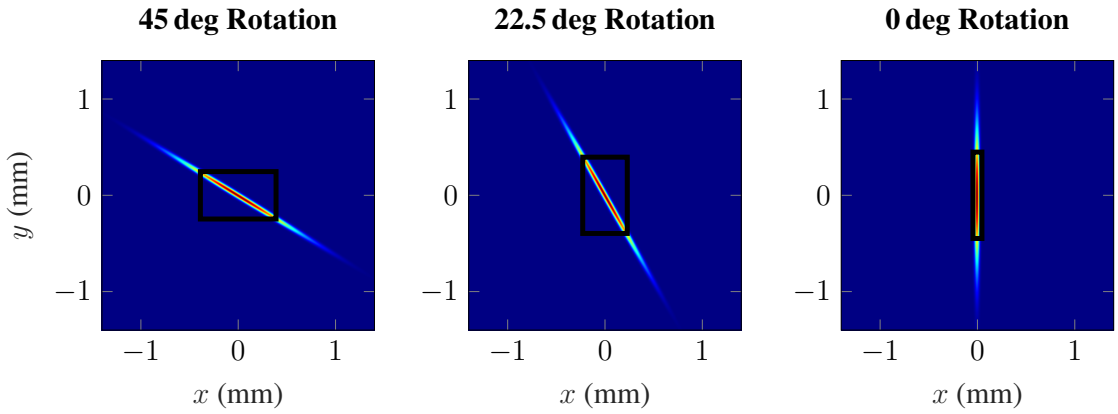

Figure 56: Plots of the elliptical Gaussian distribution for three different tilt angles (Left: 45 deg, Center: 22.5 deg, Right: 0 deg). The image analysis is performed using the long-time method and a rectangular shaped field stop. The angular subtenses are depicted by the black rectangles. The results are listed in Table 14.

is assumed to be contained within this diameter leading to a more restrictive eye safety evaluation [Kotzur et al., 2021b].

A3.4.1.2 Rotation of the field stop

For applying the image analysis according to equation (96) on an arbitrary non-uniform irradiance distribution, all possible field stops Γ have to be taken into account to maximize the ratio between the AE and AEL. When the shape of the field stop is defined to either be rectangular or elliptical, the parameters to be varied are the widths, the position and the rotation angle of the field stop. In general, measured retinal images are two-dimensional matrices and not necessarily aligned along the axial directions of a camera detector. By including the rotation of the field stop, it is ensured to obtain the most restrictive result of the image analysis as all directions of the field stop are taken into account. The rotation can be realized by two different procedures. One option is to rotate the field stop and place it within the retinal image to evaluate the AE for the corresponding angle of acceptance according to equations (76) and (77). The other option is to rotate the retinal image in fixed rotation angle steps to create separate two-dimensional retinal images to which the aligned field stops are applied. In the following example, this procedure is used to illustrate the effect of the field stop rotation. Here, the retinal image is a tilted elliptical Gaussian irradiance distribution which can be seen in the left plot of Fig. 56. The $1/e$-widths of the distribution are w_x=25 μm and w_y=700 μm and the tilt angle is 45 deg. Fig. 56 shows three retinal images for different tilt angles. For each image, the angular subtense is determined by using a rectangular shaped field stop and the long-time method where the limit behavior of the middle case from equation (70) applies. The results are listed in Table 14. In Fig. 56, it is clearly

Table 14: Results of the image analysis for the retinal images from Fig. 56 with different tilt angles.

Angular subtense \ Rotation angle	45 deg	22.5 deg	0 deg
α_x (mrad)	45.73	26.91	5.44
α_y (mrad)	28.97	46.61	52.78
α (mrad)	37.35	36.76	29.11

visible that the angular subtenses α_x and α_y change significantly from left to right. The angular subtense α which is the mean value of α_x and α_y decreases and reaches a minimum for the aligned retinal image in the right plot of Fig. 56. The angular subtense decreases about 5.6 % from a tilt angle of 45 deg to 0 deg. This means that applying the image analysis on an incorrectly aligned retinal image could lead to an underestimation of the eye safety evaluation. In this example, when assuming a static beam irradiating the eye for long emission durations, the maximum permitted power for laser class 1 is increased by 22.3 % if the 45 deg tilted elliptical distribution would be analysed instead of the aligned distribution. It is emphasized, that the rotation of the field stops does not only have to be performed on coherent radiation but also on incoherent radiation.

A3.4.1.3 Emission duration and limitation of the angle of acceptance

In the laser safety standard [IEC, 2014], the maximum limitation of the angle of acceptance depends on the emission duration. This dependence is listed in Table 11 in the equation for the maximum angular subtense $\alpha_{\max}$. Furthermore, the emission duration also affects the dependence of the AEL on the angular subtense according to equation (70). As the magnifying measurement condition will not be considered here, either the short-time or the long-time method is applied for the image analysis. In this example, a Hermite-Gaussian source [Saleh and Teich, 2007] with the order (1,2) and the $1/e^2$ waist radius 8 mm is considered and placed directly in front of the air-equivalent eye model. The retinal image is generated by solving the wave optical diffraction equation [Goodman, 2005] for the propagation through the eye with a focal length of f=14.53 mm.

The retinal image can be seen in Fig. 57 together with the results of the image analysis for four different emission durations using rectangular shaped field stops. The detailed results for the image analysis of Fig. 57 are listed in Table 15. As the maximum limitation $\alpha_{\max}$ is increasing for higher emission durations, the angular subtense of the apparent source can also have higher values. In this example, the angular subtense is equal to the maximum limitation in case of the first emission duration. For a higher

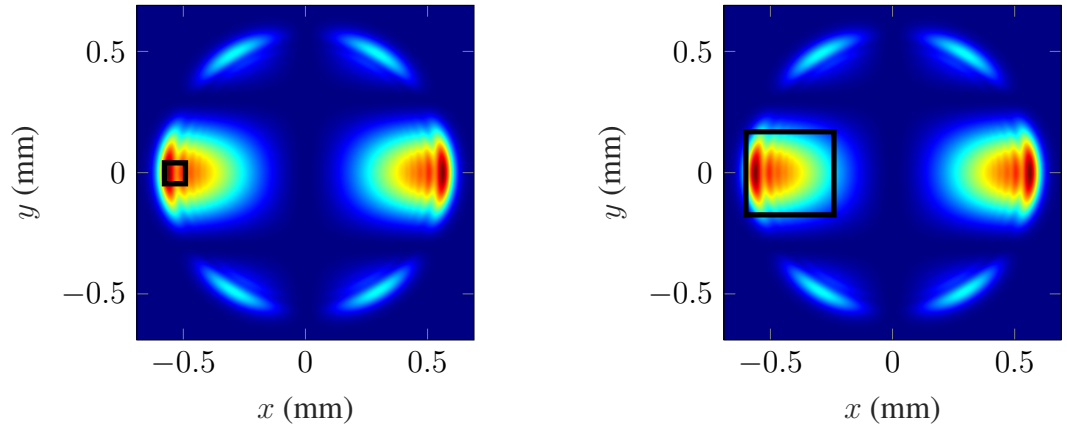

(a) Short-time method with $t \leq 625\,\mu$s.

(b) Short-time method with $t = 0.1$ s.

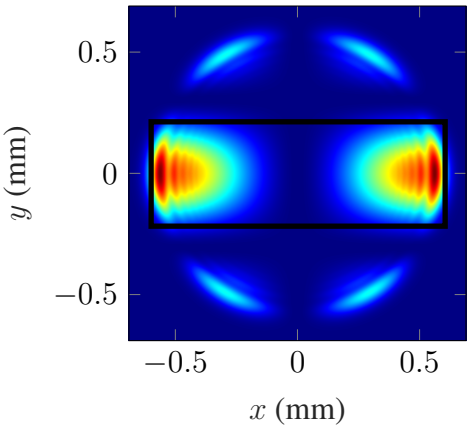

(c) Short-time method with $t > 0.25$ s.

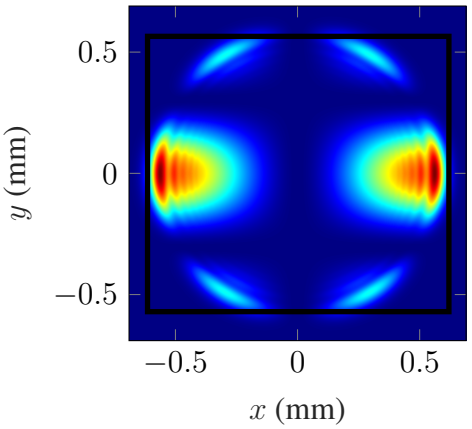

(d) Long-time method with $t > T_2$.

Figure 57: In all plots, the angular subtense of the apparent source is determined for the same retinal image. Depending on the emission duration t of the radiation, the maximum limitation $\alpha_{\max}$ changes and either the short or long-time method is used. In (a)-(c) the emission duration is $t \leq 625\,\mu$s, $t = 0.1$ s and $t > 0.25$ s and the short method is used. In (d) the emission duration is $t > T_2$ and the long-time method is used. The results of the image analysis are listed in Table 15.

$\alpha_{\max}$, the angular subtense can enclose the left peak irradiance, see Fig. 57(b), and also both the left and right peak irradiance, see Fig. 57(c). There is also a difference in the angular subtense when comparing the results for the third and fourth emission duration. In both cases the maximum limitations are identical but a different method is used. For the long-time method, the angular subtense encloses almost the complete retinal image, see Fig. 57(d).

This analysis shows that there is no specific angular subtense of the apparent source when performing an eye safety evaluation for a laser source as there is a dependence on the emission duration of the radiation. Furthermore, the angular subtense is not a characteristic of the laser source but is determined by analysing the retinal image

Table 15: Results of the image analysis for the retinal image from Fig. 57 for different emission durations t. Also, the maximum limitation $\alpha_{\max}$ is shown for the corresponding emission duration. The results show the location (x_0, y_0) and size (expressed by the angular subtense α_x and α_y) of the rectangular shaped field stop.

Result \ Emission duration	$t \leq 625\,\mu$s short	$t = 0.1\,$s short	$t > 0.25\,$s short	$t > T_2$ long
$\alpha_{\max}$ (mrad)	5	63.25	100	100
x_0 (μm)	-534.26	-420.17	0	0
y_0 (μm)	0	0	0	0
α_x (mrad)	5	21.22	70.78	72.55
α_y (mrad)	5	20.17	25.32	66.77
α (mrad)	5	20.70	48.05	69.66

created by the source. As a result, for a complete eye safety evaluation, all possible focal lengths of the eye model have to be considered for the most restrictive result.

A3.4.1.4 Multiple wavelengths

For optical systems emitting coherent radiation at several wavelengths, a few additional steps have to be taken into account to perform the retinal image analysis. The prerequisite for this is that the retinal image should be measured in terms of the spectral irradiance distribution E'_λ like in case of incoherent sources. Biologically, different wavelengths in the visible and near-infrared region show a different transmittance behavior when propagating through the eye. Especially in the near-infrared region, the amount of radiant energy that reaches the retina can be significantly reduced. This behavior is also reflected in the laser safety standard [IEC, 2014] by increasing the accessible emission limit with the correction factors $C_4(\lambda)$ and $C_7(\lambda)$. In the following, the definitions for both correction factors are extended which enables to use a generalised accessible emission limit:

$$C_4(\lambda) = \begin{cases} 1, & \text{if } \lambda \in [400\,\text{nm}, 700\,\text{nm}) \\ 10^{\frac{0.002}{\text{nm}}(\lambda - 700\,\text{nm})}, & \text{if } \lambda \in [700\,\text{nm}, 1050\,\text{nm}) \\ 5, & \text{if } \lambda \in [1050\,\text{nm}, 1400\,\text{nm}) \end{cases}, \tag{107}$$

$$C_7(\lambda) = \begin{cases} 1, & \text{if } \lambda \in [400\,\text{nm}, 1150\,\text{nm}) \\ 10^{\frac{0.018}{\text{nm}}(\lambda - 1150\,\text{nm})}, & \text{if } \lambda \in [1150\,\text{nm}, 1200\,\text{nm}) \\ 8 + 10^{\frac{0.04}{\text{nm}}(\lambda - 1250\,\text{nm})}, & \text{if } \lambda \in [1150\,\text{nm}, 1400\,\text{nm}) \end{cases}. \tag{108}$$

The laser safety standard provides limits that depend on the emission duration and on the wavelength of the radiation whereas either the correction factor C_4 or C_7 is

Table 16: Overview of the source characteristics used in the exemplary retinal image in Fig. 58. The sources are created by an elliptical Gaussian irradiance distribution.

Source	Wavelength	Center $x_0^{\mathrm{Ell,G}}/y_0^{\mathrm{Ell,G}}$ (mm)	Width w_x/w_y (mm)	Peak irradiance A ( )
1	λ_1	-0.65 / 0.65	0.2 / 0.2	0.3
2	λ_1	0.65 / 0.65	0.2 / 0.2	0.3
3	λ_2	0 / 0	1 / 0.3	1
4	λ_3	-0.65 / -0.65	0.2 / 0.2	0.3
5	λ_3	0.65 / -0.65	0.2 / 0.2	0.3

used. To simplify the evaluation of sources operating at multiple wavelengths, it is advantageous to use a general limit where both correction factors always occur. With this requirement and together with the above equations (107) and (108), all retinal limits for extended sources can be transformed to have the following dependence:

$$\kappa_\lambda^{\mathrm{C}}(\alpha) = C_4(\lambda)C_7(\lambda)\kappa^{\mathrm{C}}(\alpha) \tag{109}$$

In case of multiple wavelengths, the laser safety standard states that the sum of ratios between the accessible emission AE_λ and the corresponding AELs have to be taken into account. The summation is realized by an integration over the wavelength and only the parameter dependencies of the limits are considered. With a specific field stop Γ, this results in the following term

$$\int_\lambda \frac{\mathrm{AE}_\lambda(\Gamma)}{\kappa_\lambda^{\mathrm{C}}(\gamma)}\,\mathrm{d}\lambda = \int_\Gamma \frac{1}{\kappa^{\mathrm{C}}(\gamma)} \int_\lambda \frac{E'_\lambda}{C_4(\lambda)C_7(\lambda)}\,\mathrm{d}\lambda\,\mathrm{d}\Gamma = \frac{\int_\Gamma E(\Gamma)\,\mathrm{d}\Gamma}{\kappa^{\mathrm{C}}(\gamma)} = \frac{\mathrm{AE}(\Gamma)}{\kappa^{\mathrm{C}}(\gamma)}. \tag{110}$$

Here, the weighted irradiance distribution E is used which is obtained by integrating over the spectral irradiance E_λ divided by the correction factors

$$E = \int_\lambda \frac{E_\lambda}{C_4(\lambda)C_7(\lambda)}\,\mathrm{d}\lambda. \tag{111}$$

This relation can be inserted into the image analysis described in equation (96) to determine the angular subtense of the apparent source.

To illustrate the importance of the correct application of the image analysis, an exemplary retinal image is investigated consisting of five elliptical Gaussian irradiance distributions with the parameters listed in Table 16. The Gaussian distribution is defined by

$$E_{\mathrm{Ell}}^{\mathrm{G}}(x,y) = A\exp\left(-\frac{(x-x_0^{\mathrm{Ell,G}})^2}{w_x^2} - \frac{(y-y_0^{\mathrm{Ell,G}})^2}{w_y^2}\right). \tag{112}$$

Both widths w_x and w_y refer to the $1/e$-definition. The peak irradiance A is given in arbitrary units as the relative radiant energies between the sources are relevant for

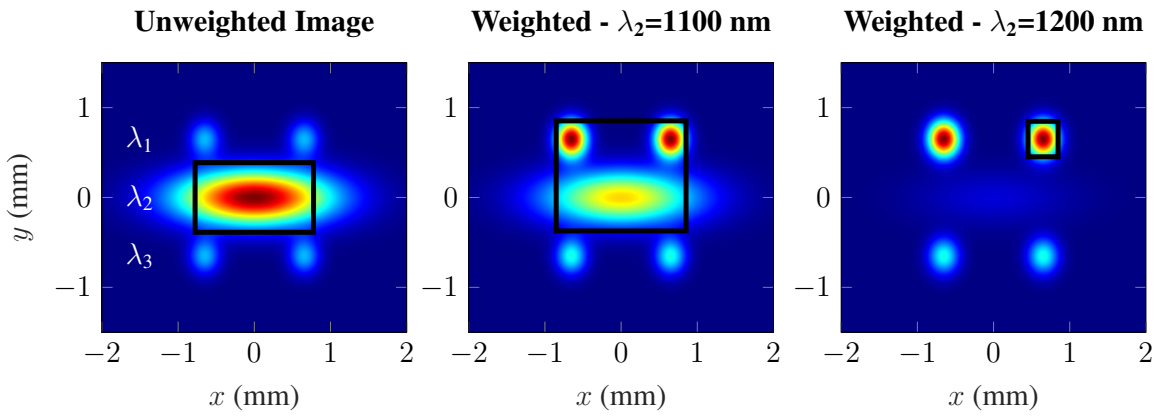

Figure 58: Left: Retinal image showing the measured irradiance distribution for the example with the wavelengths λ_1=400 nm, λ_2 and λ_3=900 nm. There are two sources for both the wavelength λ_1 and λ_2. The source with the wavelength λ_2 shows a higher irradiance peak than for the other sources. The results of the image analysis is depicted by the black rectangles and are listed in Table 16. Center: The weighted retinal image is shown for λ_2=1100 nm. The angular subtense now encloses both the center source and both upper sources. Right: Weighted retinal image for λ_2=1200 nm. By weighting with the relatively high correction factor $C_7(\lambda_2)$, the center source is barely visible and the angular subtense encloses a single λ_1-source.

the image analysis and not the absolute radiant energy. Fig. 58 shows the exemplary retinal image. Table 17 lists the results of the image analysis. The sources 1 and 2 have a wavelength of λ_1=400 nm and can be seen as two symmetric spots in the upper half of the retinal images in Fig. 58. The sources 4 and 5 which are also symmetric are located in the lower half of the retinal image and have the wavelength λ_3=900 nm. The source in the center of the retinal images shows an elliptical shape of the Gaussian distribution and two different wavelengths for λ_2, 1100 nm and 1200 nm, are considered. In the left plot in Fig. 58, the unweighted retinal image can be seen which represents the irradiance distribution measured by a plane detector. The source in the center of the image has the highest peak irradiance regardless of the wavelength λ_2. In the center and right plot, each of the irradiance distribution of the single sources are weighted with the correction factors and then summed up according to the relation in equation (111). For the sources 1 and 2, both correction factors are equal to one and the weighting does not change the irradiance levels. In case of the sources 4 and 5 which have the wavelength 900 nm, the C_7 factor is equal to one and the C_4 factor increases by 2.5. This results in a lower weighted irradiance for the lower two sources in the center and right plot of Fig. 58 compared to the upper two sources. The weighting of source 3 is different for both wavelengths. Here, in both cases the factor C_4 is equal to 5 but the factor C_7 increases from 5 to about 40 when increasing the wavelength from 1100 nm

Table 17: Result of the retinal image analysis for the three retinal images from Fig. 58 which are weighted differently. The results show the location (x_0, y_0) and size (expressed by the angular subtense α_x and α_y) of the rectangular shaped field stop.

Result \ Retinal Image	Unweighted	Weighted λ_2=1100 nm	Weighted λ_2=1200 nm
x_0 (μm)	0	0	650
y_0 (μm)	0	240	650
α_x (mrad)	91.41	100	23.23
α_y (mrad)	45.58	72.03	23.23
α (mrad)	68.49	86.01	23.23

to 1200 nm. This results in an irradiance level comparable to the upper two sources in the center plot of Fig. 58 and in a barely visible source 3 in the right plot. Applying the image analysis on all three retinal images using a rectangular shaped field stop leads to three significantly different angular subtenses which are listed in Table 17. For the unweighted retinal image, the angular subtense encloses the center source 3 and has a value of about 68 mrad. As this evaluation does not take the weighting and summation according to the laser safety standard into account, this result represent an incorrect eye safety evaluation. The correct results are depicted in the center and right plot in Fig. 58 by the black rectangles. For source 3 having a wavelength of 1100 nm, the angular subtense encloses the upper two sources and the center source and has a value of 86 mrad. The weighted irradiance of source 3 lowers for the wavelength of 1200 nm so that the angular subtense only encloses one single source with the wavelength 400 nm and has a value of 23 mrad. In the right plot of Fig. 58, the black rectangle is only drawn in source 2. However, another correct solution would be an angular subtense enclosing source 1 as the same result is obtained.

This example shows the importance of the correct application of the image analysis. Using only an unweighted irradiance distribution would result in a significantly different angular subtense. For analysing retinal images consisting of multiple wavelengths, a weighting according to equation (111) with the correction factors from equation (107) and (108) has to be done.

A3.4.2 Angular subtense of Incoherent Sources

The determination of the angular subtense does not show a broad variability of calculation methods as it was the case for coherent sources. There is one single AEL that depends on the angular subtense which is described by the behavior in equation (72) and the maximum limitation $\alpha_{\max}$ is a fixed value and does not depend on the emission duration. A further difference is that the lamp safety standard [IEC, 2006] introduces

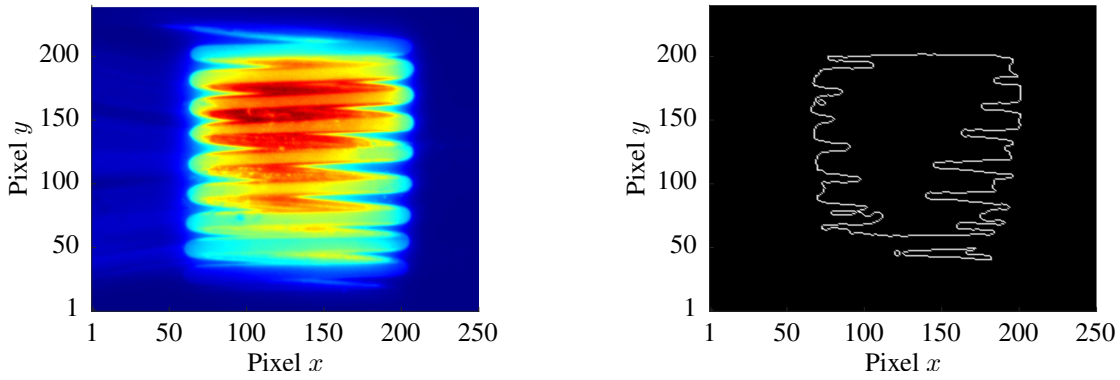

(a) Retinal irradiance distribution in arbitrary units. The retinal image was created by accommodation to the filament.

(b) The white curve shows the 50% emission points of the retinal irradiance distribution. This divides the source into several parts.

Figure 59: Measurement of the retinal image of a halogen lamp (a) and image analysis procedure according to the lamp safety standard (b) [IEC, 2006].

an explicit definition for the angular subtense of the apparent source. Here, the angular subtense is determined by the 50% emission points of the retinal image. However, depending on the retinal image, this determination may not be well defined. Fig. 59 shows a retinal image of a halogen lamp where the 50% criterion is applied. The figure shows the retinal image, measured in irradiance, for accommodation to the filament of the halogen lamp. This accommodation represents a restrictive condition. It can clearly be seen that the criterion from the lamp standard would create several separate source elements. The large source element in the center of Fig. 59 shows an angular subtense with α_x=16.4 mrad, α_y=18.1 mrad and α=17.3 mrad. Below this source there is a smaller elongated source with the angular subtense α_x=7.4 mrad, α_y=1.5 mrad and α=4.4 mrad. According to the lamp safety standard, the hazard evaluation would have to be done for each element and for the combination of the elements. This contradicts to an intuitive approach where the halogen lamp is seen as a single source.

To avoid misunderstandings and to provide one single conservative result, we propose a general definition of the angular subtense with the retinal image analysis from equation (96). The example of the halogen lamp from Fig. 59 is analysed with the retinal image analysis using rectangular shaped field stops which can be seen in Fig. 60. The pixel size of the camera detector is 4.54 μm and the distance d_2 between the eye lens and the detector plane is set to 35 mm. With these settings the solution of the retinal image analysis lead to α_x = 18.1 mrad, α_y = 22.2 mrad and α = 20.2 mrad. This evaluation yields more restrictive results than the procedure described in the lamp safety standard and the deviation between both methods is about 2.7 %. The retinal image analysis for incoherent sources is comparable to the short-time method for coherent sources. The radiance L divided by the AEL yields the same ratio as the

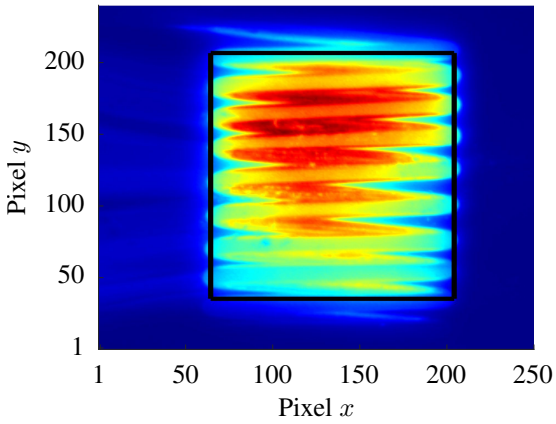

Figure 60: Application of the image analysis to determine the angular subtense of the apparent source with the use of rectangular field stops on the retinal image from Fig. 59.

radiant power Φ divided by the AEL for emission durations shorter than T_2 which is the upper case in equation (70).

A3.4.3 Photochemical Limits

In the previous sections, the eye safety evaluation was performed using retinal limits that depend on the angular subtense of the apparent source. For coherent and incoherent radiation with wavelengths in the photochemical hazard region, see Table 11 and Table 12, a further image analysis has to be applied. For analysing retinal images with regard to the photochemical limits, a rectangular or elliptical shaped field stop, which size is defined by the photochemical angle of acceptance γ_{ph}, has to be placed within the retinal images to maximize the AE. According to the photochemical image analysis from equation (99), the maximization is performed by varying the position x_{Retina} and y_{Retina} of the field stop. In the following, an exemplary retinal image will be considered which is shown in Fig. 61. The retinal image shows a grid consisting of several elongated Gaussian distributions as well as several symmetric Gaussian distributions in the gaps of the grid. The pixel size of the retinal image is 5 μm and the distance d_2 between the eye lens and retina is assumed to be 17 mm. The image analysis is performed for three different photochemical angle of acceptances γ_{ph}, 20 mrad, 40 mrad and 100 mrad. The corresponding results using both possible field stop shapes are listed in Table 18. In the left and center plot of Fig. 61, it can be seen that both possible field stops do not necessarily have to be located at the same position of the retina to maximize the AE. At an angle of acceptance of 20 mrad, the elliptical field stop is not large enough to enclose more than one peak irradiance while two peak irradiances are included in the rectangular field stop. In the right plot of Fig. 61, both field stops are placed in

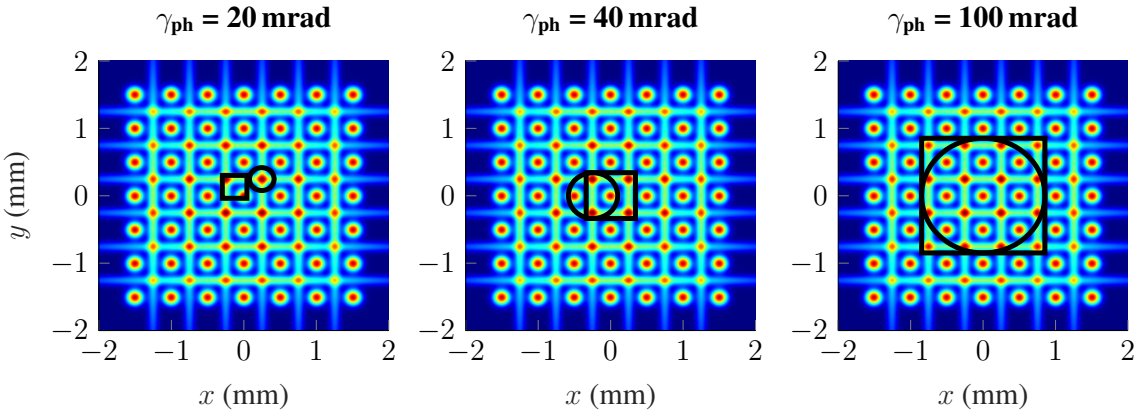

Figure 61: Result of the photochemical image analysis using a rectangular as well as an elliptical field stop for an exemplary retinal image in case of an angle of acceptance γ_{ph} of 20 mrad (left), 40 mrad (center) and 100 mrad (right). The results are depicted by the black field stops and the corresponding characteristics are listed in Table 18.

Table 18: Overview of the results of the photochemical image analysis of the exemplary retinal image from Fig. 61. The results show the position x_{Retina} and y_{Retina} of the field stop Γ_{ph} and the AE. A rectangular as well as an elliptical shape of the field stop was used.

Result \ Angle of acceptance	20 mrad	40 mrad	100 mrad
Rectangular field stop			
x_{Retina} (μm)	-130	0	0
y_{Retina} (μm)	130	0	0
AE(Γ_{ph}) (W)	2.26	8.54	47.25
Elliptical field stop			
x_{Retina} (μm)	245	-240	0
y_{Retina} (μm)	245	0	0
AE(Γ_{ph}) (W)	1.80	6.57	37.50

the center of the retinal image. Here, the rectangular field stop contains more radiant power than the elliptical one. In the above example, the measured AE is by average about 27 % higher when the rectangular shaped field stop is used which lead to a more conservative eye safety evaluation.

At last, it should be noted that in this example the used field stops can be approximated by a circle and a square which size is evaluated using equation (101). In this exemplary investigation, the deviation between an approximated circle or square and an elliptical or rectangular geometry described by equation (83) is less than 0.1 %.

A3.5 Conclusion

In this investigation, a generalized image analysis is introduced for performing eye safety evaluations of radiation in the visible and near-infrared wavelength region, The developed image analysis is in accordance to the laser safety standard IEC 60825-1:2014 [IEC, 2014] and the lamp safety standard IEC 62471:2006 [IEC, 2006] and can therefore be applied to coherent as well as to incoherent radiation. In general, two types of accessible emission limits are identified, namely limits that depend on the angular subtense of the apparent source α and the photochemical limits. For each type of limit, a separate image analysis is applied for the eye safety evaluation. The basic principle of the image analysis is to maximize the ratio between the accessible emission and the accessible emission limit.

In the laser safety standard, the limits that depend on the angular subtense represent the photomechanical, thermomechanical and thermal damage regime. For incoherent radiation, the lamp safety standard provides only one limit that depend on the angular subtense and which represent the thermal hazard. In both cases, the angular subtense describes an area within the retinal image and lead to an increase of the accessible emission limit. Therefore, the angular subtense of the apparent source is an important characteristics of the laser safety standard and lamp safety standard. However, only the lamp safety standard provides an explicit definition of the angular subtense which can lead to ambiguous results. The angular subtense does not follow a specific beam diameter definition and for this reason, a new image analysis is introduced which determines the angular subtense of the apparent source and yields the most restrictive eye safety result.

With the investigated retinal images, it is shown that there is no specific angular subtense for a certain optical system but it is a characteristic value of the retinal image. In case of coherent radiation, the determination of the angular subtense is far more complex than for incoherent radiation. It is shown, that there can be several angular subtenses for the same retinal image. Due to different dependencies of the accessible emission limits, there are three different analysis methods to obtain the angular subtense of the apparent source which are referred to as short-time, long-time and long-time-magnifying method. In the investigated retinal image, the short-time method lead to the smallest α results whereas the long-time-magnifying method yields the largest results. As two different field stop shapes, either rectangular or elliptical, can be applied, a retinal image can have up to six different angular subtenses. The angular subtense of the apparent source also depends on the emission duration of the radiation as it defines the maximum limitation according to the laser safety standard. Therefore, in case of coherent radiation the angular subtense can be limited between 5 mrad and

100 mrad whereas for incoherent radiation the maximum limitation is fixed at 100 mrad. This means that the temporal behavior of the coherent radiation also influences the angular subtense. A further influence is the choice of the field stop shape where either a rectangular or an elliptical shape can be used. As the interaction between the radiation and the tissue behave in an isotropic way the use of an elliptical shape is more justified than for a rectangular shape from a biological point of view. However, the realization of a rectangular field stop is more simple as the measured quantities are often sampled equidistantly. The investigation on the symmetric Gaussian irradiance distribution indicates that the use of a rectangular field stop leads to smaller angular subtenses than for the elliptical field stop and to more restrictive eye safety evaluations. For this reason, the use of a rectangular field stop can be justified and offers a good alternative to elliptical field stops. The image analysis for determining the angular subtense is an extensive procedure where the field stop has to be varied in its size, position and even tilt angle. The importance of the tilt angle is also shown in this investigation where it was found that the eye safety evaluation would be underestimated by about 22 % for an elliptical tilted Gaussian retinal image in case no alignment is performed. At last, the image analysis is considered for multiple coherent sources at different wavelengths. For a correct application of the analysis, it is important to consider a weighted retinal image. The weighting has to be performed by dividing each spectral irradiance with the correction factors and adding them up. This procedure is in accordance with the laser safety standard and has a similarity to the investigation of incoherent sources.

In this investigation, the image analysis is also applied to incoherent sources which has the advantage that the analysis yields one single conservative result in contrary to the α definition of the lamp safety standard. It is found that the image analysis to determine the angular subtense for incoherent sources is comparable to the short-time method of coherent sources with a fixed maximum limitation of the angular subtense.

In the last part of the investigation, the image analysis is used to evaluate the eye safety with regard to the photochemical limits. Here, the analysis is less extensive than for the determination of the angular subtense as the size of the field stop is defined by a fixed angle of acceptance and the field stop has to be varied in its position to maximize the accessible emission. The shape of the field stop is defined to be either a rectangle or an ellipse. The use of a rectangular shaped field stop is not mentioned in the safety standards but it can safely be applied as it always measures a higher amount of radiant power for the accessible emission than an elliptical shaped field stop and is therefore more conservative.

A3.6 Outlook

In this paper, an image analysis was developed and presented to perform eye safety evaluations for radiation that is imaged on the retina of the eye. The image analysis is in accordance with the evaluation scheme from the laser safety standard and the lamp safety standard. The application of the image analysis was presented in this study using exemplary retinal images. In a follow-up investigation, a much wider variety of retinal images can be examined to further support the conclusions made in this investigation. Examining more retinal images help to make more detailed statements in how far the use of a rectangular field stop is more restrictive than with an elliptical one. Regarding coherent sources and the determination of the anguluar subtense of the apparent source, such investigations help to evaluate the deviations between the short-time, long-time and and long-time-magnifying method. Another interesting point is the comparison between an eye safety evaluation with simulated injuries induced by the investigated retinal image as it has been done in a previous investigation for the thermal damage regime [Kotzur et al., 2020c, 2021a]. For example, the topic of pulsed patterns could be examined [Jean et al., 2019, 2020], whereby three criteria must be used here according to the laser safety standard.

Another issue that can be addressed is performing a complete eye safety calculation for an optical product. For a complete eye safety evaluation, usually not only one retinal image has to be analyzed, but a large number of retinal images through different eye positions and different accommodations to find the most restrictive result. To handle this computational effort, it would be advantageous to develop algorithms that point to the most restrictive result for a given optical product. For a collimated laser beam, the most restrictive result is obtained when accommodating to infinity, since the radiation is focused on the minimum spot size. However, in the case of single astigmatic beams, it is unclear which accommodation leads to the most restrictive result, since there are two beam waists that are locally displaced. Another example is a scanning lidar system. When accommodating to infinity, the retina is scanned with a focused beam, while when accommodating to the scanning mirror, the radiation is always imaged on the same location on the retina. Here, both cases must be evaluated to determine the more restrictive result.

A3.7 Appendix A: List of symbols

α	angular subtense of the apparent source
$\alpha_{\max}$	maximum limitation of the angular subtense of the apparent source

$\alpha_{\min}$	minimum limitation of the angular subtense of the apparent source
α_x	angular subtense of the apparent source along the x-direction
α_y	angular subtense of the apparent source along the y-direction
α_{l}	angular subtense of the apparent source obtained for $t > T_2$
$\alpha_{\mathrm{l}}^{(M)}$	angular subtense of the apparent source obtained for $t > T_2$ and for the 'magnifying measurement condition'
α_{s}	angular subtense of the apparent source obtained for $t \leq T_2$
δ	rotation angle of Γ
γ	angle of acceptance of Γ
Γ	field stop
γ_{ph}	angle of acceptance of Γ_{ph}
γ_k	angle of acceptance of Γ along the k-direction with $k \in \{x, y\}$
γ_x	angle of acceptance of Γ along the x-direction
$\gamma_x^{\lim}$	limited angle of acceptance of Γ along the x-direction
γ_y	angle of acceptance of Γ along the y-direction
$\gamma_y^{\lim}$	limited angle of acceptance of Γ along the y-direction
Γ_{ph}	field stop for photochemical limits
γ_{ph}	angle of acceptance of Γ_{ph}
κ	retinal limit dependence on α
κ^{I}	retinal limit dependence on α for incoherent sources
κ^{C}	retinal limit dependence on α for coherent sources
$\kappa_\lambda^{\mathrm{C}}$	wavelength weighted quantity of κ^{C}
λ	wavelength of the radiation
$\mathbf{C}_{\mathrm{Ell}}$	ellipse describing Γ_{ph} obtained by the intersection between the retina and a right circular cone located at $\mathbf{O}$ with a full opening angle of γ_{ph}, an elevation angle of θ_{V} and an azimuth angle of θ_{H}
$\mathbf{n_1}$	normalized direction vector of the first axis of the ellipse $\mathbf{C}_{\mathrm{Ell}}$
$\mathbf{n_2}$	normalized direction vector of the second axis of the ellipse $\mathbf{C}_{\mathrm{Ell}}$
$\mathbf{O}$	coordinate origin
$\mathbf{x_0}$	center of the ellipse $\mathbf{C}_{\mathrm{Ell}}$
Ω	solid angle
Ω_M	solid angle for field stops located at $\mathbf{M}$
Φ	radiant power
Φ^{C}	radiant power measured by a circular field stop
Φ^{S}	radiant power measured by a square field stop

AE	accessible emission measured by a field stop
AE_λ	spectral accessible emission measured by a field stop
$\mathbf{M}$	center of Γ
θ_e	angle of a normal vector to the direction of radiation for evaluating the irradiance
θ_H	azimuth angle of a right circular cone located at $\mathbf{O}$
θ_V	elevation angle of a right circular cone located at $\mathbf{O}$
φ	angular coordinate of a polar coordinate system
A	peak irradiance of $E^\mathrm{G}_\mathrm{Ell}$
a	half width of Γ
b	half width of Γ
$B(\lambda)$	blue light hazard weighting function defined in the lamp safety standard IEC 62471:2006
$C_4(\lambda)$	correction factor defined in the laser safety standard IEC 60825-1:2014
$C_7(\lambda)$	correction factor defined in the laser safety standard IEC 60825-1:2014
d_2	distance between ideal lens and retina in the air-equivalent eye model
$d_\%$	diameter containing an arbirtrary power percentage of the total radiant power of the retinal image
$d_{62.5}$	diameter containing 62.5 % of the total radiant power of the retinal image
d_{63}	diameter containing 63 % of the total radiant power of the retinal image
$d_{71.5}$	diameter containing 71.5 % of the total radiant power of the retinal image
d_{86}	diameter containing 86 % of the total radiant power of the retinal image
d_Ap	circular aperture diameter of the air-equivalent eye model
E	irradiance
E'	weigthed and unaveraged irradiance
E'_λ	unweighted spectral irradiance
E_λ	spectral irradiance
E_RI	irradiance distribution on the retina / retinal image
$E^\mathrm{G}_\mathrm{Ell}$	elliptical Gaussian irradiance distribution
$E^\mathrm{G}_\mathrm{sym}$	radial symmetric Gaussian irradiance distribution
f	focal length of the air-equivalent eye model

K_1	half length of the first axis of the ellipse $\mathbf{C}_{\mathrm{Ell}}$
K_2	half length of the second axis of the ellipse $\mathbf{C}_{\mathrm{Ell}}$
L	radiance
L^{C}	radiance measured by a circular field stop
L^{S}	radiance measured by a square field stop
L_{V}	luminance
Q	radiant energy
r	radial coordinate of a polar coordinate system
$R(\lambda)$	burn hazard weighting function defined in the lamp safety standard IEC 62471:2006
t	emission duration
T_2	time defined in the laser safety standard IEC 60825-1:2014
w	$1/e$-width of $E^{\mathrm{G}}_{\mathrm{sym}}$
w_x	$1/e$-width in x-direction of $E^{\mathrm{G}}_{\mathrm{Ell}}$
w_y	$1/e$-width in y-direction of $E^{\mathrm{G}}_{\mathrm{Ell}}$
x	coordinate in a Cartesian coordinate system
x_0	x-coordinate of the center of Γ
$x_0^{\mathrm{Ell,G}}$	x-coordinate of the center of $E^{\mathrm{G}}_{\mathrm{Ell}}$
x_{Retina}	x-coordinate of the intersection point between the retina and the axis of a right circular cone representing Γ_{ph}
y	coordinate in a Cartesian coordinate system
y_0	y coordinate of the center of Γ
$y_0^{\mathrm{Ell,G}}$	y-coordinate of the center of $E^{\mathrm{G}}_{\mathrm{Ell}}$
y_{Retina}	y-coordinate of the intersection point between the retina and the axis of a right circular cone representing Γ_{ph}
(M)	'magnifying measurement condition' of the laser safety standard IEC 60825-1:2014

Disclosures

The authors declare that there are no conflicts of interest related to this article.